The Human Memory Circuit: Methodological development, validation, and implementation for the complete volumetric assessment of extra-hippocampal white matter and subfield structures in healthy and pathological aging

by

Robert S.C. Amaral

A thesis submitted in conformity with the requirements
for the degree of Master of Science
Integrated Program in Neuroscience
McGill University

Table of Contents

The Human Memory Circuit: Methodological development, validation, and implementation for the complete volumetric assessment of extra-hippocampal white matter and subfield structures in healthy and pathological aging

Robert S.C. Amaral

Master of Science

Integrated Program in Neuroscience
McGill University

2016

Abstract

The hippocampal formation is often investigated for its role in memory within the context of healthy development, aging, and numerous neuropsychiatric disorders. Projections from within the hippocampal formation form collections of thin white matter tracts (alveus and fimbria) leading out of the medial temporal lobe via the fornix. These fiber bundles then project to the mammillary bodies, forming the outputs of the human memory circuit. In contrast to the anatomy of the hippocampal formation, volumetric analysis of these white matter structures has received significantly less attention. Therefore, a robust and reliable anatomically detailed protocol was created for their manual segmentation using high-resolution magnetic resonance images (MRI). Segmentations were also designed for compatibility with a previous hippocampal subfield segmentation protocol derived from our group. Application of segmentations as inputs for an automatic segmentation pipeline was then assessed and confirmed using a strict validation procedure. The validated algorithm was used to segment MRI images from two populations: a healthy aging cohort (OASIS), as and an Alzheimer's disease (AD)/Mild Cognitive Impairment (MCI) cohort (ADNI) to analyze the architecture of both the subfields and the white matter. Significant decreases in bilateral fornix volume were observed to occur over the course of healthy aging, along with significant increases in volume of the bilateral alveus and CA1 subregions. Similar to these aging results, significant decreases were observed for both the fimbriae and fornices when comparing controls to the AD cohort. Contrary to results obtained for healthy aging, significant decreases were also observed in the CA1, CA4/DG, subiculum and SLRM. The MCI cohort demonstrated similar volumetric decreases when compared to controls.

No significant differences were present between AD and MCI cohorts. The observed and contrasting results obtained for the alveus and CA1 regions may suggest a neuroprotective or compensatory role for these structures in healthy aging.

Le circuit mémoire humaine : méthodologique développement, la validation et la mise en œuvre pour l'évaluation volumétrique complète de la matière et sous-zones blanches structures extra- hippocampiques dans le vieillissement sain et pathologique

Robert S.C. Amaral

Maître des sciences
Programme intégré en neurosciences
Université McGill

2016

Abstract

La formation hippocampique est souvent étudiée pour son rôle dans la mémoire dans le contexte développemental, du vieillissement, et dans de nombreux troubles neuropsychiatriques. Les projections émanant de l'intérieur de la formation hippocampique forment de groupes de minces faisceaux de matière blanche (alveus et fimbria) sortant du lobe temporal médian via le fornix. Ces faisceaux de fibres projettent alors vers les corps mamillaires, formant les sorties du circuit de la mémoire chez l'Homme. Comparativement à l'anatomie de la formation hippocampique, l'analyse volumétrique de ces structures de matière blanche a reçu bien peu d'attention. Par conséquent, un protocole robuste et fiable détaillé anatomiquement a été créé, pour la segmentation manuelle de ces régions; en utilisant des images de résonance magnétique à haute résolution (IRM). Les critères de segmentations ont également été conçus de sorte à être compatibles avec un précédent protocole provenant de notre groupe; permettant la segmentation des sous-régions de l'hippocampe. L'application de ces critères de segmentations pour une utilisation en segmentation automatique a par la suite été évaluée et confirmée en utilisant une procédure de validation stricte. L'algorithme de segmentation validé a ensuite été utilisé pour segmenter les images d'IRM pour deux populations: une cohorte vieillissant en bonne santé (OASIS), ainsi que les groupes atteints de la maladie d'Alzheimer (AD) / ou de déficience cognitive légère (MCI) au sein de la cohorte ADNI, afin d'étudier l'architecture des sous-régions de l'hippocampe ainsi que de la matière blanche associée. Au cours du vieillissement en bonne santé, des diminutions bilatérales significatives du volume du fornix ont été observées, accompagnées bilatéralement d'une augmentation significative du volume de l'alveus et de la sous-régions CA1. De même, des diminutions significatives ont été observées pour les deux

fimbria et fornix lorsque l'on compare les contrôles à la cohorte AD; mais contrairement aux résultats obtenus pour le vieillissement en santé, des diminutions significatives ont également été observées dans le CA1, CA4 / DG, subiculum et SLRM. La cohorte MCI a démontré des diminutions volumétriques similaires par rapport aux témoins. Aucunes différences significatives n'a été observées entre les groupes AD et MCI. Les résultats contrastants observés obtenus pour les régions de l’alveus et CA1 peuvent suggérer un rôle neuroprotecteur ou compensatoire pour ces structures dans le vieillissement sain.

Acknowledgements

The work presented in the thesis herein would not be possible without the members of the Computational Brain Anatomy Laboratory who have provided me with not only support and guidance, but also great company. It is for these reasons that I wish to thank each and every member for their devotion to completing excellent science, as well as for providing an environment that fosters academic growth, learning, and experience so readily and easily. For this, I thank you all.

I also wish to thank my committee members Dr. John Breitner, Dr. Louis Collins, and Dr. Jens Pruessner for their guidance, attendance, and contribution to each and every committee meeting held for the present project, including my defense seminar. I can truthfully say that each meeting was a great learning experience, and their feedback increased both the quality of my work, and scope of my scientific capabilities. I thank them for challenging and pushing me to think critically, while also providing a comfortable atmosphere to do this in.

I would also like to thank Dr. Daniela Palombo for providing me with my first opportunity to be involved in science during my undergraduate degree. It is through the many late nights of laboratory work and lengthy conversations we have shared over those years that helped to develop my initial scientific curiosity.

To my family, thank you. Your endless support and constant encouragement has always driven me to pursue researching the very science I am most passionate about. In particular, I would like to thank my parents, Roberto and Susana Amaral, who have fostered not only my interest in science even at an early age, but for supporting me in everything that I do. I am eternally grateful to you both. To Samantha D'Souza, thank you for your unwavering love and support, and for constantly instilling within myself the courage, drive, and dedication to complete any and all my goals. These qualities I have learned from you. I also wish to thank my grandparents Maria Evangelina Amaral and Walter Furtado Cabral, who respectively, have suffered, and still suffer from the very disease studied in the present thesis. They serve as a constant personal motivation for the work described herein, and it is to them that I dedicate this thesis to.

Above all, I would like to thank the individual who has coached me through the past four years, my supervisor, Dr. M. Mallar Chakravarty. Without his constant support and guidance none of this work would be possible. It has not only been a pleasure to work with a scientist so devoted to the scientific endeavor, but also one who is dedicated to his students. I appreciate the many opportunities to showcase my work and the time spent conversing and developing scientific ideas. It is through these many conversations that I have been most inspired. I sincerely thank you.

Preface

The present dissertation is of original, unpublished, and independent work by the author, Robert S.C. Amaral.

A version of the work described in Chapter 3 and 4 has been written and submitted for publication as: Amaral, R. S. C., Park, M. T. M., Devenyi, G. A., Lynn, V., Pipitone, J., Winterburn, J., Chavez, S., Schira, M., Lobaugh, N., Voineskos, A. N., Pruessner, J. C., Chakravarty, M. M., the Alzheimer's Disease Neuroimaging Initiative. (2016). Manual segmentation of the fornix, fimbria, and alveus on high-resolution 3T MRI: Application via fully-automated mapping of the human memory circuit white and grey matter in healthy and pathological aging.

Min Tae Matt Park aided in the initial public dataset download, setup, and computational troubleshooting. Gabriel A. Devenyi assisted in the validation experiment by preforming the transformations listed in section 3.6 'Reliability of Automatic Segmentation'. Vivian Lynn provided a second set of segmentations for completion of the inter-rater reliability comparison listed in section 3.3 'Reliability of Manual Segmentation'. Julie Winterburn provided the hippocampal labels used throughout the manuscript and can be found at: http://cobralab.ca/atlases/Hippocampus.html. Sofia Chavez, Mark Schira and Nancy Lobaugh provided support for the original scanning acquisition parameters listed in section 3.1 'Atlas Image Acquisition'. Jens C. Pruessner provided valuable feedback on anatomical accuracy of tracings. M. Mallar Chakravarty provided academic oversight, troubleshooting, project consulting and initial project conceptualization. Robert S.C. Amaral led the project conceptualization, planning, as well as execution, and preformed all experiments, validations, statistics, including the complete write up of the manuscript, supplementary materials and generation of figures. Data used in the present project was obtained from publically available datasets, specifically the Open Access Series of Imaging Studies (OASIS; Marcus et al., 2007) dataset and the Alzheimer's Disease Neuroimaging Initiative (ADNI; see adni.loni.usc.edu) dataset.

Chapter 1: Introduction

To date, magnetic resonance imaging (MRI) remains one of the most popular neuroimaging techniques for the investigation of human brain structure. MRI is particularly valued for its ability to produce detailed *in vivo* images of the human brain with minimal risk and invasiveness. This has allowed for the study of both brain structure and function and has fostered entirely new fields of study, including the volumetric study of brain regions via manual segmentation of MRI images. Recent advancements in MRI methodology have increased not only the quality of images, but have also made MRI an attractive neuroimaging technique for the imaging of large populations and datasets. Specific advancements in image acquisition and processing, as well as the use of high-field and high-resolution MRI, allow for *in vivo* imaging at a previously unprecedented level of detail and also within more manageable time constraints. These advancements have now allowed for the volumetric investigation of structures that previously could not be studied *in vivo*.

Such recent MRI advancements have placed increased focus on the investigation of the human hippocampus, particularly due to its unique anatomy. The hippocampus is composed of subfields that previously could only be studied via post-mortem histology and dissection. However, using novel MRI techniques, the subfields of the hippocampus are not only accessible *in vivo,* but can be investigated within the context of many forms of brain dysfunction. In fact, the investigation of the hippocampus as a whole has already occurred within the context of schizophrenia (Arnold et al., 2015; Haukvik et al., 2015), depression (Treadway et al., 2015; Videbech & Ravnkilde, 2015), and drug addiction (Castilla-Ortega et al., 2016; J. Xu et al., 2014). Despite this, the hippocampus is most known for its involvement in memory, as it was first documented in the case of patient H.M. who suffered from global amnesia following a bilateral medial temporal lobectomy. This procedure involved excision of over two thirds of the hippocampi (Scoville, 1954). It is from this case study that much research has focused on, and solidified the importance of the hippocampus as a brain structure implicated in both healthy and pathological aging in the form of dementias and, more, specifically, in the context of Alzheimer's disease.

It is estimated that the number of Canadians living with the most common form of dementia, Alzheimer's disease (AD), will grow to 1.4 million by 2031 (Van Hoesen & Pandya, 1975a). AD is marked by a slow decline in cognitive abilities beginning with memory impairments and is often preceded by a milder form of cognitive decline termed Mild Cognitive Impairment (MCI) (Morris et al., 2001; Petersen et al., 1999). AD and MCI pose a serious risk to the Canadian healthcare system, especially given that little is known about the cause of the disease and also that viable or efficient treatments do not yet exist (Ostbye & Crosse, 1994; Wimo, Winblad, & Jönsson, 2007). Therefore, much research has focused on understanding the progression of neurodegenerative processes that may lead to disease onset and further investigation of novel biomarkers that can be used to better understand disease progression and treatment response.

In light of the MRI advancements described above, the investigation of the hippocampus and its intricate subfields has occurred within the context of healthy (La Joie et al., 2010; Mueller & Weiner, 2009; Mueller et al., 2007; Voineskos et al., 2015) and pathological aging (Apostolova & Thompson, 2008; Chételat et al., 2008; Frisoni, Ganzola, Canu, Rüb, Pizzini, Alessandrini, Zoccatelli, Beltramello, Caltagirone, & Thompson, 2008a). However, it is important to note that the hippocampus represents only one component of the entire memory circuit. Specifically, sensory areas of the brain project to key cortices of the medial temporal lobe and serve as inputs to the hippocampus itself (Amaral & Lavenex, 2007; Duvernoy, Cattin, & Risold, 2013). Projections from within the hippocampus form collections of thin white matter tracts that eventually lead out of the medial temporal lobe. In contrast to the hippocampus, in vivo volumetric MRI of extra-hippocampal white matter structures have received significantly less attention. Given the lack of previous anatomical investigation of such structures, a robust and reliable anatomically detailed protocol for manual segmentation is needed. In this way, such methodology would allow for the volumetric assessment of these components of the memory circuit, thereby exploring their role in healthy and pathological aging.

In addition to this, while automated segmentation techniques for the hippocampus have been made available (Iglesias et al., 2015; Pipitone et al., 2014; Van Leemput et al., 2009; Yushkevich, Pluta, et al., 2015b; Yushkevich et al., 2010), similar methodology does not yet exist for white matter regions of the memory circuit. The implementation of such automated

techniques for extra-hippocampal white matter areas is needed to allow for investigations of the hippocampal-related memory structures at the circuit level and for the rapid and efficient segmentation of large datasets in the context of different disease and/or other populations.

The over-arching motivation for the present work rests on first understanding the differences between healthy and pathological aging, with specific focus on AD and MCI. By investigating differences in disease pathology and identifying key anatomical areas of interest, the identification of biomarkers for diagnosis or areas suitable for target-treatment options may be possible. Secondly, an additional motivating factor is to contribute to the field of MRI volumetry by developing, validating, and making available new methodologies for the manual and automatic volumetry of memory circuit-related brain regions.

The present thesis has three main goals: given the absence of a viable segmentation protocol for the extra-hippocampal white matter, the first objective is to create a complete, detailed, and reliable segmentation procedure adhering to the true anatomy of the white matter output regions of the hippocampus. The resulting segmentation protocol maps the complete anterior–posterior extent of all white matter structures using high-resolution MRI-data, and would be tailored to fit with our previously published protocol for the segmentation of hippocampal subfields (Winterburn et al., 2013). In this way, a complete atlas of all hippocampal subfields and outputs of the memory circuit can be created. The second objective is to evaluate the possibility of automatically labeling the white matter structures on standard MRI data using a framework previously used for the labeling the hippocampal subfields (Chakravarty et al., 2013; Pipitone et al., 2014). The third objective is to characterize the volume of the hippocampal subfields and white matter structures through the course of healthy and pathological aging using the newly derived white matter atlas and existing hippocampal subfield atlas as inputs for automated segmentation. This was done using two different publically available datasets. First, the OASIS dataset (Marcus et al., 2007) was used to investigate the normative trends of hippocampus and white matter substructures throughout the course of healthy aging. The same was completed for patients suffering from AD or MCI using data from the Alzheimer's NeuroImaging Initiative (ADNI; Mueller, Weiner, Thal, Petersen, Jack, Jagust, Trojanowski, Toga, & Beckett, 2005a; 2005b).

Taken together, the methods and results presented in this thesis will not only help to further elucidate the differences between healthy and pathological aging, but may also lead to the identification of novel biomarkers for disease risk or treatment-targets. In addition, the present study will also contribute to the development of novel methodologies for the assessment of structures comprising the memory circuit, which can later be used in the context of other diseases, populations, or large datasets.

Chapter 2: Literature Review

The following section provides a review of the background literature related to the work in the present thesis. This includes: the anatomy of the medial temporal lobes (including the hippocampus, white matter and its circuitry), imaging methods regarding structural MRI, segmentation techniques for structures in the medial temporal lobes, and relevant background information concerning pathological and healthy aging.

2.1 The Medial Temporal Lobes

Along the medial bank of the temporal lobes lie a collective group of structures that are known to be critical for proper memory function (Squire, Stark, & Clark, 2004). Known as the Medial Temporal Lobe (or Mesial Temporal Lobe by some; MTL), the structures collectively forming this area are highly interconnected and form what is known as the 'memory circuit'. These structures include the MTL cortices, the hippocampus and its subfields, as well as the extra-hippocampal white matter tracts that emanate from within the hippocampus itself. While it is understood that the memory circuit can also include areas of the thalamus, basal forebrain, and higher cortical regions (Zillmer, Spiers, & Culbertson, 2007), the aforementioned regions are considered to be the key regions of the human memory circuit. Specifically, they can be thought of as a circuit by way of their anatomical interconnectivity and together compose three dynamically connected components: a set of input structures, a central-processing hub, and a set of output structures.

2.1.1 History of Study and Involvement in Memory Functions

That we know of, the earliest documented evidence suggesting the involvement of MTL regions in memory function transpired nearly a century ago by way of a clinical case study of an amnesic patient (Bechterew, 1900). Following the death and brain resection of a 60 year old male patient who suffered from over 20 years of memory impairments, neuropathological findings identified significant bilateral atrophy to key areas of the bilateral MTL, including the hippocampus and

the surrounding MTL cortices. This marked the first ever-recorded suggestion that MTL regions are critically involved in some aspect of memory function.

Nearly 50 years later, a similar clinical case was observed in a patient who suffered from vascular infarcts following an insulin coma that implicated structures in the MTL region directly (Grünthal, 1947). Focal damage to the hippocampus and cortices left the patient with severe intellectual deficiencies, including severe anterograde and retrograde amnesia. In the following years, a similar clinical case of MTL damage was also presented in a vascular dementia patient and resulted in the same outcome of severe memory impairments (Glees & Griffith, 1952).

However, it was not until the 1950s that the MTL region (and most notably the hippocampus) became a primary focus of memory study in humans due to the bilateral medial temporal lobectomy of patient H.M. whom suffered from persistent epileptic seizures originating from these areas (Scoville, 1954). In what is now considered an accidental human lesion study, patient H.M. suffered from serious impairments in the ability to form new memories following the resection of parts of the bilateral MTL, resulting in the first documented direct evidence indicating that the MTL was vital for memory function. In addition, for the first time, formal and clinical assessment of the extent of memory impairments was well documented and evaluated (Milner, 1972; Scoville & Milner, 1957). The study and characterization of H.M.'s impairments has since continued for over 30 years and provided integral evidence of the involvement of the hippocampus in memory function (Corkin, 1984).

Since these initial discoveries, an overwhelming amount of neuroscientific research now focuses primarily on the investigation of the hippocampus, which constitutes only part of the human memory circuit within the MTL. With the improvement of novel MRI acquisition and analysis methods, the anatomy, structure, and function of the hippocampus and MTL structures have now occurred within the context of health and disease. In particular, neuroimaging advancements in MRI have allowed for both structural and functional (fMRI) investigation in order to better understand the components of the memory circuit. While the functions of MTL regions still remain a source of extensive investigation, the anatomy of MTL regions are well documented.

2.1.2 Anatomy and Circuitry of MTL Regions

The human MTL encompasses the most medial elaborations of the temporal cortex and its associated neighboring structures (Amaral & Lavenex, 2007; Duvernoy et al., 2013; Insausti et al., 1998). The input structures of the MTL memory circuit include cortical grey matter regions of the neocortex, which are comprised of the perirhinal cortex, entorhinal cortex and parahippocampal cortex. The hippocampus is considered the central processing hub of the circuit and contains subfields that are cytoarchitecturally distinct from one another. Finally, the output structures include the surrounding extra-hippocampal white matter of the alveus and fimbria, as well as the fornix, which leads out of the MTL. Over the years many in-depth anatomical and histological investigations have been completed in order to fully understand and dissociate the different regions of the MTL, many of which are now established as gold-standard anatomical atlases (Amaral & Lavenex, 2007; Duvernoy et al., 2013; Mai, Majtanik, & Paxinos, 2015).

2.1.2.1 MTL Cortices

The MTL cortices occur along the ventral aspect of the brain and extend in the anterior-to-posterior direction, primarily along the parahippocampal gyrus (Insausti et al., 1998; see Figure 1). The perirhinal cortex (PRC) is composed of Broadmann areas 35 and 36 and occurs in anterior sections of the parahippocampal gyrus. In contrast, the parahippocampal cortex (PHC) occupies more posterior sections. However, a significant portion of the parahippocampal gyrus is defined as the entorhinal cortex (ERC; Broadmann area 28), which borders the medial PRC and occurs in slightly more posterior sections of the PRC (Amaral, Insausti, & Cowan, 1987). The ERC is a 6-layered cortex and remains poorly demarcated. Despite this, it has been shown to extend into more anterior regions such as the uncus, yet its posterior border remains ambiguous and innately more variable (Duvernoy et al., 2013; Insausti et al., 1998).

The MTL cortices serve as the primary input structures of the memory circuit and receive vast projections from various sensory cortical areas. Specifically, the PRC and PHC first receive information from unimodal and polymodal association cortices originating from the temporal,

parietal, and frontal lobes (Jones & Powell, 2016; Van Hoesen & Pandya, 1975b; 1975c; Van Hoesen, Pandya, & Butters, 1975). The respective sensory pathways to the PRC and PHC are distinct. In particular, the PRC receives input from both unimodal visual association areas and inferior temporal areas and is thought to mediate object-centered identification and processing (Suzuki & Amaral, 1994). Directly opposite to this the PHC receives visiospatial information from the posterior occipital cortex, superior temporal areas, as well as the posterior parietal cortex (Suzuki & Amaral, 1994; Tranel, Brady, Van Hoesen, & Damasio, 1988). Situated between the hippocampus and adjacent MTL cortices, the ERC receives afferent connections from both the PRC and PHC and reroutes information to the hippocampus (Amaral & Lavenex, 2007; Duvernoy et al., 2013).

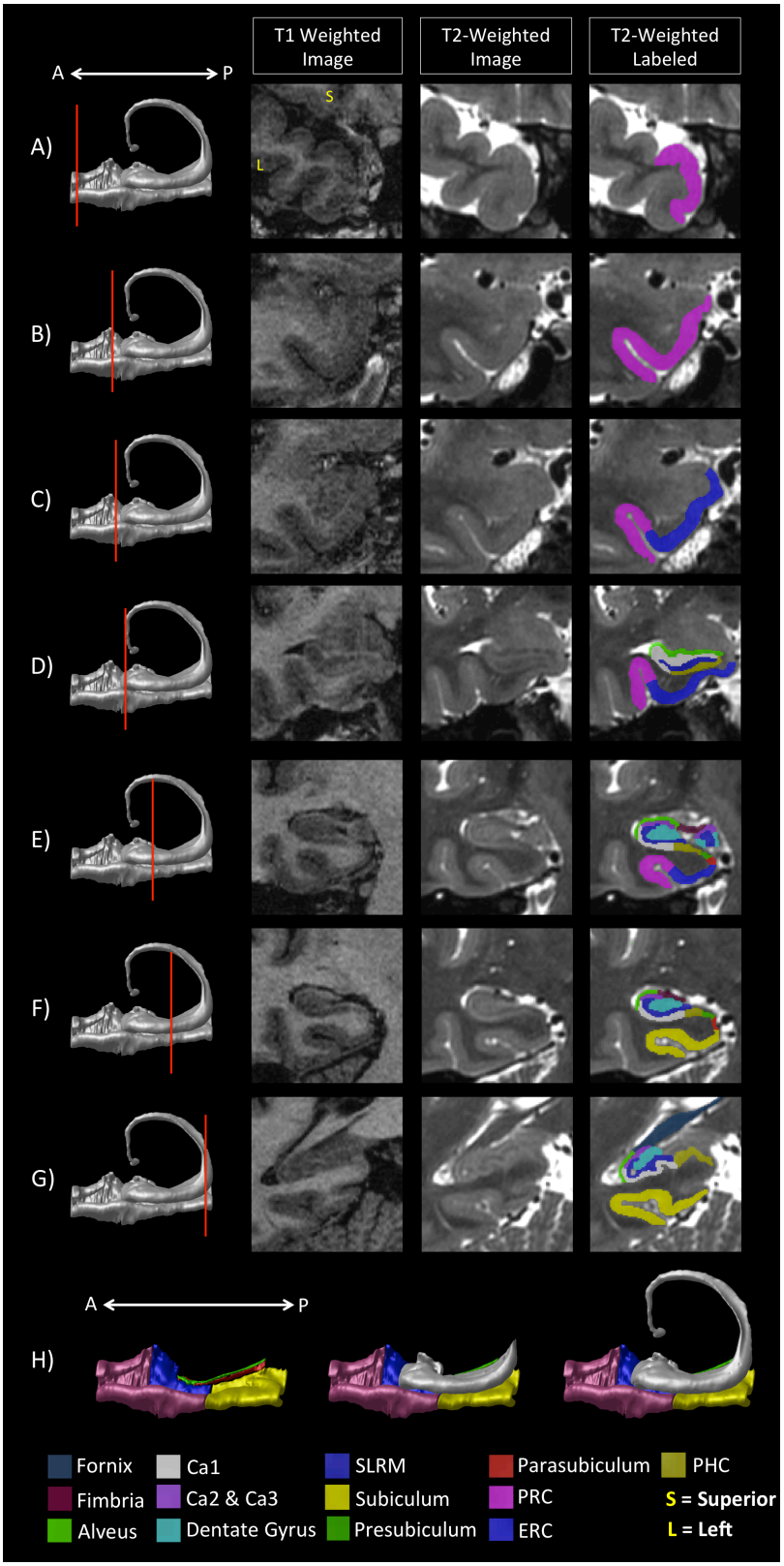

Figure 1. Anatomy of MTL cortices and hippocampal subfields. Rows A-G depict coronal sections of T1 and T2-weighted images. An additional column includes representative MTL structure delineations throughout T2-weighted images.

Adjacent 3D renderings depict the level at which each coronal slice occurs within the sagittal length of the MTL (red line). Row H provides representative 3D reconstruction of MTL cortices, MTL cortices + hippocampus, and MTL cortices + hippocampus + extra-hippocampal white matter. Image adapted from (Amaral, Winterburn, Pruessner, & Chakravarty, 2015).

2.1.2.2 Hippocampus

The hippocampus occurs bilaterally in the MTL and consists of a coiled elaboration of the cerebral cortex extending medially (and slightly superiorly) in the anterior-posterior direction (Amaral & Lavenex, 2007; see Figure 1). Sitting along the floor of the lateral ventricles, the grey matter of the hippocampus is inferiorly bordered by the MTL cortices and superiorly bound by the extra-hippocampal white matter sitting directly atop the hippocampus itself. While the hippocampus contains cytoarchitectonically distinct subfields, anatomical naming conventions exist to identify and refer to its gross structurally distinct sections. These divisions include the hippocampal head, body, and tail, and are commonly used throughout literature (Duvernoy et al., 2013; Mai et al., 2015; Malykhin, Lebel, Coupland, Wilman, & Carter, 2010; Pruessner, Li, Serles, Pruessner, Collins, Kabani, Lupien, & Evans, 2000a). The hippocampal head is a larger elaboration of folded cortex, which additionally re-folds upon itself laterally and posteriorly in the axial plane to resemble that of a 'J' shape. The head region contains multiple undulations and sits inferior to the amygdala. In more posterior sections, the hippocampal head forms the uncus region, and it is only when the uncus disappears that the body of the hippocampus is reached. The hippocampal body makes up a significant portion of volume as it forms the bulk of the anterior to posterior extension. Cross-sectionally it is reminiscent of a C-shape and without any undulations present, demarcation and identification of the different subfields and layers of the hippocampus is less difficult. In more posterior regions, the body of the hippocampus rises superiorly and elongates medially (i.e. flattens) towards the midline. This terminating region is termed the tail of the hippocampus.

2.1.2.2.1 Layers and Subfields

The hippocampus is composed of two distinct lamina: the Cornu Ammonis and the Gyrus Dentatus (Duvernoy et al., 2013). The lamina of the Gyrus Dentatus (or dentate gyrus; DG) is completely enveloped by the Cornu Ammonis and is composed of three layers: the strata

granulosum, strata moleculare, and the polymorphic layer. The strata granulosum is the main layer and contains the soma of granular neurons. The strata moleculare contains axonal fibers of the perforant pathway of the hippocampus while the polymorphic layer contains axons of the granular neurons of the strata granulosum.

On the other hand, the lamina of the Cornu Ammonis can be divided into 6 distinct layers: the alveus, the stratum oriens, stratum pyramidale, stratum radiatum, stratum lacunosum, and stratum moleculare. The alveus covers the superior surface the hippocampus and contains the main efferent fibers emanating from within the hippocampus. The stratum oriens blends with the stratum pyramidale and is mainly composed of basket cells and axonal fibers reaching the alveus. The stratum pyramidale is the main layer of the Cornu Ammonis and contains the pyramidal neurons of the hippocampus. The stratum radiatum houses the dendrites of the pyramidal cells while the stratum lacunosum is composed mainly of the white matter tracts of the perforant pathway. The stratum moleculare contains interneruons as well as the dendrites of the pyramidal neurons of the stratum pyramidale.

Neuroanatomically, the hippocampus can be further subdivided into several subfields with intricate morphologies and complex synaptic connections working together to create the processing hub of the memory circuit (Amaral & Lavenex, 2007). The majority of these subfields are composed of the different regions of the Conu Ammonis. Of all molecular layers of the Cornu Ammonis, the stratum pyramidale is the largest and can be described as having four cytoarchitecturally distinct subfields: Cornu Ammonis (CA) 1, 2, 3, and 4 (de Nó, 1934). The CA1 subregion is a continuation of the subiculum and contains triangular pyramidal neurons. Being the largest subfield, the CA1 extends along the full anterior to posterior extent of the hippocampus, occurring more superior in the hippocampal head and moving more superiolaterally along the body of the hippocampus. The CA2 region is composed of dense, large, ovoid soma and follows the same confirmation as the CA1 but is much narrower (Braak, 2012). The CA3 region is composed of scattered pyramidal neurons and axonal fibers. Continuing adjacent to the CA2 region, in the body of the hippocampus it corresponds to the most medial region of cortex that borders the lamina of the DG. The CA4 subfield contains large, scattered, ovoid soma and extends into the cavity of the DG. There is significant debate over the

existence of the CA4, as some believe that it may in fact represent a deep polymorphic layer of the DG (Amaral, 1978; Blackstad, 1956; Mai et al., 2015).

Separate from the Cornu Ammonis, the subicular region forms part of the parahippocampal gyrus and is also considered to be a subfield of the hippocampus given its connection to the CA1 region (Williams, Bannister, Berry, & Collins, 1995). Composed of four different sections (the prosubiculum, subiculum proper, presubiculum and the parasubiculum) the subiculum forms the medial continuation of either the PRC, ERC, or PHC, depending on the anterior to posterior position. In the hippocampal head, the subiculum proper occurs inferior to the CA1 subfield, forming the floor of the hippocampus. Throughout its anterior to posterior extension, the subiculum proper moves medially and extends further along the parahippocmpal gyrus. The subiculum proper is superiorly bound by the prosubiculum which borders the CA1 region and is inferiorly bound by the presubiculum, followed by the parasubiculum. The presubiculum and parasubiculum border the surrounding inferior MTL cortices and are not necessarily considered to be subfields of the hippocampus per se (Amaral, Insausti, & Cowan, 1984; Braak, 2012).

Although terminology varies across authors, the most consistently recognized subfields that together define the term 'hippocampal formation' (HF) include: the subiculum proper, CA1, CA2, CA3, CA4, and the DG (Duvernoy et al., 2013; Konrad et al., 2009). Although some include the presubiculum, parasubiculum and entorhinal cortex in the definition of the HF (Andersen, 2007; Witter, 2007), the present thesis will refer to the aforementioned subfields as the anatomical definition of the HF, as opposed to using the more ambiguous title of 'hippocampus'.

2.1.2.2.2 Circuitry

It is known that the HF constitutes two main pathways: the polysynaptic pathway and the direct pathway (See Duvernoy et al., 2013 for review). The polysynaptic pathway originates in the ERC (Amaral and Insausti, 1990) and perforates the subiculum in order to synapse on the DG. From here, axons from the DG then synapse on those present in the CA4 and CA3. Axons then project to the CA1 followed by subiculum before leaving the HF via the alveus. On the other

hand, the direct intrahippocampal pathway simply connects the ERC to the CA1. Axons then synapse in the subiculum and back down to the ERC (Du et al., 1993; MacLean, 1992).

In addition, controversy exits surrounding the presence of a third hippocampal pathway. Although its existence has been the subject of debate in humans, the alvear pathway first described by Cajal (1911) has been shown to exist in rodents (Deller, Adelmann, Nitsch, & Frotscher, 1996). Since axonal projections in the alvear pathway are first thought to travel through the alveus to reach the CA1 as opposed to perforating the subiculum as in the perforant pathway, it is considered to be a unique pathway (Mizutani & Kasahara, 1995).

2.1.3 Extra-Hippocampal White Matter

Along its entire anterior-to-posterior axis, the HF is enveloped by white matter (WM) protruding from within the HF. These myelinated fibers represent the main outputs of the HF from the polysynaptic and direct pathways, and are composed of the lamina of the alveus, fimbria and fornix. These WM structures contour the trajectory of the HF through the MTL until they aggregate near the HF tail and curve superiorly and anteriorly to project to the mammillary bodies.

The alveus covers the majority of the anterior portion of HF head. While it is considered to be a layer of the lamina of the Cornu Ammonis, its composition consists solely of axons emanating from the CA regions and is considered WM, and not part of the HF itself. The alveus also extends along the length of the HF, and sits atop the ventricular surface of the HF. Fibers of the alveus coalesce medially to give rise to a concentrated fiber bundle; the fimbria. The fimbria appears along the medial edge of the HF and is considerably larger than the alveus. Moving posteriorly, the fimbria then transitions into the crux of the fornix, at which point the WM tracts of the fornix curve vertically and anteriorly continuing through the midline of the brain. As axons of the fornicies travel through the center of the lateral ventricles, both fornicies (left and right) merge to form the body of the fornix. Finally, in its anterior extreme, both fornicies separate and descend to meet the mammillary bodies. Projections then reach the anterior nuclei of the thalamus via the mammillary bodies prior to their ascent into higher cortical regions.

2.2 Structural MRI

MRI is a medical imaging technique that takes advantage of the physical properties of the human body, high-field strength magnets, and the application of spatial magnetic field gradients in order to recover radio frequency wave energy that can be exploited to image the human body (Elmaoğlu & Çelik, 2011). An MRI scanner consists of a powerful magnet and a radio wave antenna that is used to send and receive such signals from the body. These received radio-frequency (RF) signals are then converted to images by a computer.

While MRI does not involve the use of radioactive compounds and is safe for humans, its value as a neuroimaging technique may be particularly attributed to its long list of capabilities (Elmaoğlu & Çelik, 2011). Namely, MRI can be used to investigate both structure and function using structural MRI or functional MRI (fMRI) respectively. In addition, MRI allows for the capture of images in all three planes (x, y, and z), therefore allowing for three-dimensional (3D) visualization of images with high spatial and/or temporal resolution. Since the present thesis involves the use of structural MRI, background with respect to this modality will be covered in the following sections.

2.2.1 MRI Physics and Acquisition

MRI takes advantage of the natural properties of atoms with on odd number of protons (e.g. hydrogen), which naturally precess around the axis of the atom (Nishimura, 1996). Hydrogen atoms are present throughout the human body in water molecules and vary in concentration based on tissue type. For example, fatty tissues maintain more water molecules and therefore increased numbers of hydrogen atoms. The main magnetic field within the long axis of the MRI scanner establishes a constant static magnetic field (measured in Tesla; T). Once an individual is placed within the scanner, hydrogen protons precess around the direction of the magnetic field. A radio frequency pulse can then be emitted and is specifically tuned to the frequency to which the hydrogen atoms precess (Elmaoğlu & Çelik, 2011). This causes some of the hydrogen protons to fall out of alignment with the static magnetic field and they are tipped towards the

transverse plan using a specified flip angle (e.g.: 90° would tip the main magnetization vector directly into the plane perpendicular to the static magnetic field). This places these protons in a high-energy state. As the energy from the radio frequency pulse is dissipated, the hydrogen atoms relax back into alignment with the static magnetic field, a process described as relaxation. While undergoing relaxation back to the original state, protons emit a signal which is measured by a receiving coil (Nishimura, 1996). Using spatial magnetic field gradients, this signal is then interpreted based in its spatial information and its frequency content in order to produce images.

Signal during the relaxation process is collected in K-space, a matrix where each point corresponds to a particular spatial frequency (Nishimura, 1996). This signal is first collected as a function of time and is converted to a function of frequency via Fourier transformation. Outer areas of this matrix correspond to high frequencies, while center areas are of lower frequencies. Each line of the K-space matrix is created in the time between the initial application of one RF pulse and the next, and is based on the strength of two gradients. The first gradient occurs in the x direction (frequency-encoding) and the second in the y direction (phase encoding). Once the K-space matrix is completed, each point corresponding to a spatial frequency is transformed via Fourier transformation in the x and y directions to create an image that shows the MR signal at each point.

The magnetic field strength generated by the MRI scanner is dependent on the strength of the magnet. Most common MRI machines maintain 1-3T magnets (Baudendistel, Heverhagen, & Knopp, 2004; Takahashi, Uematsu, & Hatabu, 2003), however, more higher-field magnets do exist and range from 4-11.4T (Kraff, Fischer, Nagel, Mönninghoff, & Ladd, 2015; Kuchling et al., 2014), although these magnets are somewhat less common and often require specialized expertise for acquisition and processing. While magnets at higher field strengths increase the signal to noise ratio and are able to provide high-resolution and –contrast images, imaging artifacts are more prevalent (i.e. increased inhomogeneity of the main field and the RF transmit field) along with a rise in the specific absorption rate (van der Kolk, Hendrikse, Zwanenburg, Visser, & Luijten, 2013).

2.2.2 Sequences

Based on the specific sequence and parameters used, MRI is capable of delivering images with varying contrasts that reflect the properties of different tissue types at differing resolutions. MRI pulse sequences involve configuration and the pre-programing of changing gradients and radiofrequency pulses. Namely, a pulse sequence involves the modulation of multiple scanning parameters including time to echo (TE), time to repetition (TR), field of view, and matrix size (among others). While many different types of pulse sequences exist the most common are spin echo sequences, which can be T1-weighted or T2-weighted and result in images with different properties.

2.2.2.1 T1-Weighted Images

In T1-weighted imaging, hydrogen protons are aligned in the static field and are tipped into the transverse (i.e. perpendicular) plane by a radiofrequency pulse. As described above, following the radiofrequency pulse protons realign to the static magnetic field. It is the emission of energy associated with this realignment that is measured in T1-weighted imaging (Figure 2, left). However, not all protons realign within the same time frame. Regions high in lipids tend to realign quickly, therefore producing a higher signal (e.g. WM areas like the fornix). Consequently these regions appear bright in the final image (Nishimura, 1996). In contrast to this, water maintains a dark appearance as it exhibits a slower realignment (e.g. cerebrospinal fluid of the lateral ventricles appear dark). T1-weighted images typically involve having a short TE and TR times. The TE is the time in milliseconds between the application of the RF pulse and the peak of the echo signal (Elmaoğlu & Çelik, 2011). The TR is the time between the initial application of one RF pulse and the next.

2.2.2.2 T2-Weighted Images

At the same time that hydrogen atoms aligned in the transverse plane undergo realignment to the static magnetic field, proton spins are decaying from their aligned precession in the transverse plane. The differences in this decay are captured in T2-weighted imaging (Figure 2, right). The

amount of decay is dependent on the tissue type, but areas high in fat and fluid appear bright. T2-weigthed images are normally acquired by having long TE and TR values.

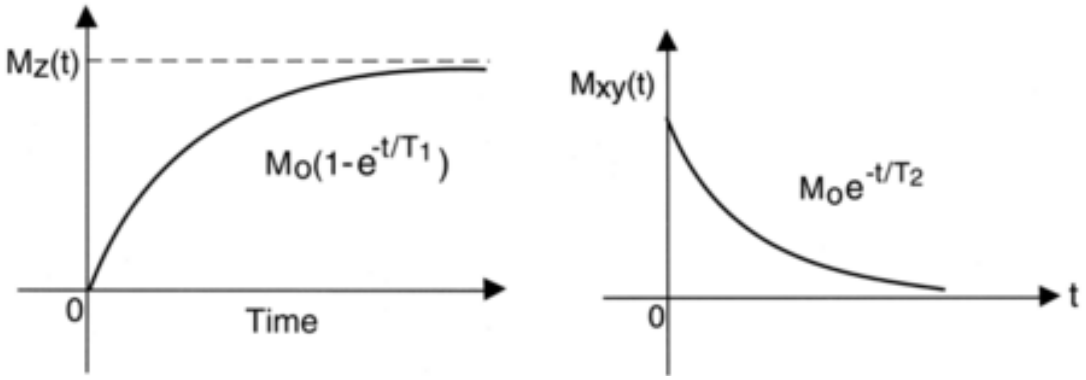

Figure 2. Graph of magnetization as a function of time. Left: Shows graph of recovery of magnetization with growth of T1. Right: Graph of magnetization with decay rate of T2. Image source: Hashemi, Bradley, & Lisanti (2010).

2.2.2.3 Gradient Echo Sequences

Gradient echo sequences use gradient fields to generate the transverse magnetization (Elmaoğlu & Çelik, 2011). In addition, gradient echo sequences also use flip angles of less than 90°. A flip angle is the amount of rotation the net magnetization exhibits following a radiofrequency pulse (Nishimura, 1996). A key advantage of these sequences is that they are more versatile and provide better contrast between the white and grey matter of the brain.

2.2.3 High-Resolution MRI

Improving the spatial resolution in MRI data is critical to the success of much of the present work and helps define the clarity with which different structures can be visualized. In MRI, image resolution is defined by the size of voxels (Nishimura, 1996). Similar to pixels, voxels are 3D cubic structures of image space and maintain specific sizes for each direction (i.e. x, y, and z). Together, all voxels of an MRI image compose the entire 3D image. Voxel size itself depends on the field of view, matrix size, as well as the image slice thickness. The matrix size is the number of frequency encoding steps in one direction as well as the number of phase encoding steps in the other plane (Elmaoğlu & Çelik, 2011). The field of view is simply the size of the area covered by the matrix. Modulations of these parameters are capable of modifying the size and resolution of MRI images.

Most MRI imaging is often completed at lower, more standard image resolutions (i.e. 1mm isotropic images). Many investigators choose to use such lower-resolution images since acquisition times are not only faster, but file sizes are also more manageable. However, in order to achieve the fine level of detail necessary to investigate detailed neuroanatomy, an increasing amount of studies employ high resolution imaging with voxel sizes well below the standard. While an exact definition of what constitutes an image as being of high-resolution does not exist, it is generally accepted that in-plane voxel sizes for high-resolution images are between 0.7-0.1mm. It is important to note that high-resolution images can be isotropic or anisotropic. Since isotropic sequences increase scanning times significantly, anisotropic sequences sacrifice spatial detail in one image plane (e.g. y) for the high-resolution acquisition in-plane (e.g. x, z).

2.2.4 Image Preprocessing

Once MRI image acquisition has been completed several preprocessing steps are typically taken to minimize the impact of image artifacts on subsequent analysis steps. While many different preprocessing steps can be performed on images, the most common (and used in the thesis herein) are bias field correction and brain extraction.

2.2.4.1 Bias Field Correction

The bias field leads to intensity inhomogeneity throughout the image. The field itself is a low frequency and spatially varying MRI artifact. This causes smooth spatially-dependent signal intensity variation within and is due to the spatial inhomogeneity of the magnetic field during scanning, variations in the receiving coil, as well as the interaction of the human body with the magnetic field (Despotović, Goossens, & Philips, 2015). A number of methods have been derived to circumvent bias field inhomogeneities including the use of low-pass filtering (Cohen, DuBois, & Zeineh, 2000), minimizing the image entropy (Vovk, Pernus, & Likar, 2007), fitting the histogram of the local neighborhood intensities to the global histogram of the image itself (Shattuck, Sandor-Leahy, Schaper, Rottenberg, & Leahy, 2001), maximizing the high frequency content of the image (Sled, Zijdenbos, & Evans, 1998), and also by creating a registered template image (Lewis & Fox, 2004). While many automatic alternatives exist, the N3 (nonparametric

nonuniformity normalization) correction algorithm (Sled et al., 1998; Zheng, Chee, & Zagorodnov, 2009), which smooths the present inhomogeneity by maximizing the high frequency content of the distribution of tissue intensity, remains one of the most popular methods used to date (Vovk et al., 2007). Recent improvements have resulted in an updated version (i.e. N4 correction; Tustison et al., 2010).

2.2.4.2 Brain Extraction

Brain extraction involves the removal of non-brain tissues (e.g. the skull) such that only brain tissue can be isolated. Brain extraction is a key step in the analysis of MRI images and can be used to provide measures of total brain volume. The most common method of brain extraction relies on the use of a template brain mask registered to the respective image in order to remove non-brain tissue (Xue et al., 2007). The same outcome can be achieved via the use of a common brain extraction tool (BET; Battaglini, Smith, Brogi, & De Stefano, 2008; Smith, 2002), which inflates a sphere until the brain boundary is reached. Recently, a robust and reliable method of brain extraction described as brain extraction based on nonlocal multi-atlas-based segmentation technique (BEaST) has been made available and uses a library of 80 priors to complete nonlocal segmentations of brain masks in a multi-resolution framework (Eskildsen et al., 2012).

2.3 Segmentation

Segmentation of the human brain involves the detailed identification of specific anatomical regions of the brain (Despotović et al., 2015). This type of neuroanatomical parcellation may occur at a coarse level of neuroanatomy (e.g. segmentation of the entire brain) or at the level of specific structures (e.g. segmentation of the amygdala, HF, cerebellum, etc.). Since image segmentation relies on the isolation of a 3D MRI image through all slices and planes, 3D structure and shape metrics (e.g. volume, surface area, deformation, shape, etc.) can be derived based on these segmentations (Tofts, 2003). MRI-based image segmentation therefore allows for the *in vivo* study of human brain structure and morphology. Neuroanatomical segmentation can occur either by way of manual tracing, or automatic segmentation (Despotović et al., 2015).

While both processes have been used to segment various regions of the memory circuit, particular focus has been placed on the segmentation of the HF and its subfields.

2.3.1 Manual Segmentation

Manual delineation involves the slice-by-slice identification of any given neuroanatomical structure of interest (or Region of Interest; ROI) by a human rater (Despotović et al., 2015). Each ROI is completed via tracing on a voxel-by-voxel basis or by using a flood-fill after careful demarcation. Human raters are expertly trained in the generation of ROIs and typically follow a detailed segmentation protocol. Such protocols increase reliability and accuracy of tracing and are based off of various brain atlases and relevant anatomical literature (See Yushkevich, Amaral, et al., 2015a). Since protocols involve image segmentation based on contrast differences, as well as specific geometric and heuristic rules, ROIs generated by expert tracers are considered gold standard in the field. In order to evaluate the reliability of a protocol, measures of inter-rater and intra-rater reliability are usually obtained. This typically involves the retracing of an ROI by the same rater (intra-rater) or comparison of a rater's completed segmentation to that of a different rater (intra-rater). The Dice's Kappa overlap metric (Dice, 1945) is most often used to evaluate reliability and assess the degree of overlap between labels where 0 represents no overlap and 1 represents perfect overlap between labels. The Dice's Kappa metric is given the formula:

$$\kappa = \frac{2a}{2a + b + c}$$

The number of voxels in both segmentations is denoted by a while b + c represents the sum of voxels unique to each respective label. Being an overlap metric, Dice's kappa penalizes raters based on spatial placement. Therefore, for structures maintaining high surface area-to-volume ratios (e.g. WM tracts) it may be harder to achieve reliability. Alternatively, the intraclass correlation coefficient (ICC) can also be used to assess the degree of correlation between any two volumes where 0 represents no correlation and 1 represents a perfect correlation. ICC measures the degree of correlation to which two volumes are associated with each other.

However, unlike the Dice overlap metric, it does not evaluate the spatial or anatomical similarity between ROIs. This can lead to certain biases. For example, two identical ROIs in very different areas can receive a high ICC. Despite the advantages of Dice's Kappa over ICC, both are often used in literature to ensure reliability of segmentation protocols. While tracing protocols do exist for MTL structures, most have focused on segmentation of the HF and its subfields.

2.3.1.1 The Hippocampus

To date, over 70 different protocols exist for the segmentation of the whole HF (Boccardi et al., 2011). The earliest recorded studies completing whole hippocampal segmentations for volumetric investigation involved segmentation limited to the head and body of the HF (Jack et al., 1989), or the hippocampal body exclusively (Bremner et al., 1995; Douglas, 1995; Kaye et al., 1997). The lack of inclusivity can be attributed to the low field strengths available at the time (1T) as well as the poor image resolution (1.5-5mm; Geuze, Vermetten, & Bremner, 2005; Jack, 1994). Advancements in MRI technology and methodology would later impact the anatomical inclusivity of protocols such that the majority of the anterior to posterior extent of the HF could be segmented as one complete ROI, or separately segmented into head, body, and tail regions (Convit et al., 1997; deToledo-Morrell et al., 2004; Killiany et al., 1993; Lehericy et al., 1994; Pruessner, Li, Serles, Pruessner, Collins, Kabani, Lupien, & Evans, 2000b; Sheline, Wang, Gado, Csernansky, & Vannier, 1996; Soininen et al., 1994; Watson, Jack, & Cendes, 1997). Although not an exhaustive list, at more standard imaging resolutions (e.g. 0.9-1mm) and higher field strengths (1.5-3T), many of the above-mentioned protocols are still used today (Boccardi et al., 2011; Geuze et al., 2005; Konrad et al., 2009). However, the many available segmentation protocols maintain slightly different, but significantly distinctive rules (e.g. alveus and fornix may be included or excluded in ROI). This has therefore prompted the development of a harmonized protocol in order to define a standardized protocol for segmentation of the whole HF (Apostolova et al., 2015; Boccardi et al., 2015; Frisoni et al., 2015; See http://www.hippocampal-protocol.net). Regardless, the ultimate limitation of such segmentation protocols lies within the treatment and segmentation of the HF as a unitary structure, as opposed to a structure composed of separate subfields.

2.3.1.1.1 Hippocampal Subfields

Recent in vivo structural MRI of the MTL have utilized some combination of high-field and high-resolution MRI acquisition techniques, post-mortem data, and long scan times to image and segment the HF subfields (Adler et al., 2014; Bender, Daugherty, & Raz, 2013; Ekstrom et al., 2009; Kerchner et al., 2013; 2012; 2010; La Joie et al., 2010; Mueller et al., 2007; Mueller & Weiner, 2009; Mueller et al., 2010; Olsen et al., 2013; Palombo et al., 2013; Van Leemput et al., 2009; Winterburn et al., 2013; Wisse et al., 2014; 2012; Yushkevich et al., 2009).

While the above-mentioned tracing protocols are capable of successfully segmenting the subfields of the HF, protocols differ in the degree of specificity and anatomical accuracy to which this can be accomplished. For example, many protocols vary not only in the number of subfields segmented, but also in the extent to which the grouping of multiple subfields together within the same ROI occur. Specifically, Palombo et al. (2013) and Olsen et al. (2013) create only 3 ROIs within the body of the HF: subiculum, CA1, CA2/CA3/CA4/DG (grouped together) while Muller et al. (2007) include 4 separate ROIs: subiculum, CA1, CA2, CA3/CA4/DG (grouped together). On the other hand, Winterburn et al., (2013) segment 5 separate ROIs including the CA1, CA2/CA3, CA4/DG, subiculum, but also segment additional molecular layers of the statum lacunosum, radiatum and moleculare (SLRM).

Additionally, many protocols limit segmentation of the subfields to the body of the HF (Bender et al., 2013; La Joie et al., 2010; Mueller & Weiner, 2009; Olsen et al., 2013; Palombo et al., 2013) and few protocols carry their subfield segmentations throughout the entire anterior to posterior extent of the HF (Adler et al., 2014; Winterburn et al., 2013; Zeineh, Holdsworth, Skare, Atlas, & Bammer, 2012). For example while Van Leemput et al. (2009) exclude the hippocampal tail entirely, both Palombo et al. (2013) and Olsen et al. (2013) only segment subfields throughout the hippocampal body and include separate ROIs for the hippocampal head and tail regions. In addition, some groups restrict segmentation to the body of the HF (La Joie et al., 2010) or only segment a few slices throughout the body itself (Mueller et al., 2007).

Quality of subfield definitions also depends on the field strength, resolution and scanning parameters used to acquire high-resolution images. For example, many *in vivo* protocols use highly anisotropic voxel dimensions (high-resolution through the coronal plane of the HF, low-resolution through the anterior-posterior direction) for identifying these regions (Ekstrom et al., 2009; Kerchner et al., 2012; La Joie et al., 2010; Olsen et al., 2013; Palombo et al., 2013). For example, Mueller and colleagues (2009) preform segmentation on *in vivo* MR images acquired on a 4 T scanner with a resolution of 0.4 mm × 0.5 mm × 2 mm, while Van Leemput et al. (2009) present subfield-level segmentation using in vivo 3 T images with a 0.38 mm × 0.38 mm × 0.80 mm resolution. Palombo et al. (2013) and Olsen et al. (2013) also present with an anisotropic voxel dimension of 0.43 × 0.43 × 3.0 mm. Similarly, La Joie et al. (2010) use T2-weighted images with voxel dimensions of 0.375 mm x 0.375 mm x 2 mm. These anisotropic dimensions may not only lead to measurement bias, but also introduce partial volume effects in images, often causing blurring of boundaries and increasing the difficulty of subfield demarcation. Notable exceptions to this are the 0.2 mm isotropic post-mortem images from Yushkevich and colleagues (2009) as well as the 0.16mm isotropic voxel resolutions obtained in Adler et al., (2014). While this work offers greater anatomical detail it unfortunately relies on a small bore 9.4 T scanner and fixed *ex vivo* medial temporal lobe specimens with a 15- or 63-hour scan time. The applications of an atlas of this kind are limited given the lack of availability of post-mortem specimens and the associated problems in registering fixed images to *in vivo* data. Recent attempts have been made to overcome these limitations by employing the use of in vivo 7T MRI (Kerchner et al., 2010; 2012; Kirwan, Jones, Miller, & Stark, 2007; Malykhin et al., 2010; Wisse et al., 2012; 2014; Zeineh et al., 2012). For example, although they interpolate their segmentations, Wisse et al., (2012; 2014) achieve high-resolution images with isotropic voxel dimensions of 0.35 mm at 7T. While advantageous, use of these protocols necessitates access to a 7T MR imaging system, which is not currently available at most academic research centers. Despite this, isotropic resolutions have been completed at 3T, as shown by Winterburn et al. (2013) who achieve 0.3mm isotropic T1 and T2 images for subfield segmentation.

Similar to reasons mentioned in section 2.3.1.1 ‘The Hippocampus’, an organized effort has been made in an attempt to harmonize segmentation of hippocampal subfields. While still in its early conception, the organized effort will attempt to bring agreement to the definition of proper

anatomical landmarks for subfields, as well as the strategies/rules used to segment subfields for subfield labeling in MRI data (Yushkevich, Amaral, et al., 2015a; See http://www.hippocampalsubfields.com/).

2.3.1.2 Extra-Hippocampal White Matter

While a few segmentation protocols have recently been introduced for MTL cortices (Bonilha, Kobayashi, Rorden, Cendes, & Li, 2003; Duncan, Tompary, & Davachi, 2014; Ekstrom et al., 2009; Insausti et al., 1998; Palombo et al., 2013; Pruessner et al., 2002; Yushkevich, Pluta, et al., 2015b; Zeineh et al., 2012), little advancement has been made with respect to segmentation of extra-hippocampal WM. Previously published protocols for the segmentation of the fornix are limited in number (Bilir et al., 1998; Copenhaver et al., 2006; Gale, Johnson, Bigler, & Blatter, 1995; Kuzniecky et al., 1999; Zahajszky et al., 2001), outdated, and contain several limitations. For example, all present protocols typically exclude posterior and/or anterior areas of the fornix. The few protocols which include the segmentation of more anterior sections of the fornix cease segmentation at the level of the anterior commissure and therefore omit inferior-most sections of the anterior pillars of the fornix (Copenhaver et al., 2006; Zahajszky et al., 2001). Similar to the grouping observed with subfields, all protocols group left and right fornices together into one ROI and do not differentiate between the left and right fornix. The observed grouping and lack of inclusivity of the fornix could be due to the use of standard imaging protocols limited in resolution and contrast. For example, Zahajszky et al. (2001) employed the use of 1.5T MRI to obtain a 1.5mm isotropic voxel dimensions while Copenhaver et al. (2006) also used a 1.5T scanner to achieve an anisotropic resolution of 1mm x 1mm x 1.5mm. These same limitations in image resolution have led to the exclusion of the alveus and fimbria altogether.

Some groups have since completed segmentations of the alveus and fimbria as part of hippocampal subfield work (Parekh, Rutt, Purcell, Chen, & Zeineh, 2015; Wang et al., 2003; Zeineh et al., 2012). Specifically, Wang et al. (2003) and Zeineh et al. (2012) both group alveus and fimbria regions together on 1mm isotropic data. While currently the most inclusive, Parekh, Rutt, Purcell, Chen, & Zeineh (2015), include a partial description of segmentation of both the alveus and fimbria on 7T 0.4mm images.

2.3.2 Automatic Segmentation

The particular costs and efforts associated with manual segmentation have motivated the development of automatic methods. By automating segmentation, time spent on segmentation would be dramatically reduced thereby facilitating research that would have otherwise taken much longer to complete. Automated segmentation techniques rely on an algorithm capable of generating a specific ROI on a given MRI scan. The underlying methods of algorithmic models vary and may rely on atlas-based techniques, deformable model techniques, or a combination of both (Dill, Franco, & Pinho, 2015).

The atlas-based automatic segmentation technique relies on the use of an atlas, usually consisting of an ideal (often a gold-standard manual) segmentation of the ROI on a representative MRI image of the population to be segmented (Cabezas, Oliver, Lladó, Freixenet, & Bach Cuadra, 2011; Dill et al., 2015). In order to complete segmentation automatically, the single atlas is first aligned directly with the target image to be segmented via registration. This registration is composed of a linear affine transformation followed by a non-linear affine transformation of the target image to the atlas. The linear transformation aligns the atlas and target images within the same coordinate space while the nonlinear transformation further refines the registration of internal brain structures (Dill et al., 2015). In this way, the atlas image (and its demarcated ROI) are now directly in line with that of the target image. These segmented ROIs are then transferred back to the original target image through the inverse linear and nonlinear transformations that originated during registration (Dill et al., 2015). However, since a single atlas may not successfully encompass the anatomical variability associated with any given population of target images, multi-atlas segmentation algorithms have been developed to increase segmentation quality. Similar to single-atlas segmentation, multi-atlas segmentation involves the registration of multiple atlases with the same target image such that a candidate segmentation is created on a per-atlas basis. All candidate segmentations are then combined to obtain a final segmentation though label fusion techniques. While capable of capturing the variability in anatomy, multi-atlas automatic segmentation comes with higher computational costs (Dill et al., 2015). An alternative method with lower computational costs involves the use of probabilistic atlases for image segmentation. Here, atlases are registered to one another and relative statistics (e.g.

geometrical shape, voxel intensity, etc.) are obtained and used in a secondary algorithm to segment target images.

Automatic segmentation methods may also rely on deformable models. This involves the placement of a contour in the target image, which is then iteratively deformed until the desired shape, and conformation of the ROI is met. Similar to atlas-based segmentation, deformable models may be semi- or fully-automated. Semi-automated techniques require the user to create the initial contour (or select predetermined landmarks in atlas-based segmentation), while fully automatic algorithms do not require user support and obtain initial contours through the registration with an atlas. Contouring is achieved by way of numerous variables including image intensity, geometry, and by avoiding deformations falling outside of the average geometric variation (Cootes, Edwards, & Taylor, 2001; Cootes, Taylor, Cooper, & Graham, 1995).

Similar to manual segmentation, the evaluation of the automatic segmentation involves reliability analysis relative to a set of gold standard labels. Labels automatically generated on target images are compared directly to manual segmentations of the same images. Dices' Kappa overlap metric (Dice, 1945), and to a lesser extent, intraclass correlation, are typically used to assess reliability and accuracy of automatic segmentation.

2.3.2.1 Automatic Segmentation of the Hippocampus

Automatic segmentation techniques for the whole HF have been proposed since the late 1990s (Dill et al., 2015). Earliest methods involved the use of deformable models and were semi-automated (Ashton, Parker, Berg, & Chen, 1997; Freeborough, Fox, & Kitney, 1997; Ghanei, Soltanian-Zadeh, & Windham, 1998; Kelemen, Székely, & Gerig, 1999). Semi-automated atlas-based segmentation methods have also been developed (Christensen, Joshi, & Miller, 1997; Haller et al., 1997; Hogan et al., 2000; Pluta, Avants, Glynn, Awate, & Gee, 2009; Tang, Mori, Ratnanather, & Miller, 2012) each employing slightly different methods for image alignment and registration. However, these semi-automated methods require the user to select specific points in all target images, which are used as reference points in later registration stages.

Fully automated methods have recently been developed and vary on their underlying techniques. For example, both deformable models (Duchesne, Pruessner, & Collins, 2002; Hu, Coupé, Pruessner, & Collins, 2011; Kim, Mansi, Bernasconi, & Bernasconi, 2012; Patenaude, Smith, Kennedy, & Jenkinson, 2011) as well as single-atlas-based techniques (Barnes et al., 2007; Carmichael et al., 2005; Friston et al., 1995; Jenkinson, Bannister, Brady, & Smith, 2002; Kwak et al., 2013; Woods, Grafton, Holmes, Cherry, & Mazziotta, 1998) have been developed for the fully automatic segmentation of the whole HF. However, the use of single-atlas techniques may not accurately capture the anatomical variability of target images. Multi-atlas automatic segmentation techniques have therefore been developed and validated to circumvent this issue (Aljabar, Heckemann, Hammers, Hajnal, & Rueckert, 2009; Coupé et al., 2011; Dill et al., 2015; Hao et al., 2014; Heckemann, Hajnal, Aljabar, Rueckert, & Hammers, 2006; Khan et al., 2011; Pipitone et al., 2014; Platero, Tobar, Sanguino, & Velasco, 2014; Sabuncu, Yeo, Van Leemput, Fischl, & Golland, 2010; Yushkevich et al., 2010). While the underlying multi-atlas methods are similar, algorithms differ in the methods regarding label fusion of all candidate labels. For example, (Coupé et al., 2011) use patch based method of label fusion while (Yushkevich et al., 2010) result in a final label via similarity-weighted voting and by minimizing the total expectation of labeling error. Hao et al. (2014) and Platero et al. (2014) use a minimization of energy function with intensity and prior terms to create a final segmentation. Despite the use of multiple atlases to account for subject variability, atlas sets used to segment a target population often originate from an entirely different population (e.g. use of adult atlas for segmentation of adolescents). Specific attempts have been made to address this issue by quantitatively hand-picking atlases from a set that most closely resemble the target population (Aljabar et al., 2009; Khan et al., 2011). However, novel methods have been created which involve less user effort and with a trade-off towards increased computational expense (Pipitone et al., 2014). Using Multiple Automatically Generated Templates (MAGeT; Chakravarty et al., 2013), Pipitone et al. (2014) employ multi-atlas voting following a bootstrapping procedure that uses a template library composed of images from the dataset under analysis. Here, high-resolution atlases are used to segment this template set of individuals. The template library is then used to segment the entire dataset and candidate labels are fused via majority vote, thereby producing fast and reliable segmentations.

Probabilistic automatic segmentation of the whole HF has also occurred, albeit to a lesser extent. The most popular and widely used method of whole hippocampal segmentation from this class of segmentation algorithms to date is Freesurfer's tool (Fischl 2002).

At any rate, the above-presented techniques involve whole-hippocampal segmentation of target images at standard resolutions (i.e. 1.5-1mm isotropic) and do not segment hippocampal subfields. While it cannot be said that one technique reigns superior to another since the methods and rigor of validation vary widely (Dill et al., 2015), some techniques offer a direct comparison to more widely used automatic segmentation tools (Pipitone et al., 2014). For a complete review of automatic segmentation of the whole HF see Dill et al. (2015).

2.3.2.1.1 Automatic Segmentation of the Hippocampal Subfields

Compared to the whole HF, the development of methods for the automatic segmentation of hippocampal subfields has occurred less frequently and comparatively recently. Of the available techniques, the majority of work involves completing subfield segmentation on target images with more standard image resolutions (Pipitone et al., 2014; Van Leemput et al., 2009). For example, Van Leemput et al. (2009) first proposed the use of automatic subfield segmentation on 1mm isotropic images using high-resolution T1-weighted hippocampal subfield atlases. This same technique has been applied in the widely used Freesurfer 5.3 (Fischl, 2012). Given the multiple concerns with quality of outputs and lack of validation (de Flores et al., 2015; Pluta, Yushkevich, Das, & Wolk, 2012; Wisse et al., 2012; Yushkevich, Pluta, et al., 2015b), the newest version of Freesurfer 6.0 (Iglesias et al., 2015) incorporated the use of 15 new *ex-vivo* high-resolution atlases acquired at 7T. Despite the novel atlases and capabilities of subfield segmentation on isotropic or anisotropic target images offered by Freesurfer 6.0, no attempts at validating its use on the standard images that it is most commonly used for have been made. Finally, the most recent technique applies MAGeT brain (Chakravarty et al., 2013; Pipitone et al., 2014) for segmentation of the hippocampal subfields using 5 high-resolution 3T atlases (Winterburn et al., 2013) on 1mm isotropic data. In an effort to validate subfield segmentations on isotropic data, authors compare down-sampled gold-standard manually derived atlas

segmentations to MAGeT brain segmented labels, thereby demonstrating the feasibility associated with this approach.

To date, only one group has developed a technique capable of subfield segmentation on high-resolution MRI images (Yushkevich et al., 2010; Yushkevich, Pluta, et al., 2015b). Automatic Segmentation of Hippocampal Subfields (ASHS) uses high-resolution atlases for the segmentation of anisotropic T2-weighted images. The original segmentation protocol first used (Mueller et al., 2007) limited automatic segmentation to the body of the HF and the algorithm itself required user input. However, ASHS was recently improved to include fully automated segmentation of subfields along the whole HF, in addition to a few cortical MTL areas (Yushkevich, Pluta, et al., 2015b). Despite appropriate validation, the method requires the use of both standard and high-resolution MR data, which may be cumbersome and difficult to obtain.

2.3.2.2 Automatic Segmentation of Extra-Hippocampal White Matter

Automatic segmentation of extra-hippocampal WM areas of the alveus, fimbria and fornix has been virtually nonexistent. Automatic segmentation of the fimbria has been previously incorporated in Freesurfer 5.3 (Fischl, 2012) and was based upon the hippocampal subfield delineations in Van Leemput et al. (2009). While Freesurfer 6.0 (Iglesias et al., 2015) is capable of automatically segmenting alveus and fimbria regions, methods with respect to the manual segmentation protocol used, or any sort of validation effort, have not been presented.

2.4 Pathological Aging

Pathological aging is the result of non-normative occurrences during aging brought on by trauma or disease in the brain (Reese, Cherry, & Copeland, 2010). While normative aging is also associated with specific levels of declining cognitive and physical health, such debilities are the result of natural aging processes. In addition, the changes in health associated with healthy aging are typically met with stability and lack clinical significance compared to pathological aging. With respect to the brain, pathological aging may refer to a whole host of age-dependent

illnesses, the most common being dementia; more specifically Alzheimer's disease dementia (Scheltens et al., 2016).

2.4.1 Alzheimer's Disease

Alzheimer's Disease (AD) is the leading cause of dementia and causes a progressive and profound loss of cognitive capabilities, often beginning with memory impairments. To date, it is estimated that 40 million people worldwide suffer from dementia (Prince et al., 2013). These figures are projected to double every 20 years. With respect to Canada alone, it is estimated that the number of Canadians living with AD will grow to 1.4 million by 2031 (Van Hoesen & Pandya, 1975a). Being a debilitating disease, AD poses a significant burden on an individual, their family, and the healthcare system itself. Due to its sheer impending magnitude, the identification of preventative measures, treatments, and biomarkers for AD diagnosis has been placed at the forefront of health and brain science research.

2.4.1.1 Symptomology

AD can present with a typical or an atypical presentation. Typical presentation of AD is characterized by profound memory impairments that are exacerbated over time (Scheltens et al., 2016). This usually begins with a mild forgetfulness which transitions into more serious inabilities to recall common details (e.g. names of family members, dates, street address, etc.). Speech issues also become apparent and word-finding as well as vocabulary troubles increase. In the same manner, profound issues are later met in executive functioning (e.g. skipping meals, loss of cleanliness, disorganized thought) such that individuals can no longer complete activities of daily living and therefore require constant care and support. Although less common, atypical AD presentation begins with language, visual, and executive impairments well before memory deficits are observed (Murray et al., 2011).

2.4.1.2 Clinical Assessment

Clinical diagnosis of AD first begins with obtaining history of a patient's cognitive problems and impairments from the patient themselves, in addition to primary caregivers and family. Aside from reported documentation, neuropsychological tests are also preformed throughout multiple time periods to clinically assess and evaluate disease severity and progression. A wide range of specific tests can be used to assess memory, language, learning, and executive functioning capabilities, however, global tests of dementia are more commonly used to clinically evaluate overall degree of dementia. Frequent tests include: the Questionnaire on Cognitive Decline in the Elderly (IQCODE; Quinn et al., 2014), Mini-Cog (Fage, Chan, & Gill, 2015), Mini-Mental State Examination (MMSE; Arevalo-Rodriguez & Smailagic, 2015) and the Clinical Dementia Rating (CDR; Morris, 1993). All assessments are questionnaire-based and vary on question style, administration length, and level of detail. For example the MMSE is a 30 point 5-10min interview probing for attention, recall, and language details. On the other hand, the CDR is a 3-point 45-50min interview that involves thorough evaluation of memory, attention, executive functioning, and daily life capabilities. Due to ease of administration and reliability of such assessments, such tests are frequently used for subject screening in clinical AD research studies.

However, clinical assessment does not only involve behavioural assessment. With the advent of neuroimaging, and discovery of genetic and CSF biomarkers, AD pathological changes can be measured *in vivo*. In fact, this has promoted the development of new clinical diagnosis standards set by the National Institute of Aging and Alzheimer's Association. This new set of criteria highlights the need of biomarker evidence in the form of either neuroimaging or CSF biomarkers, directly suggesting neuropathological changes associated with AD (Albert et al., 2011; McKhann et al., 2011; Sperling et al., 2011). For example protein analysis of CSF allows for the measurement of the concentration of the two main hallmarks of AD; the Amyloid beta (Aβ) and tau proteins (see 2.4.1.3 Pathophysiology). CSF protein concentration analysis have been reported to result in accurate and reliable AD diagnoses and are associated with cognitive decline (Mattsson et al., 2011; 2009). With respect to neuroimaging, Position Emission Tomography (PET) allows for the *in vivo* radioactive imaging of Aβ and has been shown to demonstrate the same Aβ retention as described in post mortem AD studies (Braak & Braak,

1997; Villemagne & Chételat, 2016). CSF and PET biomarker analyses are both invasive and laborious. Noninvasive *in vivo* structural MRI has also been used to identify structural AD biomarkers. MRI of the HF and cortical grey matter regions have been shown to be well associated with AD pathology (Frisoni, Fox, Jack, Scheltens, & Thompson, 2010).

2.4.1.3 Pathophysiology

Although the underlying pathophysiology of AD may be complicated and multi-causal in nature (Boyle et al., 2013), the main pathophysiological features include the existence of β-amyloid plaques and neurofibrillary tangles in the brain (Karran, Mercken, & de Strooper, 2011). Amyloid plaques result from the cleavage of the amyloid precursor protein (APP) to yield Aβ proteins that form extracellular deposits. These deposits and aggregations then become toxic to neighboring cells of the nervous system. Neurofibrillary tangles, another pathological hallmark of AD, occurs intracellularly as a result of hyperphosphorylation of tau proteins. This causes impaired axonal maturation and disrupts cellular processes, leading to improper axonal-dendritic connections and neural loss. Greatest evidence for Aβ and tau being implicated in AD originates from genetic studies of familial AD where mutations in the APP protein have been shown to affect Aβ cleavage and aggregation (Karch & Goate, 2015). In addition, mutations in presenilin 1 (PSEN1) and presenilin 2 (PSEN2) can result in familial forms of AD which are early-onset compared to most sporadic forms and account for a minority of AD cases. Subjects carrying these mutations demonstrate increased plaque formation early in their lifespan and have demonstrated that these plaques play a major role in the cleavage of APP to Aβ. Tau protein genetics are less understood but it is known that mutations in tau result in frontotemporal dementia Aβ aggregations (Scheltens et al., 2016).

Genes implicated in cholesterol metabolism has also been linked to Aβ plaque aggregation. Perhaps the most notable gene and strongest risk factor associated with AD risk is the Apolipoprotein (APOE) gene. APOE encodes three common alleles (ε 2, ε 3, ε 4), each is associated with consecutively increased AD risk (Corder et al., 1993; Strittmatter et al., 1993) with ε 4 have highest amount of associated risk. APOE plays several roles in the nervous system

including roles in cholesterol transport, neuroplasticity, and inflammation (Karch & Goate, 2015). Interestingly, APOE also binds to Aβ and influences its clearance.

2.4.1.4 Mild Cognitive Impairment

Mild Cognitive Impairment (MCI), first proposed by Petersen et al. (1999; 1997), has been characterized as a state of mild cognitive deficits without the presence of dementia. MCI is considered to be an intermediate stage prior to development of AD (Petersen, 2016). Symptomatically, MCI differs remarkably in comparison to AD and is characterized by mild forgetfulness and cognitive issues exceeding those found during healthy aging. While it has been thought of as a separate clinical entity likely representing a prodromal AD, its strong link to AD has motivated its increased research. Still in its early stages, little is known about MCI, its underpinnings, and its relationship to AD.

2.4.1.5 AD, MCI, and Hippocampal Subfields

As stated in section 2.4.1.2 'Clinical Assessment', MRI study of the HF and its progressive atrophy in AD has been increasingly studied for use as a biomarker. In addition, its role in memory processes make it a highly relevant structure for investigation in AD and MCI. While studies on whole-hippocampal shape have been performed in AD populations (Apostolova et al., 2006; Frisoni, Ganzola, Canu, Rüb, Pizzini, Alessandrini, Zoccatelli, Beltramello, Caltagirone, & Thompson, 2008b; Frisoni et al., 2006; Gerardin et al., 2009; Lindberg et al., 2012), the majority of studies preform volumetric analysis of hippocampal atrophy (Frisoni, Ganzola, Canu, Rüb, Pizzini, Alessandrini, Zoccatelli, Beltramello, Caltagirone, & Thompson, 2008b; van de Pol et al., 2006; Wang et al., 2009). The hippocampus is a major and primary site for neurofibrillary tangles and Aβ plaque deposition, and MRI-derived hippocampal volume decrease is closely related to neuronal decreases identified through histological validation (Bobinski et al., 2000; Gosche, Mortimer, Smith, Markesbery, & Snowdon, 2002; Jack et al., 2002). However, volumetric investigation at the level of hippocampal subfields is imperative. Global differences in observed whole-hippocampal volumes may be the result of regional differences in specific subfields of the HF. Identification of these subfields may not only identify viable and

appropriate biomarkers as well as treatment intervention targets, but may also shed light on subfield-specific roles in AD or MCI.

Previous high-resolution volumetric studies comparing the HF subfields in AD and control cohorts have identified decreases in subiculum, CA1, CA4/DG and SLRM volume (Adachi et al., 2003; Boutet et al., 2014; de Flores et al., 2015; La Joie et al., 2013). Among all volumetric results in AD, observed decreases in the CA1 region occur most frequently and are often the central focus in such studies (Adachi et al., 2003; Boutet et al., 2014; de Flores et al., 2015; Iglesias et al., 2015; Kerchner et al., 2010; 2013; Khan et al., 2015; La Joie et al., 2013; Li, Dong, Xie, & Zhang, 2013; Lim et al., 2012; Mueller et al., 2010; Mueller & Weiner, 2009; Wisse et al., 2014; Yassa et al., 2010; Yushkevich, Pluta, et al., 2015b). Studies employing automatic segmentation have also been completed (Khan et al., 2015; Li et al., 2013; Lim et al., 2013) and have demonstrated decreases in the subiculum, CA2/3, CA2/DG and CA1. With respect to MCI, some studies fail to show any volumetric changes (Kerchner et al., 2013; Wisse et al., 2014) yet a select few point towards focal decreases in CA1 (Mueller et al., 2010; Mueller & Weiner, 2009), CA3/DG, CA4/DG and/or the subicular subfields (de Flores et al., 2015; La Joie et al., 2013; Pluta et al., 2012).

2.4.1.6 AD, MCI, and White Matter

Accelerated levels of extra-hippocampal WM atrophy are known to be associated with AD progression (Callen, Black, Gao, Caldwell, & Szalai, 2001; Copenhaver et al., 2006). With minimal studies focusing on volumetric data, a wide range of diffusion weighted imaging (DWI) studies have shown decreases in fornix integrity (Jin, Shi, Zhan, & Thompson, 2015; Metzler-Baddeley, O'Sullivan, Bells, Pasternak, & Jones, 2012; Nowrangi, 2015; Oishi, Mielke, Albert, Lyketsos, & Mori, 2012; Zhuang et al., 2013). DWI capitalizes on the diffusion of water molecules along axons to successfully image fiber tracts *in vivo* (Mizutani & Kasahara, 1995). DWI work has also implicated the fornix in MCI (Huang et al., 2012; Mielke et al., 2009; Oishi et al., 2012). The use of DWI over volumetric investigation of extra-hippocampal WM integrity has largely been motivated by the time-dependent costs associated with segmentation of WM regions. However, DWI is limited in resolution due to a number of methodological factors and

cannot be used to successfully investigate alveus and fimbria regions. Albeit few, existing volumetric studies have (Cui et al., 2012), and have not (Copenhaver et al., 2006) shown evidence of decreases in fornicial volume. With respect to volumetric investigation of the fimbria, mixed evidence suggests both atrophy and preservation over MCI (Hanseeuw et al., 2011; Iglesias et al., 2015; Khan et al., 2015; Lim et al., 2012; Yushkevich, Pluta, et al., 2015b) and AD (Frisoni et al., 2006; Khan et al., 2015; Li et al., 2013; Lim et al., 2013). While no study has sought to investigate the volumetry of the alveus directly, automatic segmentation studies have reported volumetric decreases of the alveus in AD (Boutet et al., 2014) but not in MCI (Iglesias et al., 2015).

2.4.1.7 AD Treatment

Current therapeutic approaches for the treatment and management of AD have largely focused on pharmacological methods. To date, four FDA-approved drugs have been developed for the treatment of AD. These include cholinesterase inhibitors (donepezil, rivastigmine and galantamine) and a glutamate antagonist (memantine; Scheltens et al., 2016). Both function to increase the presence of the neurotransmitter acetylcholine. This largely stems from the notion that acetylcholine decreases associated with age were thought to underlie the changes associated with AD. Although clinical studies have shown some effect, effects are typically marginal and may only stabilize symptoms during the first year of treatment (Birks, 2006). Novel approaches for AD treatment have focused on anti-amyloid techniques to reduce the presence of Aβ plaques. These include anti-aggregation drugs and drugs that inhibit the cleaving of APP to from Aβ. Unfortunately current clinical evaluation of such interventions shows absolutely no effect in mediating changes to AD behavior, pathology, or atrophy (Coric et al., 2012; Doody et al., 2013; 2014; Salloway et al., 2014). In addition, no approved treatments have been put forth for MCI, and have largely focused on the change of numerous lifestyle factors (Petersen et al., 1997).

While pharmacological treatment options have not shown much promise, more invasive treatment options targeting circuitry and plasticity of MTL areas are currently under development. Namely, Deep Brain Stimulation (DBS) as a treatment option for AD is now being explored in clinical trials (Gratwicke et al., 2013). DBS involves the implant of a

stimulating electrode in the anterior limbs of the fornix. Electrical stimulation can then be administered at specific frequencies and rates. Initial results show promise with DBS exhibiting an effect of decreased rates of hippocampal atrophy among patients, as well as eliciting hippocampal growth in a number of cases (Sankar et al., 2015).

2.5 Healthy Aging

Healthy aging is described as normative aging that occurs without the presence of significant cognitive decline. Changes in brain structure are also observable throughout healthy aging with the brain showing fluctuating but increased atrophy throughout age (Raz & Rodrigue, 2006; Sowell et al., 2003). In addition, there is evidence that the atrophy observed throughout aging closely correlates to the mild decreases in cognitive function observed throughout healthy aging (Fjell & Walhovd, 2010; Lockhart & DeCarli, 2014). Most often the study of healthy aging occurs alongside that of AD, and with the frequent comparison of AD to healthy aging cohorts (de Flores et al., 2015). While no alternative comparison exists as a baseline measure, it is important to understand that differences in brain structure between healthy and pathological aging have not been fully defined. Moreover, it is difficult to distinguish healthy brain changes with preclinical stages of AD or MCI (Fjell, McEvoy, Holland, Dale, & Walhovd, 2014). Elucidating the effect of normative aging on brain structure would provide a more coherent picture of what "baseline" normal aging is taken to be. Similar to work in AD and MCI, amongst other regions, the HF remains an area of increased interest in the study of aging.

2.5.1 Aging and Hippocampal Subfields

While global hippocampal atrophy is known to increase with age (Jack, Petersen, Xu, O'Brien, & Smith, 1998), post mortem studies have also identified varying rates of neuronal losses in hippocampal subfields throughout age (Simić, Kostović, Winblad, & Bogdanović, 1997; West, Coleman, Flood, & Troncoso, 1994). Attempts have been made to investigate the HF *in vivo*, however they have been limited to MRI methods of looking at global shape change (Csernansky et al., 2000; Wang et al., 2003; Yang, Goh, Chen, & Qiu, 2013) and radial atrophy (Apostolova et al., 2012; Frisoni, Ganzola, Canu, Rüb, Pizzini, Alessandrini, Zoccatelli, Beltramello,

Caltagirone, & Thompson, 2008a; Wang et al., 2006). However, these methodologies cannot target individual subfields themselves. Similar to *in vivo* MR work in AD and MCI, volumetry of the subfields may be more useful.

Compared to the study of AD and MCI, the investigation of hippocampal subfields with respect to healthy aging has been relatively limited. Despite this, many studies investigating HF subfields throughout age support the preservation of the CA1 region (La Joie et al., 2010; Mueller et al., 2007; Voineskos et al., 2015). However, numerous studies have demonstrated an opposite and linear decrease in CA1 volume throughout age (Mueller et al., 2007; Mueller & Weiner, 2009; Raz, Daugherty, Bender, Dahle, & Land, 2015; Shing et al., 2011; Wisse et al., 2014). Other studies have used semi-automated methods (Kerchner et al., 2013) to show linear decreases in CA1 volume, while a recent automated investigation revealed no effect throughout age (Pereira et al., 2014). Results regarding the CA4/DG are mixed with both decreases (Mueller & Weiner, 2009; Pereira et al., 2014; Wisse et al., 2014) and preservation (de Flores et al., 2015; Kerchner et al., 2013; Mueller et al., 2007; Raz et al., 2015; Shing et al., 2011) observed.

2.5.2 Aging and WM

No study to date has sought to fully address changes in all WM regions (i.e. alveus, fimbria, and fornix) of the memory circuit. While some volumetric studies investigating the fimbria have shown no change in volume across age (Frisoni, Ganzola, Canu, Rüb, Pizzini, Alessandrini, Zoccatelli, Beltramello, Caltagirone, & Thompson, 2008a; Pereira et al., 2014), the fornix has only received extensive attention in DWI studies. Quantitative fiber tracking results showing age-dependent reductions in fornicial structure (Schmahmann et al., 2007; Zahr, Rohlfing, Pfefferbaum, & Sullivan, 2009) along with more recent DWI studies (Fletcher et al., 2013; Gunbey et al., 2014; C. Lebel et al., 2012; Sala et al., 2012; Sasson, Doniger, Pasternak, Tarrasch, & Assaf, 2013; Sullivan, Rohlfing, & Pfefferbaum, 2010).

2.6 Present Study Approach

This thesis first evaluates and describes a protocol for the manual segmentation of HF WM, and validates its use in an automatic segmentation framework (MAGeT Brain). This framework is then used to automatically segment WM and HF subfields in a population of healthy and pathological (i.e. MCI, AD) aging. Chapter 3 identifies the main materials and methods used in the study. This includes a description of the segmentation protocol, datasets used, and analysis techniques employed. In Chapter 4, all results of the statistical and analytical tests are reported, including the reliability outcomes of manual segmentations, validation results, as well as the volumetric results for healthy versus pathological aging. Results are discussed and critically evaluated in Chapter 5.

Chapter 3: Methods

Three main methods were used to produce the final contributions of the present thesis. The first involves a description of the detailed manual segmentation protocol defined for the WM (alveus, fimbria, and fornix) of the HF; the second is the validation of this protocol for use in a fully automated segmentation scheme; and the final is the application of the automated protocol on the OASIS and ADNI datasets to study healthy and pathological aging respectively.

3.1 Atlas Image Acquisition

High-resolution T1- and T2-weighted images used for the development of our manual segmentation protocol are from data acquired from 5 healthy subjects (2 male, 3 female, aged 29-57, average age of 37 years). All images were acquired on a 3T GE Discovery MR 750 system (General Electric, Milwaukee, WI) at the Centre for Addiction and Mental Health (Toronto, Canada) using an 8-channel head coil. Three separate sets of high-resolution T1 and T2-weighted images were acquired. T1-weighted images were acquired using the 3D inversion-prepared fast spoiled gradient-recalled echo acquisition (FSPGR-BRAVO; TE/TR = 4.3 ms/9.2 ms, TI = 650 ms, $\alpha = 8°$, 2NEX, FOV = 22 cm, slice thickness = 0.6 mm, 384 × 384 in-plane steps). High-resolution T2-weighted images were acquired using the 3D fast spin echo acquisition (FSE-CUBE; TE/TR = 95.3 ms/2500 ms, ETL = 100 ms, 2NEX, FOV = 22 cm, slice thickness = 0.6 mm, 384 × 384 in-plane steps). Both image sets have an isotropic voxel size of 0.6 mm. A final isotropic voxel size of 0.3 mm was obtained for both T1 and T2 images using reconstruction filters, ZIPX2 and ZIP512. All images were converted to the MINC file format and subsequent image processing and neuroanatomical labeling was performed using tools from the MINC software distribution (http://www.bic.mni.mcgill.ca/ServicesSoftware/HomePage).

Each image was corrected for RF inhomogeneity non-uniformity (Sled et al., 1998) and the three T1 and T2-weighted images were averaged together following rigid-body alignment (Collins, Neelin, Peters, & Evans, 1994) in order to decrease noise and increase contrast. Each image was then normalized to a fixed intensity range (0–10,000), and intensity-averaged on a voxel-by-voxel basis to enhance signal and contrast (Holmes et al., 1998) to produce one final T1, and T2-

weighted image volume. T1- and T2-weighted averages were then rigidly aligned to one another (Collins et al., 1994) to allow for neuroanatomical homology between the contrasts.

3.2 Manual Tracing Protocol

Whereas past protocols have only involved manual tracings of the fornix, the present work seeks to delineate the left and right alveus, fimbria, and fornix using the high-resolution images described above. In addition, the protocol is tailored to fit with a previously published protocol for segmentation of the HF subfields by our group (Winterburn et al., 2013). A variety of different anatomical papers and print atlases were used to create the WM atlases (e.g. Duvernoy et al., 2013; Mai et al., 2015; Talairach & Tournoux, 1988). All tracings were completed using the Display software package (part of the MINC toolkit: http://www.bic.mni.mcgill.ca/ServicesSoftware/HomePage). In general, contrast differences were used to discern the WM from the HF grey matter and surrounding structures. In areas of anatomical uncertainty, geometrical rules were applied to maintain a consistent approach that approximates the known neuroanatomy while allowing the protocol to be effectively replicated by others; a strategy successfully employed by our group (Park et al., 2014; Winterburn et al., 2013) and others (Ekstrom et al., 2009; Kerchner et al., 2010; La Joie et al., 2010; Libby, Ekstrom, Ragland, & Ranganath, 2012; Malykhin et al., 2010; Mueller & Weiner, 2009; Palombo et al., 2013; Pluta et al., 2012; Preston et al., 2010; Pruessner, Li, Serles, Pruessner, Collins, Kabani, Lupien, & Evans, 2000a; Wisse et al., 2012; Yushkevich et al., 2009; 2010). Similarly, this has also been the case for the application of histologically derived MR atlases (Adler et al., 2014) where visual inspection of such atlases has also been used in conjunction with other atlases to approximate borders of HF subfields in head and tail sections (Yushkevich, Pluta, et al., 2015b). Although T1-weighted scans were mainly used to guide segmentation, T2-weighted scans proved useful as a second anatomical reference (most notably in areas where the T2 contrast provided more visibility; e.g. the anterior pillars of the fornix or WM posterior to the crux of the fornix). Given that the present WM structures have a complex three-dimensional shape (e.g. fornix twists and turns in and out of various planes), all views were employed to aid delineation. Some of the WM structures may be more visible in one plane (i.e. sagittal, coronal, axial) than another. For similar reasons, 3D surface representations of segmentations were used to guide tracing in ambiguous areas and to enforce strict neuroanatomical homology. The

description provided below represents only a summary of the devised tracing protocol. A comprehensive version of the protocol with specific written guidelines per structure and corresponding 17 anatomically detailed images, can be found in Appendix A.

Alveus: Identification of the alveus begins in the coronal plane in the anterior to posterior direction (all other planes including 3D reconstruction were used to aid tracing). At its most anterior extremity, the alveus first appears as a circular/oval shape approximately 1mm prior to the emergence of the HF head as previously identified by (Winterburn et al., 2013). At this point, all high-intensity WM voxels (similar to those of the corpus callosum or anterior commissure) are included as alveus; the superior border being the grey matter of the amygdala, and inferior border being the WM superior to the entorhinal and perirhinal cortices. Once the HF head emerges, the alveus sits atop the HF and is inferiorly bounded by the grey matter ribbon of the CA region (see Figure 3A, i). Since the WM of the alveus blends inferiorly with that of the WM superior to the parahippocampal gyrus, an approximation is made such that the alveus extends superiorly on the HF from the lateral-most extent of the HF to the medial most extent (see Figure 3A, ii, iii). In more posterior slices, the HF shifts superiorly towards the lateral ventricle. At this point the WM of the alveus extends more laterally and blends with the WM inferior to the HF. In order to ensure inclusion of voxels contained within the alveus, the lateral boundary is taken to be the point at which the WM of the alveus meets the floor of the lateral ventricle (Figure 3B, iv). Medially, the alveus is traced until it is no longer visible. While the inferior boundary remains the same as in previous slices, the superior boundary at this point now becomes the cerebrospinal fluid (CSF) of the lateral ventricle. For the most part, the alveus maintains the same boundaries from the HF body to the tail, running laterally and superiorly along the HF. Following the disappearance of the uncus of the HF head, the WM of the alveus and fimbria become indistinguishable at the level of the HF body. Here, a geometric rule was devised to separate these two regions. This involved bisecting the entire WM ribbon superior to the HF with a vertical line down the middle of the top most undulation of the HF body (see Figure 3C, v). This measurement was taken to be the half-way point between the medial end of the CA4/DG (i.e. the medial-most termination of CA4/DG and the stratum radiatum, lacunosum and moleculare (SR/SL/SM) subregions as defined by Winterburn et al. (2013)) and the lateral most point of the HF WM, which extends out into the lateral ventricle. All WM occurring lateral

to this vertical line was demarcated as alveus. In posterior sections near the HF tail, the high intensity signal contrast of the WM ribbon begins to decrease with each consecutive slice until it completely disappears. Segmentation of the alveus therefore terminated on the last slice on which it was discernible.

Fimbria: Moving along the HF from anterior to posterior in the coronal plane, segmentation of the fimbria begins once the uncal sulcus appears. In the case of the fimbria, all cardinal orthogonal planes were used to aid tracing. Similar to the alveus, the fimbria is superiorly bordered by the CSF and inferiorly bordered by the grey matter of the uncus of the HF head. At the level of the uncus, the fimbria extends laterally until it reaches the lateral most undulation of the HF. This point coincides with the medial termination of the CA2/3 and DG/CA4 regions in our previous HF subfield atlas (Winterburn et al., 2013). The fimbria continues medially until the high intensity WM ribbon is no longer visible. In more posterior coronal sections, the fimbria begins to separate from the uncus and is flanked by the alveus. At the level of the HF body, a vertical line is drawn bisecting the WM ribbon on top of the HF, exactly half-way up the lateral-most undulation of the HF (Figure 3C, v). All WM medial to this line is included as fimbria. All other border definitions remain the same. Tracing of the fimbria continues until the crux of the fornix is in full view coronally (Figure 3E, vi).

Fornix: Tracing of the fornix begins in the coronal plane once the crux of the fornix is in full view (Figure 3E, vi). All other planes including 3D surface representations were also used to aid tracing. At this point, the fornix is bound inferomedially by the pulvinar nucleus of the thalamus and by the CSF of the quadrigeminal cistern. Since the WM of the fornix blends superiorly with the WM of the corpus callosum (Figure 3E, vii) and the commissure of the fornix, a reliable geometric rule to maintain tracing accuracy was employed. This involved tracing the WM along the angle where the fornix meets the superior WM from its lateral to medial edge (Figure 3E, red line). The lateral boundary of the fornix at this point is the medial edge of the alveus. In more posterior sections the WM of the fornix becomes removed from the WM of the corpus callosum and is traced until it is no longer visible. Tracing in the coronal plane ensues anterior to the crux of the fornix where the fornix moves superiomedially and anteriorly. The fornix takes a flattened appearance as its inferior, medial, and lateral aspects are all bordered by the CSF of the lateral

ventricle. Here, the superiomedial border is the same as listed previously (Figure 3I, red line). The fornix then detaches from the corpus callosum (Figure 3H, viii) and tracing includes only the condensed area of high-intensity WM. These demarcations continue throughout the body of the fornix coronally until the anterior pillars of the fornix are reached (Figure 3F). At this point, the fornix moves inferiorly in two separate columns to meet the mammillary bodies. At this point, the axial view of the T2-weighted images is best used to trace WM of the fornix.

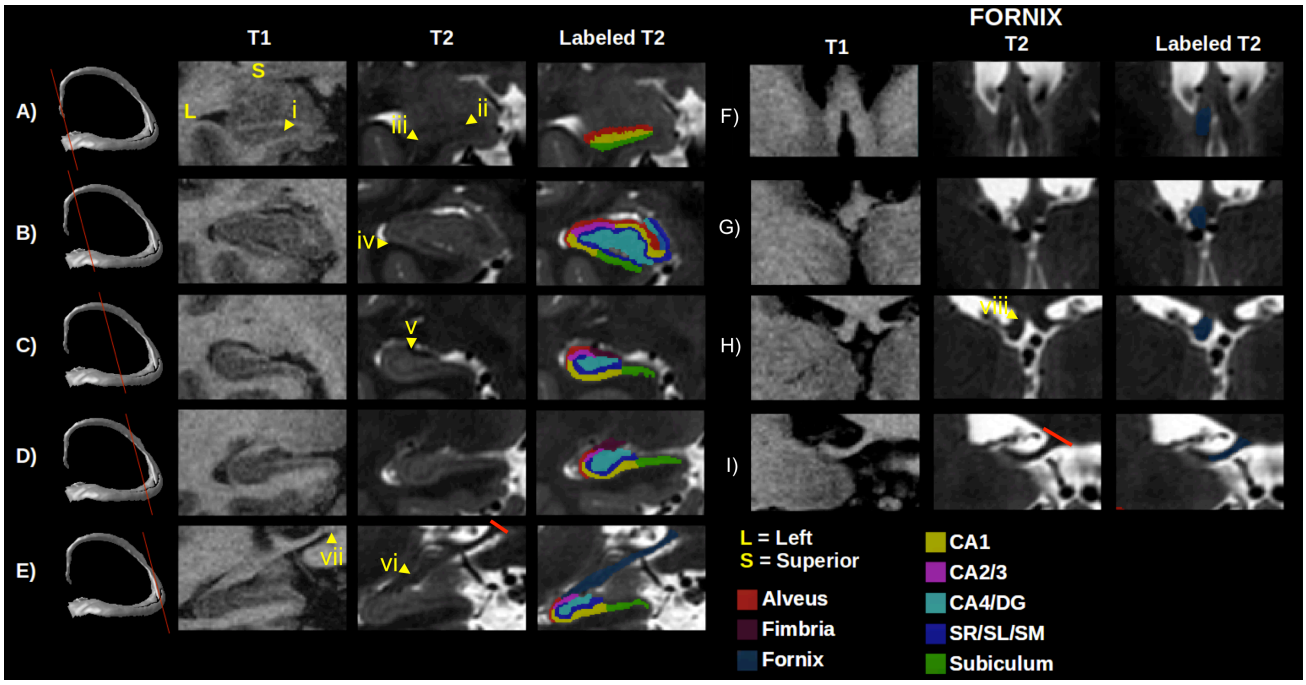

Figure 3. Example of segmentation protocol for the alveus fimbria and fornix. Columns A-E show unlabeled coronal slices for the white matter regions. Representative slices of the fornix are also included in rows F-I. White matter labels are presented along side hippocampal subfield labels from Winterburn et al. (2013). Both T1 and T2 images were cross-referenced during tracing. Sagittal and axial sections were also used to guide tracing. A) Depicts tracing protocol for the alveus at the level of the anterior HF head region. The alveus is bordered superiorly by the grey matter of the amygdala and inferiorly by the grey matter of the hippocampus (i). Sitting on top of the hippocampus, it includes the white matter ribbon extending from the most medial extension of the hippocampus (ii) to the most lateral extension of the hippocampus (iii). B) Shows segmentation protocol for the alveus in the head of the hippocampus. The alveus is bordered superiorly by the cerebrospinal fluid (CSF) of the lateral ventricle, and inferiorly by the hippocampus. It extends medially over the hippocampal undulations until it is no longer visible. Laterally the alveus is traced until it reaches the point where it meets the end of the lateral ventricle (iv). C) The alveus maintains the same border definitions except for its medial extent. Due to the presence of the fimbria, the alveus continues medially half-way up the top most undulation of the hippocampal body (v). The white matter ribbon medial to this extent is taken to be fimbria. D) Coronal slice though more posterior regions of the hippocampal body. E) The fimbria is traced until the presence of the crux of the fornix (vi), while the alveus remains. At this point the fornix is continued superiomedially until it meets the white matter of the corpus callosum (vii). F) Anterior pillars of the fornix. Axial sections were most useful in identifying the anterior pillars of the fornix as they descend inferiorly to reach the mammillary bodies. G) Coronal section through the body of the fornix. All high intensity white matter of the fornix is included in segmentation. H) Coronal section through the posterior body of the fornix. The fornix at this level is surrounded by CSF. I) A section though the posterior fornix just prior to the crux of the fornix. Superomedially the fornix follows the same rule as in vii.

3.3 Reliability of Manual Segmentation

The alveus, fimbria, and fornix of all 5 high-resolution scans were segmented using the protocol described above. Both intra and inter-rater reliability was assessed and consisted of retracing three randomly selected brains bilaterally. In order to reduce artificial increases in accuracy due to rater memory, all manual segmentations were completed 6-18 months after completion of initial segmentations by two separate individuals: one who developed the majority of the protocol and another who was taught the protocol *de novo* based on the description provided herein. Both tracers used not only the same tracing program (MINC Display) and style (i.e. mouse and keyboard), but also maintained the same screen size, resolution and image intensities across all tracings. Reliability for WM regions was measured using Dice's Kappa (Dice, 1945), which measures the degree of overlap between test and re-test labels (1 = full overlap, 0 = no overlap).

3.4 Investigation of the Memory Circuit in Healthy and Pathological Aging

3.4.1 Healthy Aging Dataset: OASIS

The OASIS cross sectional dataset was used to assess variation in WM (i.e. alveus, fimbria, and fornix) through the course of healthy aging (Marcus et al., 2007). A composite dataset, OASIS includes T1-weighted images from a total of 416 participants aged 18-96 scanned at 1.5T (3-5 scans per subject at 1 x 1 x 1.25mm, then rigidly registered, averaged, and resampled to 1mm isotropic voxel dimensions). Clinical Dementia Rating (CDR) scores were provided for each subject where 0 = no dementia, 0.5 = very mild dementia, 1= mild dementia, 2 = moderate dementia (Morris, 1993). To ensure that individuals suspected of having Alzheimer's disease or any existing cognitive impairment were excluded, 100 individuals with CDR scores greater than 0 were removed. A total of 316 individuals were used in the final analysis (aged 18-94; mean = 45.17, SD = 23.88, 62.3% female, CDR=0; see Appendix B: Population Demographics for age/sex distributions).

3.4.2 Pathological Aging Dataset: ADNI1 3T baseline

Pathological aging data used in this article were obtained from the Alzheimer's Disease Neuroimaging Initiative (ADNI) database (adni.loni.usc.edu). The ADNI was launched in 2003 as a public-private partnership, led by Principal Investigator Michael W. Weiner, MD. The primary goal of ADNI has been to test whether serial magnetic resonance imaging (MRI), positron emission tomography (PET), other biological markers, and clinical and neuropsychological assessment can be combined to measure the progression of mild cognitive impairment (MCI) and early Alzheimer's disease (AD). For up-to-date information, see www.adni-info.org. The ADNI1 3T baseline dataset was used to assess the role of WM in pathological aging. This provided a healthy control group of 47 individuals (mean age = 75.11, SD = 3.90, 61.70% females), an MCI group of 69 (mean age = 75.01, SD=8.18, 36.23% females) and an AD group of 35 (mean age = 74.23, SD = 7.93, 65.71% females; see Appendix B: Population Demographics for age/sex distributions) for a total of 151 individuals. Similar to the OASIS scans, all T1-weighted images maintained a 1mm isotropic voxel resolution.

3.4.3 Image Pre-Processing

In order to facilitate the downstream segmentation pipeline, OASIS images underwent pre-processing with N4 nonuniform intensity normalization (Tustison et al., 2010) followed by neck cropping. Preprocessed ADNI1 3T baseline data (i.e. gradwarp, B1 non-uniformity and N3 correction; Sled et al., 1998; Zheng et al., 2009) were cropped to remove the neck.

3.5 Automatic Segmentation: MAGeT-Brain Segmentation

Multiple automatically generated templates (MAGeT) Brain segmentation (Chakravarty et al., 2013; Pipitone et al., 2014) was used in conjunction with the 5 high-resolution atlases to derive automatically generated segmentations of the subfields and WM of the HF. MAGeT Brain was implemented with a total of 21 templates (both for OASIS and the ADNI datasets; as per Pipitone et al., 2014). Using nonlinear registration (Avants, Epstein, Grossman, & Gee, 2008) each atlas was used to label each template library image. Each subject was then labeled using

nonlinear registration between each image in the template library, yielding 105 (5 atlases x 21 templates) possible candidate segmentations for each subject. These candidate labels were then fused via majority vote to create the final label. Images in the template library were chosen to represent the demographic spread within each cohort under study. OASIS templates maintained a mean age of 42.70 (SD = 21.18 years and 52.38% female). For the ADNI cohort, templates chosen maintained a mean age of 74.23 (SD = 7.20, 52.38% female; 4 healthy controls, 12 MCI, and 5 AD). All 466 MAGeT-Brain outputs (315 OASIS, 151 ADNI) were assessed for quality via manual inspection on a slice-by-slice basis. Quality control was based on specific set of rules where each segmentation was assigned either a score of 0 (fail), 0.5 (good pass), or 1 (excellent pass; see Appendix C for quality control procedure).

3.6 Reliability of automatic segmentation

Although MAGeT-Brain has been previously validated for HF segmentation (Pipitone et al., 2014), an additional validation effort was made in order to verify if the WM regions defined above could be identified on standard 1mm isotropic T1-weighted acquisitions. In order to test the reliability of the MAGeT-Brain labels, MAGeT labels were generated from the OASIS reliability dataset (consisting of 30 individuals scanned twice with a delay of 1-89 days). A total of 20 individuals were used after exclusion for possible pathological conditions (see Section 3.4.1). Intraclass correlation coefficient (ICC) was used to assess the degree of correlation between the labels generated from the first and the second scan. Although this would provide a measure of precision, in order to test the accuracy of MAGeT brain segmentation, individual subject first scans were rigidly registered to the second scan (with 6 degrees of freedom; Avants et al., 2008). Resulting transformations were used to transform the MAGeT labels calculated on the first scan of the subject into the space of the repeat scan. Dice's Kappa was used to assess the degree of overlap between labels where 0 represents no overlap and 1 represents perfect overlap between labels:

$$\kappa = \frac{2a}{2a + b + c}$$

Here, the number of voxels in both segmentations is denoted by a while $b + c$ represents the sum of voxels unique to each respective label. Although registration and resampling errors will

confound the quality of this evaluation, we use this to establish a possible lower bound on MAGeT Brain segmentation reliability in the context of labeling standard T1-weighted MRIs.

An additional test for precision was completed which involved the use of a modified leave-one-out-cross validation (LOOCV), similar to the simulation approach presented in our previous work (Pipitone et al., 2014). In this approach, each high-resolution T1-weighted atlas is downsampled to 1mm isotropic voxel dimensions, and automatically segmented using the remaining atlases. Similarly, the downsampled versions of the homologous manually derived labels are used as a gold standard for segmentation against automated evaluation. Each LOOCV round involved the selection of a single downsampled atlas image treated as a subject image to be segmented by MAGeT-Brain. Given that the final step of the MAGeT-Brain pipeline involves a majority vote and that an odd number of input atlases improves segmentation (Pipitone et al., 2014), all combinations of three input atlases were used. Thus, each downsampled atlas is segmented once using each possible combination of 3 of the 4 high-resolution atlases. Therefore, for each of the five atlases, a total of 4 segmentations were evaluated per run, resulting in combined total of 5 x 4 = 20 segmentations evaluated overall. The template library was composed of all 5 downsampled atlases as well as 14 OASIS scans. Dice's Kappa was calculated for each of the 20 segmentations per region (via comparison to the downsampled gold standard labels).

3.7 Whole-Brain Volume Estimation

The OASIS and ADNI datasets include estimates of total intracranial volume (eTIV; as derived from FreeSurfer) and were used in subsequent analyses. Recently, an arguably more robust measure of total brain volume, brain extraction based on a nonlocal segmentation technique (BEaST; Eskildsen et al., 2012), has also been used in recent literature for providing whole-brain measures. Although results presented in the present paper include those using the eTIV as provided with each dataset, results were additionally run using BEaST outputs as a complementary measure (See Appendix D).

3.8 Statistical Analysis

A general linear model (GLM) accounting for sex and eTIV was used to assess the relationship between volumes of the structures and age in the OASIS dataset. Models assessing age by sex interactions as well as the presence of quadratic and cubic effects of age were also assessed. Analysis was performed for the entire HF (i.e. combined subfields) and WM circuit (i.e. combined WM regions) first as a whole, then repeated for individual HF subfields and WM structures. Effect sizes (standardized ß values) were calculated for each region. Multiple comparisons between all 16 subregions of the memory circuit were corrected for using Bonferroni correction (here, corrected threshold corresponds to $p < 0.0031$; uncorrected p values are also reported). Pair-wise structural correlations were also assessed to test for volumetric relationships between all WM or HF subregions to determine if there were any significant subregion grouping patterns in the normative neurodegenerative process or if pairs of subfields and HF WM regions degenerated with a consistent patterning. Prior to correlation analyses, volumes were first residualized for effects of age, sex and eTIV. A correlation matrix was generated with a bootstrap of 10,000 iterations for matrices of the left and right volumes separately, and 100,000 times for the bilateral correlation matrix.

In the ADNI data, a GLM accounting for age, sex and eTIV, was used to assess differences in volume across controls, MCI, and AD groups. Once again, correction for multiple comparisons yielded a Bonferroni corrected significance level of $p < 0.0031$ and standardized ß values were also obtained for each region.

Chapter 4: Results

4.1 Protocol Reliability

Intra-rater reliability values evaluated though Dice's Kappa revealed high reliabilities for WM regions, ranging from 0.81-0.90 (see Table 1). In addition, the assessment of inter-rater reliability demonstrated that reproducibility of the manual tracing protocol was high with Dice's kappa ranging from 0.81-0.87 (Table 1). The above results were comparable to those frequently reported and accepted in HF subfield literature (de Flores et al., 2015; Mueller et al., 2010; Olsen et al., 2013; Palombo et al., 2013; Winterburn et al., 2013; Wisse et al., 2012). Three-dimensional rendering was also used to qualitatively assess morphometric contiguity and was found to be of sufficiently smoothly contours (See Figure 4).

Table 1. Summary of Intra/Inter-rater Reliability

Structure	**Left Dice Score**		**Right Dice Score**	
	Intra (range)	Inter (range)	Intra (range)	Inter (range)
Alveus	0.88 (0.90-0.85)	0.87 (0.89-0.85)	0.86 (0.90-0.75)	0.85 (0.86-0.83)
Fimbria	0.90 (0.92-0.89)	0.85 (0.87-0.83)	0.81 (0.86-0.71)	0.81 (0.84-0.77)
Fornix	0.89 (0.90-0.87)	0.81 (0.82-0.80)	0.84 (0.88-0.76)	0.81 (0.81-0.80)
Total White Matter	0.90 (0.90-0.89)	0.81 (0.84-0.75)	0.84 (0.89-0.76)	0.80 (0.86-0.74)

Average intra and inter-rater reliability was calculated using Dice's volumetric Kappa. A score of 0 represents no overlap between test and retest labels, whereas a value of 1 represents a complete overlap.

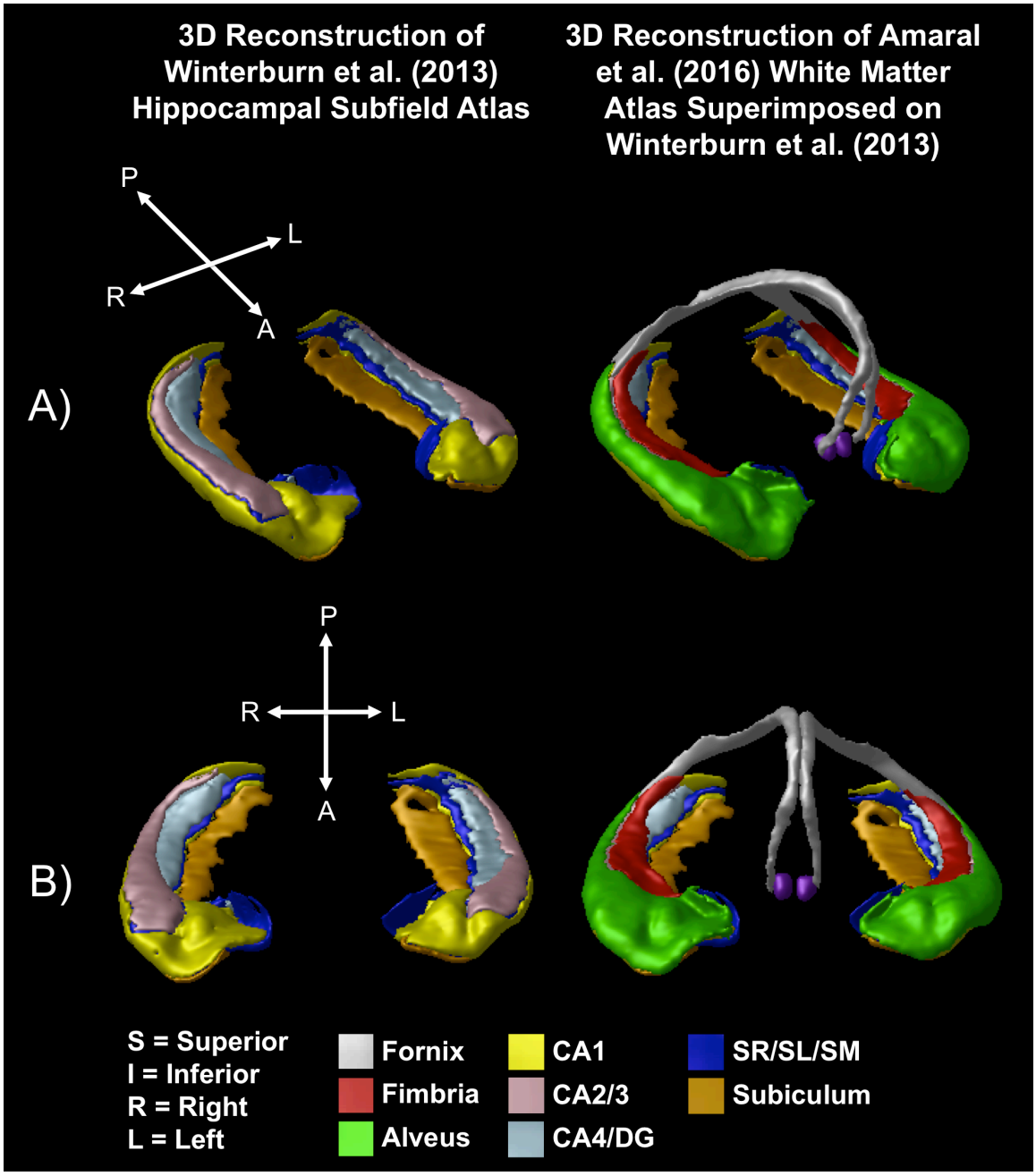

Figure 4. Three dimensional reconstruction of high-resolution hippocampal subfield and white matter atlases. Bilateral 3D reconstruction of the hippocampal subfields as per Winterburn et al. (2013) are depicted in the first column. The second column depicts the novel white matter labels superimposed on the Winterburn atlas. Row A) presents a lateral view of the bilateral hippocampi and white matter. Row B) presents a superior view of the hippocampal subfields and white matter.

4.2 Quality Control of MAGeT Brain Output

Segmentation quality control of the OASIS dataset resulted in 19 out of an initial 315 subjects (6.4%) being removed due to segmentation failure. ADNI quality control resulted in the exclusion of 6 individuals out of 151 (3.97%).

4.3 MAGeT Brain Reliability

Intraclass correlation coefficients (ICC) were used to assess the degree of correlation between the volumes generated from the first and the second OASIS scans. Results indicated a medium to high consistency for HF subfields and WM regions ranging from 0.79-0.99 (see Table 2; OASIS Validation). Dice's Kappa was used to assess the degree of overlap between labels and revealed values ranging from 0.61-0.84 (see Table 2; OASIS Validation). Results of the LOOCV analysis revealed Dice scores ranging from 0.30-0.70 for both HF subfields and WM structures. Although these validation results are comparable to previous work from our group for automatic HF subfields (Pipitone et al., 2014), results are lower than other groups (Van Leemput et al., 2009; Yushkevich et al., 2010; Yushkevich, Pluta, et al., 2015b). Despite this, it is important to note that validation efforts of the aforementioned groups have either 1) involved manual delineations of considerably fewer HF subfields, 2) traced HF subfields only along the body of the HF while excluding all WM regions, and 3) have only completed automated segmentation on high-resolution MR images (as opposed to the 1mm isotropic standard resolution used in the present study).

Table 2. Summary of MAGeT Brain Validation

Structure	Left			Right		
	OASIS Validation		LOOCV	OASIS Validation		LOOCV
	ICC (SD)	Dice (SD)	Dice (SD)	ICC	Dice (SD)	Dice (SD)
CA1	0.95	0.77 (0.03)	0.57 (0.05)	0.98	0.76 (0.03)	0.50 (0.04)
CA2 & CA3	0.94	0.63 (0.06)	0.32 (0.09)	0.95	0.63 (0.08)	0.35 (0.10)
Dentate Gyrus/CA4	0.96	0.84 (0.02)	0.65 (0.04)	0.94	0.82 (0.03)	0.56 (0.05)
SR/SL/SM	0.96	0.68 (0.03)	0.39 (0.05)	0.96	0.65 (0.04)	0.30 (0.05)
Subiculum	0.96	0.73 (0.04)	0.52 (0.10)	0.96	0.75 (0.04)	0.41 (0.07)
Alveus	0.93	0.65 (0.05)	0.39 (0.07)	0.96	0.61 (0.05)	0.33 (0.06)
Fimbria	0.96	0.73 (0.05)	0.49 (0.09)	0.91	0.69 (0.08)	0.39 (0.11)
Fornix	0.99	0.80 (0.02)	0.70 (0.04)	0.99	0.79 (0.03)	0.67 (0.04)
White Matter	0.98	0.73 (0.04)	0.53 (0.7)	0.99	0.70 (0.05)	0.46 (0.06)
Hippocampus	0.98	0.73 (0.04)	0.49 (0.7)	0.99	0.72 (0.04)	0.42 (0.06)

Reliability values were assessed for each structure per hemisphere. MAGeT Brain labels of 20 OASIS subjects scanned at two different time points were used to assess the accuracy of MAGeT Brain segmentation. Reliability was conducted using Intraclass Correlation (ICC) which assesses the degree of volumetric correlation between test and re-test volumes. A score of 0 represents no correlation, a value of 1 represents a perfect correlation. In order to assess the precision of MAGeT Brain segmentation, labels produced from the first scan of each subject were rigidly aligned to their respective repeat scan. Kappa values were then calculated once labels were in the same space. Average reliability was assessed using Dice's volumetric Kappa which assesses the degree of overlap between test and re-test volumes. A score of 0 represents no overlap, a value of 1 represents a perfect overlap between test and re-test labels. An additional validation of MAGeT Brain employed the use of a leave-one-out-corss-validation (LOOCV) to assess segmentation precision. Reliability was assessed again using Dice's Kappa.

4.4 OASIS Dataset

No significant associations with age were found for combined WM volumes (i.e. sum of alveus, fimbria, and fornix; Left: p=0.46; Right: p=0.82). Out of all WM subregions, we observed a surprising positive association between bilateral alveus volumes and age (Left: R^2=0.12, p<0.001; Right: R^2=0.097, p<0.001; see Figure 5 A). Decreases in bilateral fornicial volume through the adult lifespan were observed (Left: R^2=0.022, p=0.0012; Right: R^2=0.038, p<0.001; see Figure 5 C). The association between fimbria volume and age was less clear as the left

fimbria volume decreased (R^2=0.027, p=0.0011) and the right fimbria remained stable (p=0.91; see Figure 5 B) in relation to age.

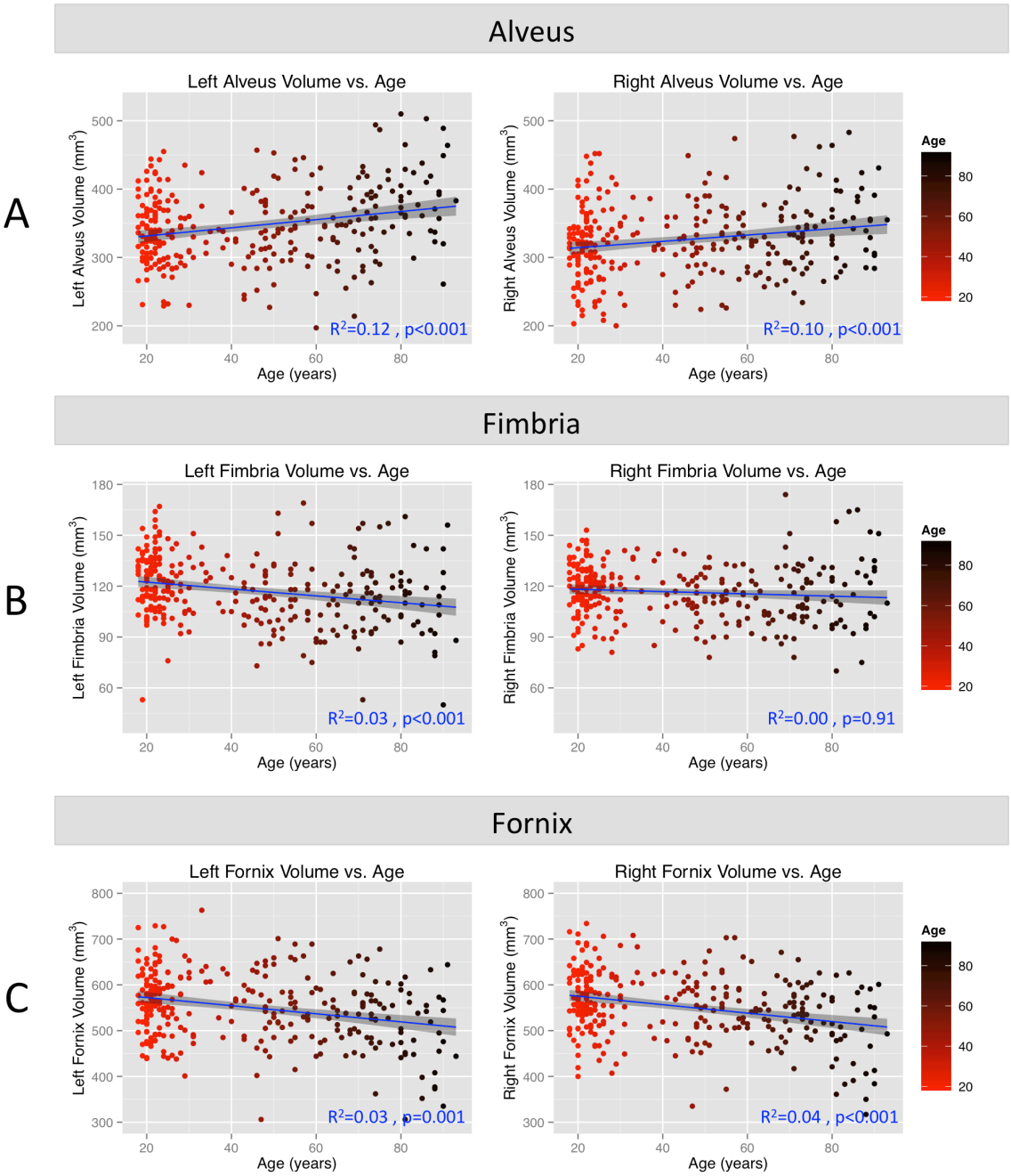

Figure 5. Weighted scatter plots of white matter subfield volumes across age for 315 OASIS cases. Regression lines plotted depict volume as a function of age. Statistics reported are for a general linear model (GLM) accounting for sex and estimated total intercranial volume (eTIV). A: Plot of alveus volume as a function of age. GLM accounting for sex and eTIV demonstrated bilateral volume increases in the alveus (Left: R^2=0.12, p<0.001; Right: R^2=0.10, p<0.001). B: Plot of fimbria volume as a function of age. GLM accounting for sex and eTIV demonstrated a significant decrease for only the left fimbria (R^2=0.03, p<0.001). The right fimbria was not significant (p=0.91). C: Plot of fornix volume as a function of age. GLM revealed a bilateral decrease in fornix

volume for both the left (R^2=0.03, p=0.001) and right (R^2=0.04, p<0.001) fornix. Plot depicts *p* and adjusted R^2 values.

No significant relationship was observed for age with respect to whole HF volume (Left: p=0.87; Right: p=0.077) following Bonferroni correction. Significant associations between age and some of the HF subfields were also observed. A positive association between age and volumes of left and right CA1 was found (respectively, R^2=0.044, p<0.001; R^2=0.0043, p<0.001; Figure 6 A). The left CA4/DG demonstrated a trend toward volumetric decrease associated with age (R^2=0.0073, p=0.035) while the right did not show any such association (p=0.937; Figure 6 B). The left SR/SL/SM was found to decrease over time (R^2=0.012, p=0.014; Figure 6 C), while the decrease in the right hemisphere did not reach significance. All linear models run using BEaST-derived total brain volumes did not deviate from findings reported above (see Appendix D for results).

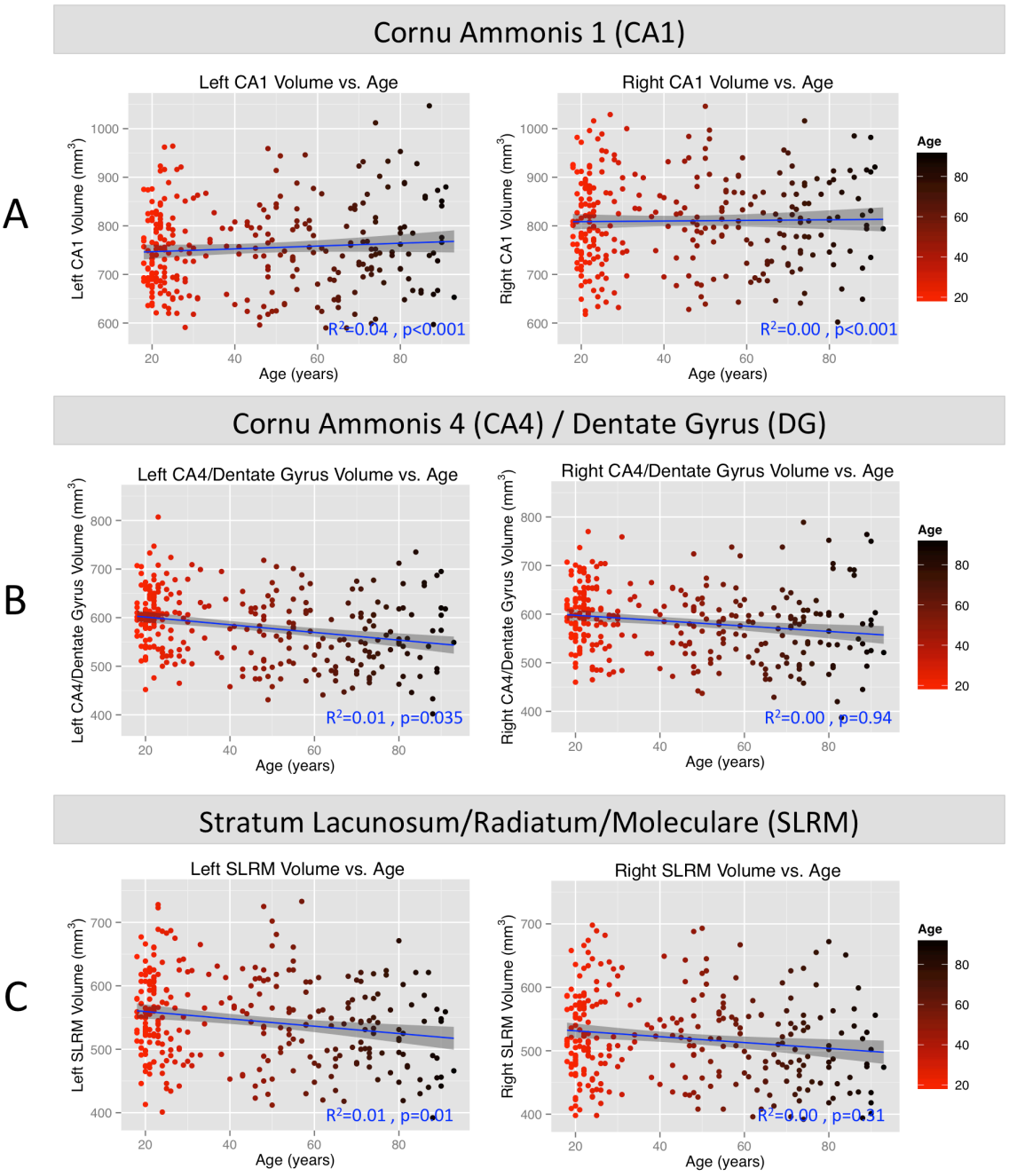

Figure 6. Weighted scatter plots of hippocampal subfield volumes across age for 315 OASIS cases. Regression lines plotted depict volume as a function of age. Statistics reported are for a general linear model (GLM) accounting for sex and estimated total intercranial volume (eTIV). A: Plot of CA1 region volume as a function of age. GLM accounting for sex and eTIV demonstrated bilateral volume increases in the CA1 region (Left: R^2=0.04, p<0.001; Right: R^2<0.001, p<0.001). B: Plot of CA4/DG volume as a function of age. GLM accounting for sex and eTIV demonstrated a significant decrease for only the left CA4/DG (R^2=0.01, p=0.035). The right CA4/DG was not significant (p=0.94). C: Plot of SR/SL/SM volume as a function of age. GLM revealed a bilateral decrease in SR/SL/SM volume for the left (p=0.01). The right SR/SL/SM showed no significant change (p=0.31). Plot depicts *p* values and adjusted R^2 values.

Bilateral increases of alveus volume over age maintained the largest effect size (left: ß =0.84; right: ß =0.73; see Figure 7). Largest negative effect sizes were observed for the left and right fornicial volumes (respectively, ß =-0.69; ß =-0.54). Out of all WM regions the left fimbria (ß =-0.15) showed the smallest effect size as it decreased in volume with age. Within the HF subfields, the bilateral CA1 region maintained the largest positive effect size (left: ß =0.82; right: ß =0.94) and largest negative effect sizes observed for the left CA4/DG (ß =-0.32) and left SR/SL/SM (ß =-0.39).

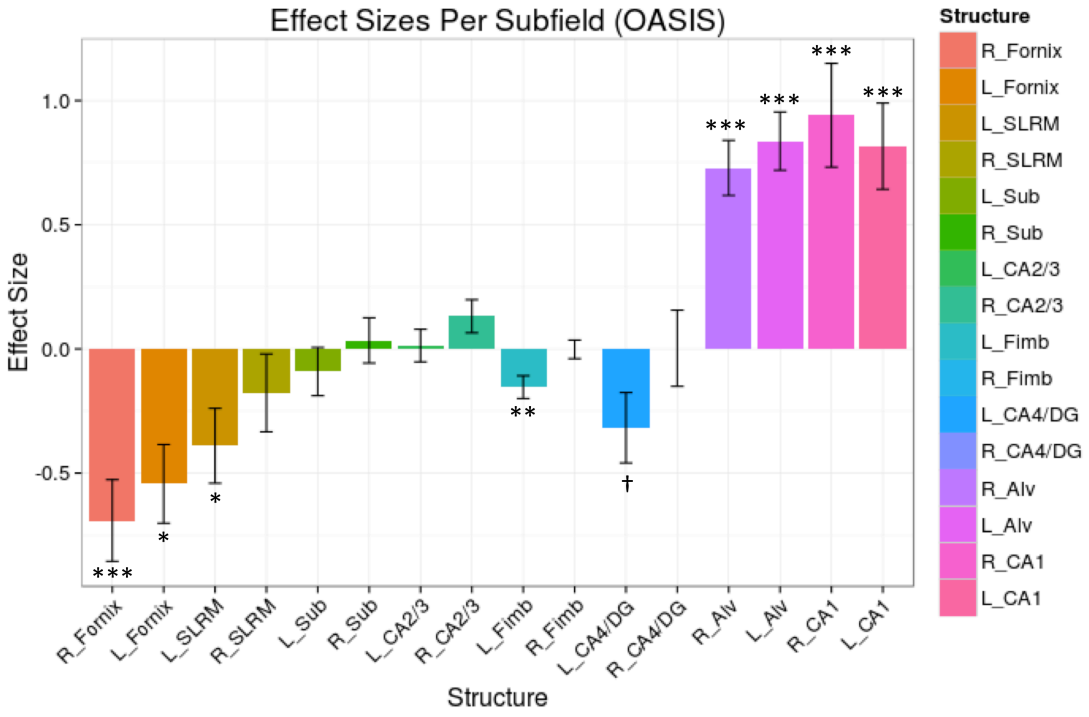

Figure 7. Graph depicting effect size (ß values) of age on structure volumes. A general linear model accounting for sex, and total intercranial volume, demonstrated significant volumetric differences across age (post-Bonferroni correction) for the right and left fornix, right and left alveus, left fimbria, right and left CA1 region as well as the left SR/SL/SM. The left CA4/DG was found to be significant prior to Bonferroni correction. *p<.05, **p<0.01, ***p<0.001, † indicates significance prior to Bonferroni correction.

A correlation matrix of the left and right volumes separately revealed generally positive correlations (Figure 8, A & B) with similar patterns across left and right hemispheres (p<0.001 for all r-values reported here). Namely the left CA1 region was significantly correlated to the left CA2/3 (r = 0.38), CA4/DG (r = 0.64) and SR/SL/SM (r = 0.74) regions. This observed positive correlation was also observed for the right CA1 with CA2/3 (r = 0.58), CA4/DG (r = 0.67) and SR/SL/SM (r = 0.82). In addition, the left alveus was positively correlated to the left

CA1 (r = 0.54), CA2/3 (r = 0.70) and SR/SL/SM (r = 0.43). Similar positive correlations were also observed for the right alveus with the right CA1 (r = 0.75), CA2/3 (r = 0.70) and SR/SL/SM (r = 0.65). A bilateral correlation (Figure 8 C) revealed positive inter-hemispheric cross-correlations between the right alveus and left CA1 region (r = 0.59) as well as the left alveus and right CA1 (r = 0.52). Positive correlations were also observed between the right CA1 and left SR/SL/SM (r = 0.67) as well as the left CA1 and right SR/SL/SM (r = 0.65).

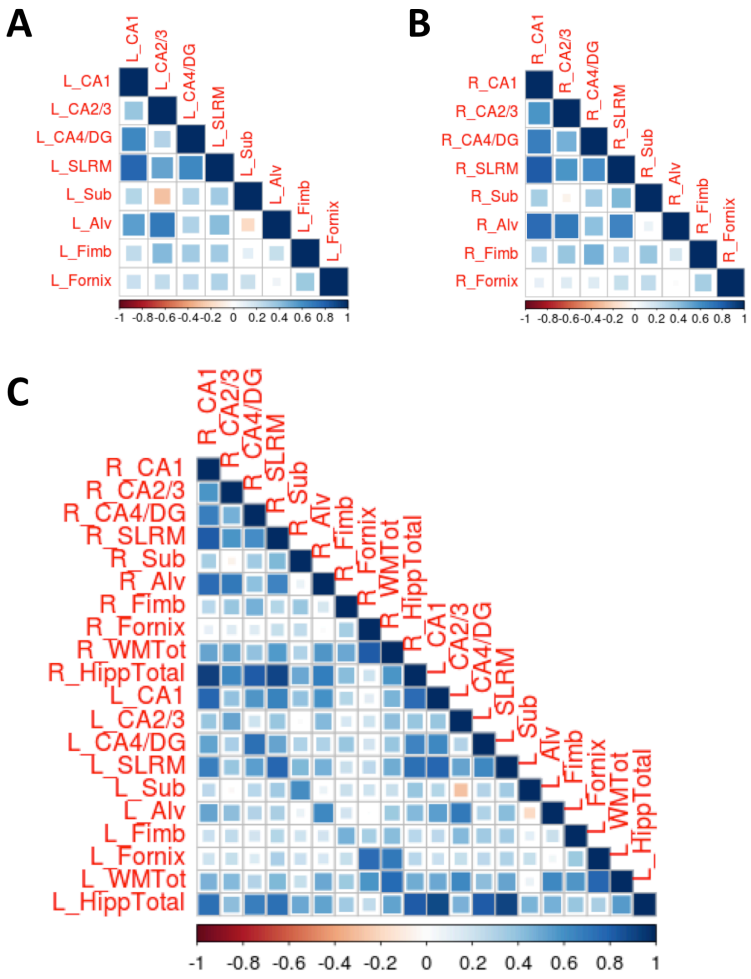

Figure 8. Structural correlation matrices of subfield volumes. A: Structural correlation matrix of left hemisphere subfields. Correlations were bootstrapped 1000 times. B: Structural correlation matrix of right hemisphere subfield volumes. Correlations were bootstrapped 1000 times. C: Structural correlation matrix of all subfield volumes bilaterally. Scale depicts degree of correlation (Pearson r value).

4.5 ADNI Dataset

In contrast to the OASIS results, a significant difference in combined WM volumes (i.e. alveus fimbria and fornix) were observed between the control and MCI group (Left: R^2=0.036, p=0.0073; Right: R^2=0.032, p=0.016; see Figure 9 B). A significant difference was also observed for HF whole volume between control and the MCI cohort (Left: R^2=0.11, p<0.001; Right: R^2=0.060, p<0.001; see Figure 9 A). Contrary to results observed in the healthy aging cohort, the bilateral alveus did not show any significant differences between control and MCI groups (Left: p=0.90; Right: p=0.33; Figure 10 A). The left and right fimbria were found to decrease bilaterally (Left: R^2=0.12, p<0.001; Right: R^2=0.068, p=0.003; Figure 10. B), as did the fornix (Left: R^2=0.051, p=0.0043; Right: R^2=0.093, p<0.001; Figure 10 C) when comparing controls to MCI.

Between the MCI and AD cohorts no significant effect of diagnosis was found for all WM regions combined (see Figure 9 A). Trend-level differences were observed with respect to whole-HF volume differences (Left: R^2=0.013, p=0.079; Right: R^2=0.008, p=0.13; see Figure 9 B). Volumes of all WM subregions were not significantly different between MCI and AD except for the left fimbria, which was found to be significantly decreased in AD compared to MCI (R^2=0.039, p=0.029).

Comparison between the control and AD groups yielded results that were strikingly similar to the control and MCI comparisons. AD demonstrated overall smaller combined WM volumes (Left: R^2=0.089, p<0.001; Right: R^2=0.042, p=0.018; see Figure 9 A), as well as the combined HF volume (Left: R^2=0.27, p<0.001; Right: R^2=0.18, p<0.001; see Figure 9 B). Unlike results for the normative aging sample, significant differences in alveus volume were not observed when comparing controls to the AD group. However, bilateral volume decreases were observed for both the fimbria (Left: R^2=0.38, p<0.001; Right: R^2=0.12, p=0.001), and fornix (Left: R^2=0.068, p=0.0063; Right: R^2=0.10, p<0.001). All above linear models were re-run using BEaST volumes as in the OASIS dataset and showed similar results (see Appendix D for results).

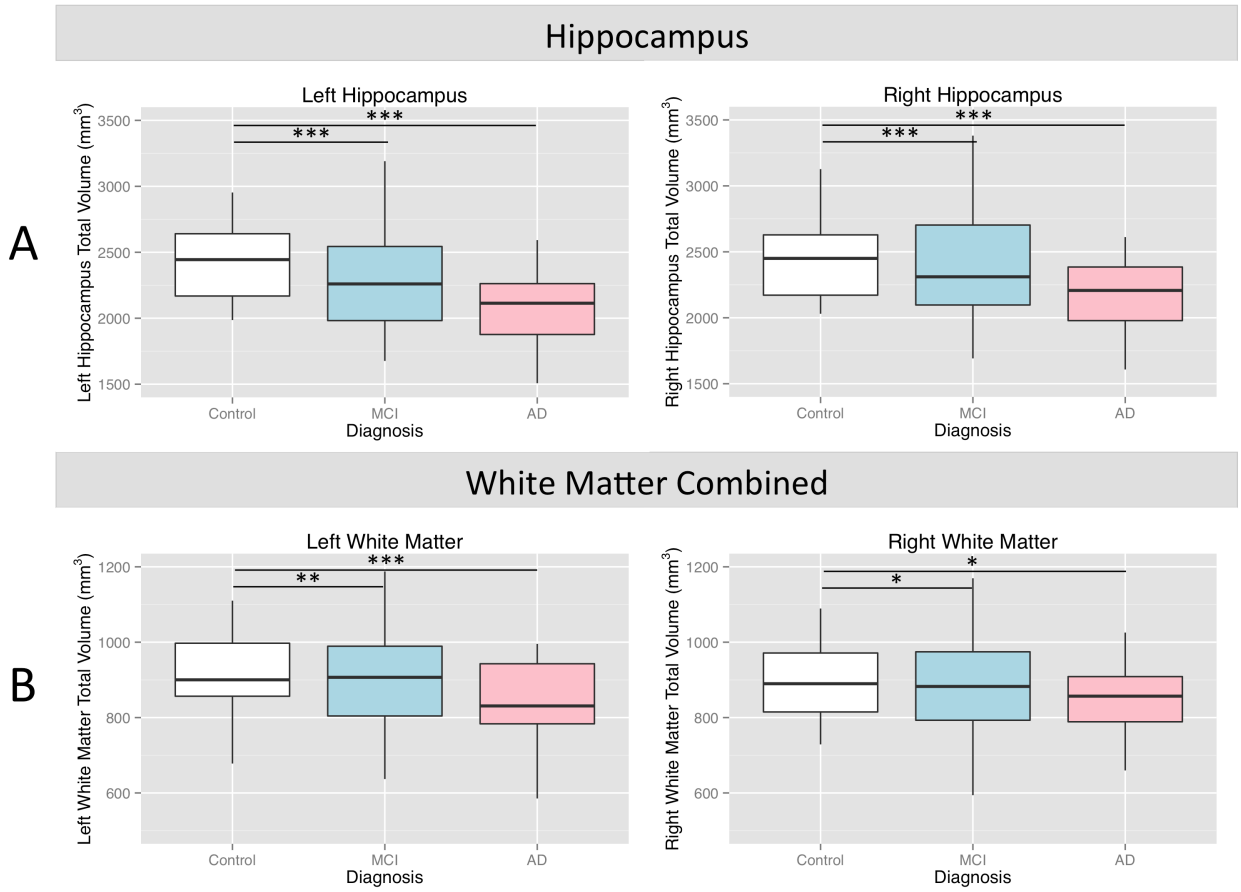

Figure 9. Boxplots of combined hippocampal subfield and white matter volumes for ADNI sample. A: Boxplot of whole hippocampal volume. Whole hippocampal measurement was obtained via the addition of all hippocampal subfield volumes (CA1, CA2/3, CA4/DG, Subiculum and SR/SL/SM). General linear model (GLM) accounting for age, sex and estimated total intracranial volume (eTIV) demonstrated bilateral volume decreases in the hippocampus when comparing the control cohort to the MCI group (Left: R^2=0.11, p<0.001; Right: R^2=0.06, p<0.001), and the Control to AD cohort (Left: R^2=0.27, p<0.001; Right: R^2=0.18, p<0.001). B: Boxplot of combined white matter volume. Combined white matter volume was obtained by the addition of all white matter subfield volumes (alveus, fimbria, and fornix). A GLM accounting for age, sex and eTIV demonstrated a significant decrease when comparing Controls to the MCI group (Left: R^2=0.036, p=0.0073; Right: R^2=0.032, p=0.016), and Control to the AD group (Left: R^2=0.089, p<0.001; Right: R^2=0.042, p=0.018). *= p<0.05, **= p<0.01, ***=p<0.001.

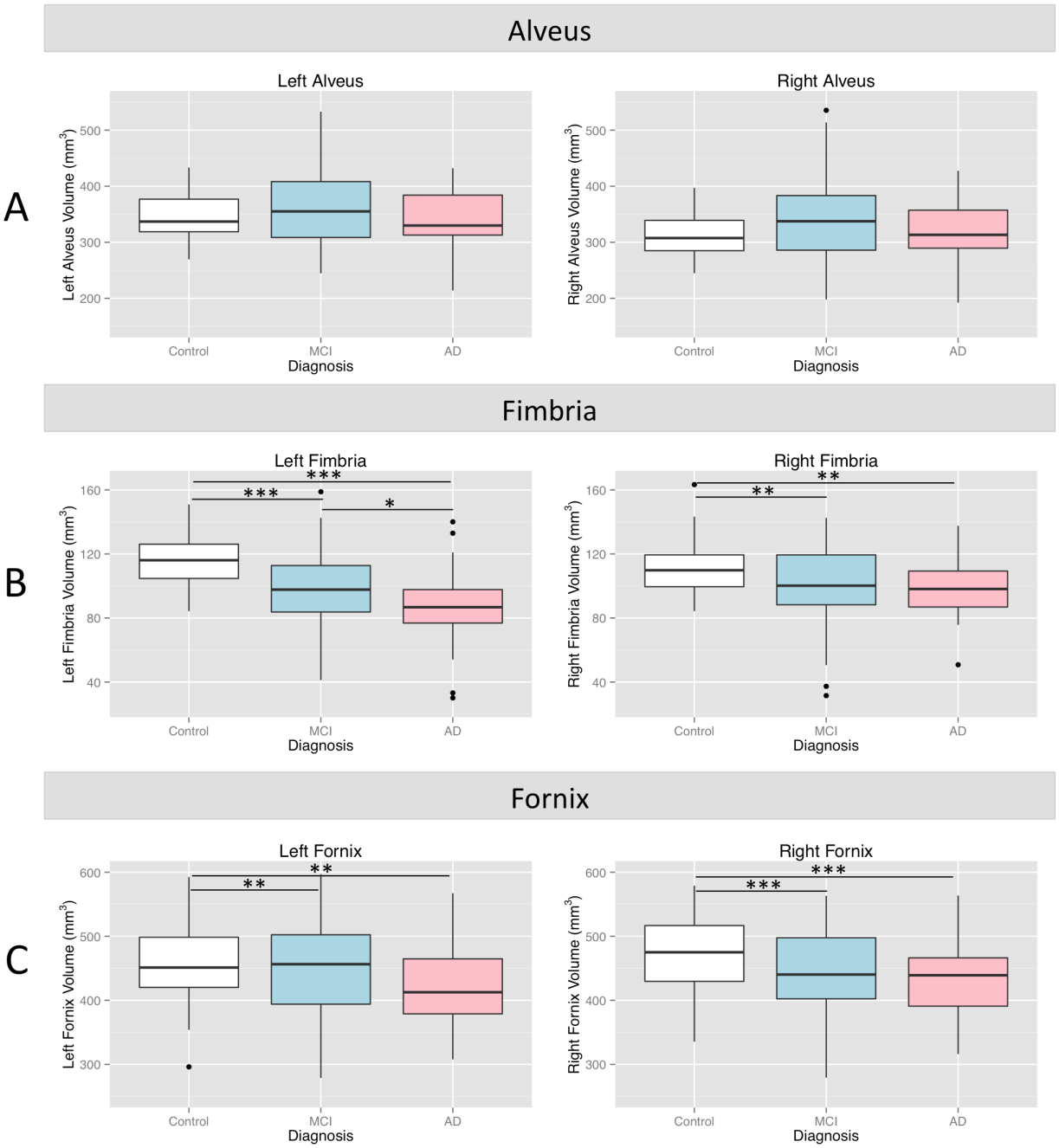

Figure 10. Boxplots of white matter subfield volumes for ADNI sample. A: Boxplots depicting left and right alveus volume by group. A general linear model (GLM) accounting for age, sex and estimated total intracranial volume (eTIV) demonstrated no significant differences comparing across all cohorts. B: Boxplots depicting left and right fimbria volume by group. A GLM accounting for age, sex and eTIV demonstrated a bilateral decrease in fimbria volume when comparing controls to the MCI cohort (Left: R^2=0.11, p<0.001; Right: R^2=0.068, p=0.003). The left fimbria was found to have a significant decrease (R^2=0.039, p=0.029) when comparing volumes of the MCI cohort to those of the AD group. Finally volumes for the bilateral fimbria significantly decreased when comparing controls to the AD cohort (Left: R^2=0.38, p<0.001; Right: R^2=0.12, p=0.001). C: Boxplots depicting left and right fornix volume by group. A GLM accounting for age, sex and eTIV demonstrated a bilateral decrease in fornix volume when comparing controls to the MCI cohort (Left: R^2=0.051, p=0.0043; Right: R^2=0.093, p<0.001). Comparing controls to the AD group, a significant decrease in the left and right fornix was also found (respectively, R^2=0.068, p=0.0063; R^2=0.102, p<0.001). *= p<0.05, **= p<0.01, ***=p<0.001.

In direct contrast to the OASIS results, comparing controls to the MCI cohort (Figure 11 A), demonstrated significant decreases in left and right CA1 (respectively ß =-61.1 and ß =-85.0) and also more striking decreases in the left and right subiculum (respectively ß =-43.2 and ß =-42.8), left and right SR/SL/SM (respectively ß =-67.7 and ß =-46.5), left fimbria (ß =-18.3), and right fornix (ß =-44.6). The left and right CA4/DG regions (respectively ß =-52.3 and ß =-43.2) as well as the right fimbria (ß =-12.7) and left fornix (ß =-34.2) were significant prior to Bonferroni correction. When comparing controls to the AD cohort, significant effect sizes were observed for the left and right CA1 (respectively ß =-114.0 and ß =-88.7), left and right CA4/DG (respectively ß =-74.3 and ß =-71.8), left and right subiculum (respectively ß =-67.9 and ß =-62.1), left and right SR/SL/SM (respectively ß =-87.3 and ß =-67.3), left and right fimbria (respectively ß =-29.9 and ß =-13.8), and right fornix (ß =-42.5). The left fornix (ß =-37.6) was significant prior to Bonferroni correction. Lastly, the MCI versus AD group effect sizes (Figure 11 C) showed no significant effect sizes, although, the left and right subiculum (respectively ß =-26.9 and ß =-21.7), as well as the left fimbria (ß =-11.8) were significant prior to Bonferroni correction.

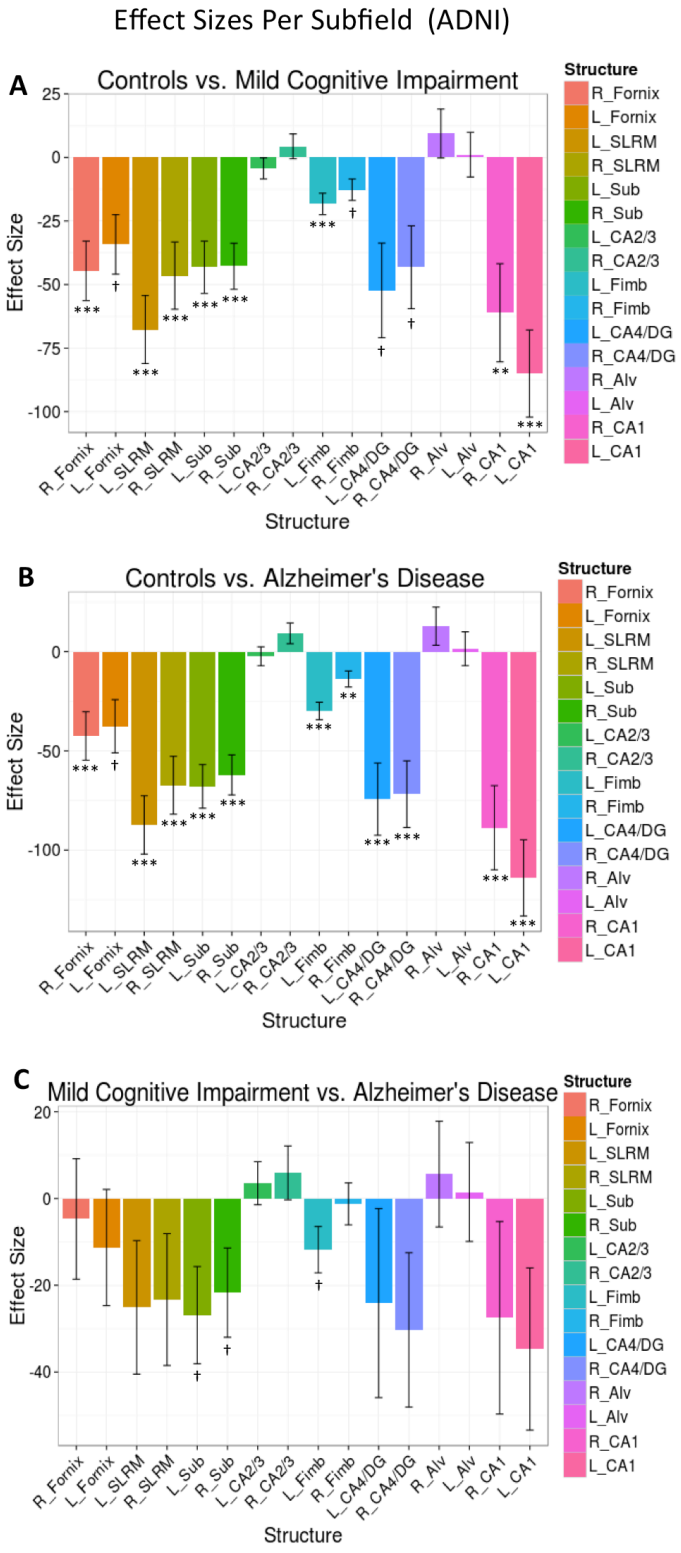

Figure 11. Graph depicting effect size (ß values) of group status on structure volumes in ADNI sample. A general linear model (GLM) accounting for sex, and total intercranial volume was used to assess changes in volumes across all groups (post-Bonferroni correction). A: Effect sizes for controls versus MCI. Significant effect sizes were noted

for the right and left CA1, right and left subiculum, right and left SR/SL/SM, left fimbria and right fornix. The left and right CA4/DG, right fimbria, and left fornix were also found to be significant prior to Bonferroni correction. B: Effect sizes for controls versus AD. Significant effect sizes were noted for the right and left CA1, right and left CA4/DG, right and left subiculum, right and left SR/SL/SM, right and left fimbria and the right fornix. The left fornix was found to be significant prior to Bonferroni correction. C: Effect sizes for MCI versus AD. No significant effect sizes were noted for all subregions. The right and left subiculum, and left fimbria were found to be significant prior to Bonferroni correction. *p<.05, **p<0.01, ***p<0.001, † indicates significance prior to Bonferroni correction.

Chapter 5. Discussion

The present thesis presents a complete and comprehensive investigation of WM volumetry with respect to normal and pathological aging. This was accomplished via the creation, validation, and implementation of a novel methodological approach to the *in vivo* investigation of human extra-hippocampal WM. First, a detailed high-resolution segmentation protocol for the delineation of all WM outputs of the HF (i.e. alveus, fimbria and fornix) was developed and was found to be both reliable and reproducible; importantly the developed protocol is complementary to existing work on the HF subfields by our group (Winterburn et al., 2013). Secondly, the feasibility of using these manual segmentations as atlases for the automatic segmentation of HF subfields and WM by way of MAGeT-Brain segmentation was assessed and validated. Validation efforts demonstrated both appropriate precision and accuracy of MAGeT-Brain output segmentations at 1mm isotropic voxel dimensions. Finally, the volumetry of the WM structures in healthy and pathological aging was assessed by performing MAGeT-Brain segmentation on two different datasets, namely, the OASIS dataset (a healthy aging cohort) and the ADNI-1 3T baseline dataset (cohorts of controls, MCI, and AD). Results indicated a preservation of the bilateral alveus and CA1 region over the course of healthy aging. Significant decreases were also noted for the bilateral fornix, left fimbria, and left SR/SL/SM regions. With respect to pathological aging, comparison of the MCI cohort to controls indicated decreases in bilateral CA1, subiculum, SR/SL/SM, left fimbria and right fornix. While comparison of MCI to AD cohorts did not reveal any significant differences, the results observed for comparison of controls to AD remained markedly similar to those observed for MCI to controls with decreases observed in the bilateral CA1, CA4/DG, subiculum, SR/SL/SM, fimbria, and right fornix.

Manual segmentation has been a dominant approach for the study of HF subfields *in vivo*. Many protocols exist for the segmentation of the HF subfields (e.g. Adler et al., 2014; Bender et al., 2013; Duncan et al., 2014; Ekstrom et al., 2009; Kerchner et al., 2012; La Joie et al., 2010; Malykhin et al., 2010; Mueller & Weiner, 2009; Olsen et al., 2013; Palombo et al., 2013; Preston et al., 2010; L. Wang et al., 2003; Winterburn et al., 2013; Wisse et al., 2012; Yushkevich, Pluta, et al., 2015b; Zeineh et al., 2012; Zeineh, Engel, Thompson, & Bookheimer, 2001) including recent work towards the development of a unified protocol (Yushkevich, Amaral, et al., 2015a). Despite the many available options for manual segmentation of the HF, the use of (Winterburn et

al., 2013) for manual segmentation maintains significant advantages. Firstly, the present tracing protocol segments HF subfields along the entire anterior to posterior axis of the HF while other groups instead include separate labels for head and tail regions (Olsen et al., 2013; Palombo et al., 2013; Preston et al., 2010; L. Wang et al., 2003; Zeineh et al., 2001). In fact, some protocols are devoid completely of segmenting the head and tail and restrict segmentation of HF subfields to solely the body (Bender et al., 2013; Kerchner et al., 2012; Mueller et al., 2007). Secondly, the protocol employed maintains improved inclusivity with respect to regions segmented. For example, Palombo et al. (2013) include only three ROIs: the subiculum, CA1, and CA2/CA3/CA4/DG (grouped together); this same ROI assortment and grouping is consistent across multiple segmentation protocols (Duncan et al., 2014; La Joie et al., 2010; Preston et al., 2010; Zeineh et al., 2001). As opposed to segmentation of 3 ROI regions, the Winterburn et al. (2013) protocol delineates 5 different ROIs (subiculum, CA1, CA2/CA3, CA4/DG, SL/SR/SM), and is the only method at 3T that can successfully isolate the molecular layers (i.e. SL/SR/SM). These characteristics of the Winterburn et al. (2013) protocol allow for the precise investigation of HF subfields at an unprecedented level of anatomical rigor.

Novel post mortem work has led to the capability of segmenting 6 separate ROIs (i.e. subiculum, CA1, CA2, CA3, CA4/DG, and SL/SR/SM; Adler et al., 2014) via histology-derived volumetric annotation of the HF. This process involves reconstructing sequential histological sections to the MRI scan of the same post mortem brain in order to obtain exact microscopic-based HF subfield delineations. While the product achieved by this type of work is desirable, the effort required and lack of applicability of the final product may hinder its use in novel research studies. A time-intensive and computationally expensive process, the histological-reconstruction and registration to an MRI scan preformed here was completed for an 89-year-old female. This severely limits subject variation in the finalized segmentation and makes results of this work difficult to apply to other cohorts. Moreover, since delineations are solely based on the histology of one subject, no specific set of rules can be applied manually to other cases and establishes this work as more of a proof-of-concept study. However, future work in this field holds promise. If histologically reconstructed MRI delineations can be completed on numerous subjects of a representative population, they may be useful atlases for incorporation into an automatic segmentation framework.

In addition to the above limitations observed in the segmentation protocols themselves, efficacy and quality of manual tracings also depend on field-strength, resolution, and scanning parameters used for acquisition. For example, many *in vivo* scanning protocols use highly anisotropic voxel dimensions in the coronal plane with low-resolution through the anterior-posterior direction (2-3 mm; Kerchner et al., 2010; La Joie et al., 2010; Mueller et al., 2007; Mueller & Weiner, 2009; Olsen et al., 2013; Palombo et al., 2013; Van Leemput et al., 2009). While these types of acquisitions are advantageous since they reduce acquisition times, they introduce significant sampling bias in the measurement of small and geometrically complex structures and partial volume effects, possibly altering the visualization of clear boundaries. Despite the inherent trade-off with respect to scan-time, the scanning parameters employed in the present thesis address these concerns by using images with anisotropic voxels. Although this trade-off is not explicitly quantified (which would be difficult to complete in the absence of data from other groups), it is likely that systematic introduction of noise in images with anisotropic voxels can be more easily overcome with increases in sample size. Therefore the use of anisotropic data can limit partial volumes and increase accuracy of manual segmentations completed for the HF subfields and associated WM regions. In addition, some groups argue for more precise measures by completing segmentation of HF subfields at 7T (Kerchner et al., 2012; Kirwan et al., 2007; Malykhin et al., 2010; Wisse et al., 2012; Zeineh et al., 2012). While signal-to-noise and image-contrast ratios may be improved and results in images with an increased level of detail, most MR research is conducted using 3T scanners. Not only are the costs of 7T scanners high, but their absence in clinical settings may also hamper data availability and corresponding study investigation (Balchandani & Naidich, 2015).

The similar limitations observed for the HF subfields with respect to segmentation protocols and scanning acquisition also hold true for the volumetric investigation of the WM regions of the alveus, fimbria, and fornix. As a whole, little work has focused on the WM of the HF, let alone its segmentation and volumetry. Our work improves on previously published protocols for the segmentation of the fornix (Bilir et al., 1998; Copenhaver et al., 2006; Gale et al., 1995; Kuzniecky et al., 1999; Zahajszky et al., 2001) that carry specific limitations. Namely, these include: the lack of full anterior to posterior segmentation, grouping of multiple structures within

the same ROI, and exclusion of entire structures altogether. For example, all above-mentioned WM protocols fail to segment posterior and/or anterior areas of the fornix. Of those that claim to include posterior and anterior-most regions (Copenhaver et al., 2006; Zahajszky et al., 2001), segmentation terminates at the level of the anterior commissure, thereby omitting the anterior pillars of the fornices. Grouping of structures is also observed amongst all protocols as only one ROI is created for the fornices, and volumetric measures are a bilateral sum of the right and left fornix. The current protocol circumvents both these issues and is not only capable delineating the left fornix from the right, but also includes the entire anterior to posterior extent of the fornix. Additionally, the above protocols exclude the fimbria and fornix entirely. Although a few protocols exist for the segmentation of the alveus and fimbria, these either group both regions together into the same ROI (Wang et al., 2003; Zeineh et al., 2012) or lack clear anatomical details for their separate delineation (Parekh et al., 2015). In addition, the majority of protocols have completed segmentation at more standard imaging resolutions, often employing 1.5T isotopic (e.g. Zahajszky et al., 2001) or anisotropic voxel sizes (1mm x 1mm x 1.5mm; e.g. Copenhaver et al., 2006). The only protocol that includes sub millimeter voxel sizes is Parekh et al. (2015; 0.4mm isotropic) but employs high-field 7T imaging in order to do so while also combining the fimbria and fornix within the same ROI. To the best of our knowledge, this work is the first to develop a detailed 3T protocol for the full anterior to posterior segmentation of the alveus, fimbria, and fornix.

Establishing inter- and intra-rater reliability is key to the development of a useful segmentation protocol. Not only does this secure the reproducibility of the protocol by the protocol author (intra-rater reliability), it also establishes the reproducibility of the protocol by others based on the protocol outline (inter-rater reliability). In Table 1 we show strong inter- and intra-rater reliabilities with Dice's Kappa values ranging from 0.81-0.90 for the alveus, fimbria, and fornix. Direct comparison of our results to those of past protocols is difficult for a number of reasons. Firstly, of the protocols segmenting the alveus, fimbria, and fornix, none include any measures of reliability (Parekh et al., 2015; Wang et al., 2003; Zeineh et al., 2012). In addition, past protocols for the segmentation of the fornix use ICC as a method of reliability evaluation. While ICC is capable of discerning the degree of correlation to which two volumes are associated with each other, it does not maintain the capability of evaluating the spatial or anatomical similarity

between them. For example, two ROIs with exactly the same volume can be compared and may receive a high ICC. However, if these volumes were in completely different spatial locations, then observed ICC values would not change. Since the essence of segmentation lies in proper boundary placement, a more suitable and frequently used measure is Dice's Kappa overlap metric (Dice, 1945). Used excessively in recent HF subfield segmentation literature (Olsen et al., 2013; Palombo et al., 2013; Winterburn et al., 2013; Yushkevich, Pluta, et al., 2015b) and herein, this method penalizes raters for segmentations that fall outside the boundaries of the original ROI. Nonetheless, the ICC values reported by other groups are moderately high (see Table 3), ranging from 0.88-0.97. Taking into consideration that these results were obtained at standard image resolutions, the reliability of the present high-resolution segmentation protocol is high, especially given the increased margin of error incurred with increased voxel resolution and number.

Table 3. Comparison of WM Reliability Across Protocols

Author	**Intra-Rater Reliability**	**Inter-Rater Reliability**	**Method of Evaluation**
Amaral et al., 2016	0.81-0.90	0.81-0.87	Dice's Kappa
Bilir et al., 1998*	2.9-3.5%	0.86-0.98	Coefficient of variation percentage / ICC
Copenhaver et al., 2006*	0.93	0.97	ICC
Gale et al., 1995*	0.92	0.92	ICC
Kuzniecky et al., 1999*	3.5%	0.82	Coefficient of variation percentage / ICC
Parekh et al., 2015	none	none	none
Wang et al., 2003	none	none	none
Zahajszky et al., 2001*	0.91	0.83	ICC
Zeineh et al., 2012	none	none	none

Reliability values listed are those reported in respective articles. Ranges are reported for some protocols. Listed ranges for Amaral et al., (2016) is based on average WM reliability across all regions (i.e. not limited to the fornix).
* denotes segmentation of only fornix.

It can be argued that volume is not considered a primary metric for the MR investigation of white matter tracts. By contrast, it can be thought that a better estimate of white matter integrity can be completed using diffusion-weighted imaging (DWI). This is reflected in literature where volumetric investigation of the WM structures of the memory circuit has received significantly less attention. Instead, the majority of studies focus on DWI measures. While DWI is capable of

successfully imaging WM tracts, standard DWI measures do not maintain the level of spatial detail needed to capture the alveus, fimbria, and areas of the anterior-most fornix. Although tailored high-resolution DWI sequences can increase fiber-tracking results, these protocols take more time to employ and are highly specific. This makes subsequent analyses more laborious to complete (Yassa et al., 2010; Zeineh et al., 2012). In addition, given their proximity to the lateral ventricles, standard DWI measures of these WM projections may suffer from partial volume effects, free water contamination, and inherent spatial, as well as angular resolution constraints, all of which limit its application to only the fornix (Pelletier et al., 2013; Zhuang et al., 2013). Different pulse sequences (e.g. FLAIR) have also been used to eliminate the CSF partial volume effects, however, this often comes at a cost of lowering signal-to-noise ratio and consequently downgrades fiber tracking results (Basser & Pajevic, 2000; Chou et al., 2005; Jones, 2003). Therefore, volumetry of these regions may be a useful proxy of WM integrity and, potentially, a complementary analysis metric. As advancements in high-resolution DWI continue, future work should look to establish and quantify the homology between these two metrics. This may identify if easily obtained volumetric data (as such from automatic segmentation pipelines) can be practically used as a primary metric. This is especially important for in-clinic use. Results permitting, if viable WM biomarkers for disease onset or progression are discovered, a method capable of providing quick and efficient patient evaluation would be an asset, and therefore more practical as opposed to a detailed and laborious high-resolution DWI sequence.

Advancements with respect to the automatic segmentation of HF subfields have been made over recent years (Fischl, 2012; Iglesias et al., 2015; Pipitone et al., 2014; Van Leemput et al., 2009; Yushkevich, Pluta, et al., 2015b). Despite the use of high-resolution images as inputs by some algorithms (e.g. Yushkevich, Pluta, et al., 2015b), these images still suffer the same resolution constraints as mentioned previously. In addition, availability of such datasets are rare and the majority of large MR datasets complete scanning at more standard resolutions. In fact, the majority of automatic HF subfield segmentation has been completed on standard 1mm isotropic images (Fischl, 2012; Iglesias et al., 2015; Pipitone et al., 2014; Van Leemput et al., 2009; Voineskos et al., 2015). It can be argued that the dependability of using an automatic segmentation method on such data may result in imprecise measurements. Since the MAGeT-

Brain algorithm uses a combination of whole HF anatomy and local contrast features (both of which are visible despite speculation in standard T1-weighted images), accurate and precise measurements should be possible. Our validation efforts were therefore motivated not only by this, but also due to the absence of any validation effort made on behalf of the aforementioned algorithms for segmentation of HF subfields on standard MR images (apart from Pipitone et al., 2014 by our group). We demonstrated high accuracy as measured by ICC in our first of three validations. The high ICCs supported the reproducibility of MAGeT-Brain segmentation for all structures. Our corresponding two additional tests for precision revealed lower but appropriate numbers. The Kappa values obtained following the transformation of OASIS labels into the same space represent a lower bound of reliability given the inherent error attributed with image registration. LOOCV results were similar to those previously reported by our group (Pipitone et al., 2014). Compared to other validation reports, our Dice's Kappa values were slightly lower than those reported in Yushkevich et al. (2009; Dice range of 0.51-0.74) and Yushkevich, Pluta, et al. (2015b; Control HF subfields Dice range of 0.50-0.82). However, it is important to differentiate between the two validations as they were obtained through validation directly on high-resolution images, and did not contain WM regions. In addition, the LOOCV included in (Yushkevich, Pluta, et al., 2015b) and (Yushkevich et al., 2009) included the comparison of manual segmentations directly to automatic results of the same image since atlases and subject images were of the same resolution. The present LOOCV completed is limited by our segmentation protocol, which cannot be used to manually delineate HF subfields and WM directly on 1mm isotropic data. Although not ideal, the down-sampling atlases (and corresponding labels) was required to complete an approximate validation. As described in (Pipitone et al., 2014), the resampling during this LOOCV combined with the use of only three atlases may have contributed to lower overlap scores (as we have previously demonstrated). The observed lower values for WM subregions were expected, yet are still impressive given that these structures are often 1-2 voxels thick and are spatially dynamic (i.e. twist, turn and move in and out of all planes). Further, the Dice metric penalizes structures with high surface area-to-volume ratios; precisely the type of geometry shown in the HF WM structures. To our knowledge, this is the first attempt at validation, let alone automatic segmentation, of the HF subfields and alveus, fimbria, and fornix on T1 1mm3 standard MRI images.

The use of 1mm isotropic data remains a limitation of the present study, with a trade-off made for image quantity over quality. Future work still lies in adapting and validating MAGeT-Brain segmentation for the automatic segmentation of high-resolution images. With respect to standard image segmentation, a few additional improvements can be made in future MAGeT-Brain work. For example, it is well known that automatic multi-atlas segmentation techniques require atlases representative of their population in order to achieve the best possible results (Cabezas et al., 2011; Dill et al., 2015). One limitation of the current implementation of MAGeT-Brain involves the demographic details of the high-resolution atlases used. Specifically, atlases consisted of 2 males and 3 females aged 29-57 (av. = 37). While such an atlas set may be representative for a healthy aging population, they may not be the most appropriate for the segmentation of AD or MCI cohorts. Having an additional representative set of high-resolution HF/WM atlases for AD and/or MCI patients may provide more accurate results. Although the inherent problem of comparison between results generated from two different atlases sets would remain, the unique structure of MAGeT-Brain attempts to somewhat circumvent this issue via the use of templates. By having a subset of the subjects chosen as templates, final segmentations are ultimately based off a representative set of subjects as opposed to directly from the atlases. In this way, the bias associated with using healthy atlases to segment AD cohorts is reduced. Despite difficulties associated with creating a gold-standard atlas set of atrophic AD or MCI brains, this would also be advantageous for further validation. Currently, the validations included herein are only applicable to the OASIS cohort. By having a high-resolution atlas set, the same LOOCV can be preformed for AD or MCI populations.

Compared to the study of AD and MCI, the investigation of HF subfields and WM with respect to healthy aging has been relatively limited. Consistent with previous findings from our group (Voineskos et al., 2015), no significant relationship with whole HF volume and age were observed, however, the present study identified a strong preservation of the CA1. To date, few studies seem to support this result (La Joie et al., 2010; Voineskos et al., 2015). However, numerous studies have demonstrated an opposite and linear decrease in CA1 volume throughout age (Mueller et al., 2007; Mueller & Weiner, 2009; Raz et al., 2015; Shing et al., 2011; Wisse et al., 2014). Unlike the present study, these studies involve MR images at sub-millimeter voxel sizes. Consequently, significantly lower participant numbers are used compared to the present

study (see Table 4 for comparison). Nonetheless, other studies have used semi-automated methods (Kerchner et al., 2013) to show linear decreases in CA1 volume, while a recent automated investigation revealed no effect throughout age (Pereira et al., 2014). It has also been demonstrated that CA1 volume decline begins around the age of 50 in a nonlinear trajectory (de Flores et al., 2015). Some studies have also shown similar results to those presented in this study regarding null changes in CA4/DG volume (de Flores et al., 2015; Kerchner et al., 2013; Mueller et al., 2007; Raz et al., 2015; Shing et al., 2011), yet a few studies support decreases with age (de Flores et al., 2015; Mueller & Weiner, 2009; Pereira et al., 2014; Wisse et al., 2014; see Table 4 for overview of studies investigating HF subfield structure in healthy aging). Heterogeneity in these results across laboratories may be a result of different methods used for segmentation, differing definitions of the subfields themselves, and/or differing use of covariates. For example, studies that use the Mueller protocol (Mueller et al., 2007) may suffer from a substantial bias, as this protocol only requires the demarcation of three coronal slices in the body of the HF. Further, other studies may or may not use brain volume as a covariate in their results.

Table 4. Comparison of WM and HF Subfield Volumetry Across Healthy Aging Studies

Author	**Field Strength / Voxel Resolution (mm)**	**Segmentation Type / Subject Number**	**Labeled ROIs**	**Volumetric Results**
Amaral et al., 2016	3T / 1.0 x 1.0 x 1.0	Automatic /315	CA1, CA2/CA3, CA4/DG, SL/SR/SM, Subiculum, alveus, fimbria, fornix	Increase: alveus, CA1 Decrease: left SL/SR/SM, fornix, left fimbria
Frisoni, Ganzola, Canu, Rüb, Pizzini, Alessandrini, Zoccatelli, Beltramello, Caltagirone, & Thompson, 2008a	3T / 1.0 x 1.0 x 1.0	Manual /19	HF, DG, subiculum, alveus/fimbria	Increase: HF
Kerchner et al., 2013	7T / 0.22 x 0.22 x 1.5	Semi-Automatic / 27	CA1/SL/SR/SM, CA1/SP, CA3/DG	Decrease: CA1/SR/SL/SM

La Joie et al., 2010	3T / 0.38 x 0.38 x 2.0	Manual /50	CA1, CA2/CA3/CA4/ DG, subiculum	Decrease: subiculum
Mueller et al., 2007	4T / 0.4 x 0.5 x 2.0	Manual /42	CA1, CA2, CA3/CA4/DG, subiculum	Decrease: CA1
Mueller & Weiner, 2009	4T / 0.4 x 0.4 x 2.0	Manual /119	CA1, CA1-2 transition, CA3/DG	Decrease: CA1, CA3/DG
Pereira et al., 2014	3T / 1.0 x 1.0 x 1.0	Automatic /50	CA1, CA2/CA3, CA4/DG, subiculum, presubiculum, fimbria	Decrease: CA2/CA3, CA4/DG
Raz et al., 2015	3T, 0.4 x 0.4 x 2.0	Manual /80	CA1/CA2, CA3/DG, subiculum	Decrease: CA1/CA2
Shing et al., 2011	3T / 0.4 x 0.4 x 2.1	Manual /29	CA1/CA2, CA3/CA4/DG, subiculum	Decrease: CA1/CA2
Voineskos et al., 2015	1.5T / 0.78 x 0.78 x 1.5	Automatic /137	CA1, CA2/CA3, CA4/DG, SL/SR/SM, subiculum	Decrease: CA2/CA3, CA4/DG, SL/SR/SM, subiculum
Wisse et al., 2014	7T / 0.7 x 0.7 x 0.7	Manual /29	CA1, CA2, CA3, CA4/DG, subiculum	Decrease: CA1, CA4/DG

No study to date has investigated changes in WM regions within the memory circuit. Thus, our results demonstrating preservation of the bilateral alveus and decreases in the left fimbria and fornices with age are the first to our knowledge. While some volumetric studies investigating the fimbria have shown no change in volume across age (Frisoni, Ganzola, Canu, Rüb, Pizzini, Alessandrini, Zoccatelli, Beltramello, Caltagirone, & Thompson, 2008a; Pereira et al., 2014) the fornix has been extensively studied via DWI. Studies using quantitative fiber tracking corroborate our results by showing age-dependent reductions in fornicial structure (Schmahmann et al., 2007; Zahr et al., 2009), along with more recent DWI studies (Fletcher et al., 2013; Gunbey et al., 2014; Lebel et al., 2012; Sala et al., 2012; Sasson et al., 2013; Sullivan et al., 2010).

On the other hand, research pertaining to the study of HF subfields within the context of AD and MCI has been reasonably more extensive. Previous high-resolution volumetric studies comparing the HF subfields in AD and control cohorts have replicated our observed findings of simultaneous decreases in subiculum, CA1, CA4/DG and SR/SL/SM volume together (Adachi et al., 2003; Boutet et al., 2014; de Flores et al., 2015; La Joie et al., 2010). Among all volumetric results in AD, observed decreases in the CA1 region occur most frequently and are often the central focus in such studies (Adachi et al., 2003; Boutet et al., 2014; de Flores et al., 2015; Iglesias et al., 2015; Kerchner et al., 2013; Khan et al., 2015; La Joie et al., 2013; Li et al., 2013; Lim et al., 2012; Mueller et al., 2010; Mueller & Weiner, 2009; Wisse et al., 2014; Yassa et al., 2010; Yushkevich, Pluta, et al., 2015b). Studies employing automatic segmentation completed at more standard resolutions akin to the present study have also been completed (Khan et al., 2015; Li et al., 2013; Lim et al., 2013) and have substantiated our results of decreases in the subiculum, CA2/3, CA2/DG and/or CA1. As stated previously, it is important to note that differences in segmentation protocols and atlases may partially explain the varying results among studies. While some fail to show volumetric changes in MCI cohorts (Kerchner et al., 2013; Wisse et al., 2014), a select few point towards focal decreases in CA1 (Mueller et al., 2010; Mueller & Weiner, 2009), CA3/DG, CA4/DG and/or the subicular subfields (de Flores et al., 2015; La Joie et al., 2013; Pluta et al., 2012). Some of the aforementioned automatic segmentation studies also included an MCI component, which resulted in similar results (Hanseeuw et al., 2011; Iglesias et al., 2015; Khan et al., 2015; Lim et al., 2012; Yushkevich, Pluta, et al., 2015b; see Table 5 for overview of studies investigating HF subfield structure in MCI and AD).

Table 5. Comparison of WM and HF Subfield Volumetry Across AD and MCI Studies

Author	**Field Strength / Voxel Resolution (mm)**	**Segmentation Type / Subject Number**	**Labeled ROIs**	**Volumetric Results**
Amaral et al., 2016	3T / 1.0 x 1.0 x 1.0	Automatic /AD: 47 MCI: 69	CA1, CA2/CA3, CA4/DG, SL/SR/SM, Subiculum, alveus, fimbria, fornix	Decrease: CA1, SL/SR/SM, subiculum, fornix, fimbria
Adachi et al., 2003	1.5T / 1.0 x 1.0 x 1.0	Manual / AD: 12	CA1, CA3/CA4, subiculum	Decrease: CA1, CA3/CA4, subiculum

Boutet et al., 2014	7T / 0.30 x 0.30 x 1.2	Manual / AD: 4	CA1-SL/SR/SM, CA1-SP, hilum, subiculum-SP, alveus	Decrease: CA1-SL/SR/SM, CA1-SP, subiculum-SP, alveus
Callen et al., 2001	1.5T / 1.3 x 1.3 x 1.3	Manual /AD: 40	Hippocampus, fornix, mammillary bodies	Decrease: Hippocampus, fornix, mammillary bodies
Copenhaver et al., 2006	1.5T / 1.0 x 1.0 x 1.0	Manual /AD: 16 MCI; 20	Fornix, mammillary bodies	Decrease: Fornix, mammillary bodies
Hanseeuw et al., 2011	3T / 0.81 x 0.95 x 1.0	Automatic /MCI: 15	CA1, CA2/CA3, CA4/DG, presubiculum, subiculum, fimbria	Decrease: CA2/CA3, subiculum
Iglesias et al., 2015	1.5T, 1.0 x 1.0 x 1.0	Automatic /MCI: 16	CA1, CA2/CA3, CA4, GC-DG, molecular layer, presubiculum, subiculum, parasubiculum, alveus, fimbria	Decrease: CA1, CA2/CA3, CA4, GC-DG, molecular layer, fimbria
Kerchner et al., 2010	7T / 0.2 x 0.2 x 2.0	Manual /AD: 14	CA1-SL/SR/SM, CA1-SP	Decrease: CA1-SP
Kerchner et al., 2013	7T / 0.22 x 0.22 x 1.5	Semi-automatic /MCI: 15 AD: 11	CA1-SL/SR/SM, CA1-SP, CA3/DG	Decrease: CA1-SL/SR/SM, CA1-SP, CA3/DG
Khan et al., 2015	1.5T / 1.1 x 1.1 x 1.2	Automatic /MCI: 357 AD: 291	CA1, CA2/CA3, CA4/DG, presubiculum, subiculum, fimbria	Decrease: CA1, CA2/CA3, CA4/DG, presubiculum, subiculum, fimbria
La Joie et al., 2010	3T, 0.375 x 0.375 x 0.375	Manual /MCI: 17 AD: 18	CA1, CA2/CA3/CA4/, subiculum	Decrease: CA1, CA2/CA3/CA4/, subiculum
Li et al., 2013	1.5T / 1.2 x 1.2 x 1.2	Automatic /AD: 29	CA1, CA2/CA3, CA4/DG, presubiculum, subiculum, fimbria	Decrease: CA1, CA2/CA3, CA4/DG, presubiculum, subiculum,

				fimbria
Lim et al., 2013	3T / 1.0 x 1.0 x 1.0	Automatic /AD: 31	CA1, CA2/CA3, CA4/DG, presubiculum, subiculum, fimbria	Decrease: CA2/CA3, CA4/DG, presubiculum, subiculum
Mueller et al., 2010	4T / 0.4 x 0.4 x 2.1	Manual /MCI: 20 AD: 18	CA1, CA1-2 transition, CA3/DG, subiculum	Decrease: CA1, CA1-2 transition, CA3/DG, subiculum
Mueller & Weiner, 2009	4T / 0.4 x 0.4 x 2.0	Manual /MCI: 20 AD: 18	CA1, CA1-2 transition, CA3/DG, subiculum	Decrease: CA1, CA1-2 transition, subiculum
Pluta et al., 2012	3T / 0.4 x 0.4 x 2.0	Semi-automated /MCI: 17	CA1, CA4/DG	Decrease: CA1, CA4/DG
Wisse et al., 2014	3T / 0.7 x 0.7 x 0.7	Manual /MCI: 16 AD: 9	CA1, CA2, CA3, CA4/DG, subiculum	Decrease: CA1, CA3, CA4/DG, subiculum
Yassa et al., 2010	3T / 0.75 x 0.75 x 0.75	Manual /MCI: 10	CA1, CA3/DG, subiculum	Decrease: CA1, CA3/DG
Yushkevich, Pluta, et al., 2015b	3T / 1.0 x 1.0 x 1.0	Automatic /MCI: 40	CA1, CA2/CA3, CA4/DG, presubiculum, subiculum, fimbria	Decrease: CA2/CA3, CA4/DG, presubiculum, subiculum, fimbria

With respect to WM regions, we found significant decreases in only the fornix and fimbria in both AD and MCI. Previous studies have demonstrated the accelerated atrophy of the fornix in AD volumetrically (Callen et al., 2001; Copenhaver et al., 2006) along with a wide range of DWI studies (Jin et al., 2015; Metzler-Baddeley et al., 2012; Oishi et al., 2012; Zhuang et al., 2013). While DWI work also implicates the fornix in MCI (Huang et al., 2012; Mielke et al., 2009; Oishi et al., 2012) the few existing volumetric studies have (Cui et al., 2012), and have not (Copenhaver et al., 2006) shown evidence of decreases in fornicial volume. As for the fimbria, mixed evidence suggests both atrophy and preservation over MCI (Hanseeuw et al., 2011; Iglesias et al., 2015; Khan et al., 2015; Lim et al., 2013; Yushkevich, Pluta, et al., 2015b) and AD (Frisoni, Ganzola, Canu, Rüb, Pizzini, Alessandrini, Zoccatelli, Beltramello, Caltagirone, & Thompson, 2008a; Khan et al., 2015; Li et al., 2013; Lim et al., 2013). While no results were observed for the alveus, decreases in alveus volume have been both reported in AD (Boutet et

al., 2014) and not found in MCI (Iglesias et al., 2015). Surprisingly, we did not observe significant differences for WM regions when comparing AD to MCI (that is, aside from the left fimbria). Although such differences have been reported (Mielke et al., 2009; Oishi et al., 2012) we found increasing negative effect sizes for the fornix and fimbria in aging to MCI and AD. Although not significantly step-wise, these results may support the conclusion that rates of atrophy in WM structures in healthy aging can serve as a predictor of conversion to MCI and AD (Fletcher et al., 2013).

Perhaps the most important goal of this study was to volumetrically assess the memory circuit in its entirety. In this way, each subfield could be evaluated within the context of all other structures, unlike most studies, which simply consider a few subfields irrespective of neighboring structures. This approach is necessary given the inherent connections present within the HF subfields and neighboring structures. In order to draw conclusions about atrophy and disease changes, taking into consideration only sections of this circuitry is insufficient. By including the WM and the HF subfields we are able to reach this circuitry at a gross anatomical level. It is known that the HF has two main pathways: the polysynaptic pathway and the direct pathway (see Duvernoy et al., 2013 for review). Briefly, the polysynaptic pathway originates in the entorhinal cortex (Amaral & Insausti, 1990) and perforates the subiculum in order to synapse on the DG. From here, axons from the DG then synapse on those present in the CA4 and CA3. Axons then project to the CA1 followed by subiculum before leaving the HF via the alveus and fimbria. On the other hand, the direct pathway simply connects the entorhinal cortex to the CA1. Axons then synapse in the subiculum and back down to the entorhinal cortex (Du et al., 1993; MacLean, 1992). Taking into consideration that the entorhinal cortex is the first site of AD-related pathology (Braak & Braak, 1991; Gomez-Isla et al., 1996; Moreno et al., 2007; Whitwell et al., 2007) and that MR-identified structural atrophy has been shown to occur first in this region (Dickerson, 2001; Du et al., 2001; Killiany et al., 2000; 2002; Miller et al., 2015; Pennanen et al., 2004; Varon, Loewenstein, Potter, & Greig, 2011; Visser et al., 1999; see Zhou, Zhang, Zhao, Qian, & Dong, 2015 for review), our results are therefore justifiable at the circuit level. Specifically, early atrophy of the entorhinal cortex may implicate the distal structures involved in its downstream circuitry. Since the first synapse of the direct pathway involves the CA1, the observed CA1 atrophy is logical. Our observed atrophy with respect to the subiculum and

CA4/DG in AD/MCI can also be explained given the fact that these regions consecutively mimic the connections within the perforant pathway. Following this logic, atrophy beginning in one region would propagate to connecting regions occurring downstream. This idea fits with the cell-cell interaction hypothesis of AD (i.e. prion-like theory of AD) where the spread of pathogenesis is dependent on brain circuitry and spreads from cell to cell in a prion-like manner (Miller et al., 2015; Small, Schobel, Buxton, Witter, & Barnes, 2011; see Brundin, Melki, & Kopito, 2010 for general review; see Yin, Tan, Jiang, & Yu, 2014 for AD-relative review). In fact, these results have been mimicked in *ex-vivo* studies where the loss of afferents from the entorhinal cortex to the DG can cause DG atrophy (Scheff, Price, Schmitt, & Mufson, 2006). Surprisingly, the final output afferents of the alveus were not found to suffer from volumetric changes despite that its deterioration has already been observed in AD (Mizutani & Kasahara, 1995).

Continuing with this line of thinking, the preservation of CA1 and alveus regions in our healthy aging sample can be explained by the possible strengthening of an older, more controversial pathway; the alvear pathway. Although its existence has been a subject of debate in humans, this pathway first described by (Cajal, 1911) has been shown in rats (Deller et al., 1996). This is different then the perforant pathway since axonal projections here first travel through the alveus to reach the CA1 rather than perforating through the subiculum (Mizutani & Kasahara, 1995). Not only did we identify increases in alveus and CA1 volume throughout healthy aging, we also found structural correlations between these two regions. Taken together, these results could reveal some sort of neuroprotective effect mediated by the CA1 and/or alveus.

The results obtained are also important on a clinical level. Given that the patterns of WM decreases observed in MCI and AD cohorts contrasted with results in the healthy aging cohort, these regions may serve as viable biomarkers for disease onset or even treatment options. Interestingly, the failure of pharmacological approaches has motivated increased interest in deep brain stimulation (DBS) for the treatment of AD; a therapy that has shown positive results in other neurodegenerative diseases such as Parkinson's disease (Deep-Brain Stimulation for Parkinson's Disease Study Group, 2001). While many treatment targets have been suggested for AD (see Bick & Eskandar, 2016 for review), DBS of the fornix in rodents have shown increases

in memory capabilities (Hescham et al., 2013b; C. Zhang, Hu, Wu, Zhang, & Zhang, 2015). It is unsure weather DBS may mediate orthodromic or antidromic activation of the myelinated axons of the fornix (Hardenacke, Shubina, Bührle, & Zapf, 2013; Hescham, Lim, Jahanshahi, Blokland, & Temel, 2013a), regardless, stimulation has shown to increase cellular activity in the CA1, CA3, and DG of the HF, as well as increase neurotropic factors (Gondard et al., 2015), all of which support the stimulation of neuroprotective mechanisms. These details fit in line with our observed volumetric results; if DBS of the fornix is possible, it may have downstream volumetric effects on HF subfields, thereby approximating the results observed in healthy aging (i.e. increases in CA1 and stability of other subfields). In fact, DBS of the anterior limbs of the fornix has already been completed on 6 AD patients (Sankar et al., 2015) and demonstrated significant increases in global HF volume correlated to increases in cognitive scores for 2 patients. However, the precise volumetric measurement of HF subfields, or WM has yet to be completed. Future work should be done to identify what downstream effect fornix stimulation incurs and if changes approximate those that might be observed in normative aging.

Additionally, it is important to consider the impact that genetics may play in disease risk and onset. For example, it is well known that APOE4 is a significant risk factor for AD (Genin et al., 2011) with many studies demonstrating a dose-dependent risk in carriers of ε3 and ε4 alleles (Farrer et al., 1997). Recent investigation of the effect of APOE status on subfield volume has shown decreased subicular volume (Donix et al., 2010), as well as CA1-SLRM volume (Kerchner et al., 2014) in elderly cognitively normal participants. While increased rates of atrophy have been shown in whole-hippocampal volume of AD APOE4 carriers (Schuff et al., 2009), more focal decreases have also been observed in the CA3/DG (Mueller & Weiner, 2009) of AD patients. Understanding the effect of APOE status (and other AD-related polymorphisms) on the HF subfields and WM would help to elucidate its volumetric effect on asymptomatic and symptomatic populations. Unfortunately genetics were not included in the freely available OASIS dataset, and were not completed for the ADNI cohort. This remains an important limitation to the current work, and should be investigated in future studies.

Perhaps the most salient limitation involved the use of cross-sectional and standard (1mm isotropic) MR images in our analyses. Although the use of such images provide inherently lower

spatial information compared to high resolution images, the lack of dataset availability comprising of high resolution images for healthy aging, MCI and/or AD cohorts forced us to choose scan quantity over quality. While datasets like the Human Connectome Project (Van Essen et al., 2013) do exist and include 0.7mm isotropic scans of 897 healthy subjects aged 22-35, the limited age range forfeits the ability to complete a viable healthy aging study. This is also the case for retrospective or longitudinal data. Tied to this is our use of subsampled versions of atlases during validation. Intuitively, downsampling atlases only provides a proxy gold standard label and may cause the loss of anatomical correctness due to resampling error. In addition, the devised WM protocol can only be thought of as an approximation of structure as rules and delineations are based on available print atlases and histological papers; a limitation suffered by most manual segmentation protocols that do not derive delineations from MRI data registered to histological data (e.g. Adler et al., 2014).

Here we have presented not only a novel protocol for the segmentation of WM structures, but have also validated its use for automatic segmentation via MAGeT Brain. Additionally, we assess the changes in these regions (along with HF subfields) in healthy aging and AD/MCI. We identified significant decreases in key WM and HF regions that follow the circuit-based patterns as theorized by the prion-like spread of AD pathology. Results support a neuroprotective role of the alveus and/or CA1 regions for healthy aging. Future study of WM regions and their relation to HF subfields are needed in both health and disease. The inclusion of MTL inputs (i.e. entorhinal, perirhinal or parahippocampal cortices) in future volumetric studies should be prioritized in order to achieve a more comprehensive assessment of the entire human memory circuit. This complete assessment would also offer insight into the circuit-based findings we observed. Finally, a comparison of DWI to volume metrics for the assessment of WM regions should be done in order to better understand which are most sensitive to observing changes in the alveus, fimbria and/or fornix.

References

Adachi, M., Kawakatsu, S., Hosoya, T., Otani, K., Honma, T., Shibata, A., & Sugai, Y. (2003). Morphology of the inner structure of the hippocampal formation in Alzheimer disease. *AJNR. American Journal of Neuroradiology*, *24*(8), 1575–1581.

Adler, D. H., Pluta, J., Kadivar, S., Craige, C., Gee, J. C., Avants, B. B., & Yushkevich, P. A. (2014). Histology-derived volumetric annotation of the human hippocampal subfields in postmortem MRI. *NeuroImage*, *84*, 505–523. http://doi.org/10.1016/j.neuroimage.2013.08.067

Albert, M. S., DeKosky, S. T., Dickson, D., Dubois, B., Feldman, H. H., Fox, N. C., et al. (2011). The diagnosis of mild cognitive impairment due to Alzheimer's disease: Recommendations from the National Institute on Aging-Alzheimer's Association workgroups on diagnostic guidelines for Alzheimer's disease. *Alzheimer's & Dementia*, *7*(3), 270–279. http://doi.org/10.1016/j.jalz.2011.03.008

Aljabar, P., Heckemann, R. A., Hammers, A., Hajnal, J. V., & Rueckert, D. (2009). Multi-atlas based segmentation of brain images: Atlas selection and its effect on accuracy. *NeuroImage*, *46*(3), 726–738. http://doi.org/10.1016/j.neuroimage.2009.02.018

Amaral, D. G. (1978). A Golgi study of cell types in the hilar region of the hippocampus in the rat. *The Journal of Comparative Neurology*, *182*(4 Pt 2), 851–914.

Amaral, D. G., & Insausti, R. (1990). The human hippocampal formation. In G. Paxinos (Ed.), *The Human Nervous System*. San Diego: Academic Press.

Amaral, D. G., & Lavenex, P. (2007). Hippocampal neuroanatomy. In P. Andersen, R. Morris, D. G. Amaral, T. Bliss, & J. OKeefe (Eds.), *The Hippocampus Book*. Oxford University Press.

Amaral, D. G., Insausti, R., & Cowan, W. M. (1984). The commissural connections of the monkey hippocampal formation. *Journal of Comparative Neurology*, *224*(3), 307–336. http://doi.org/10.1002/cne.902240302

Amaral, D. G., Insausti, R., & Cowan, W. M. (1987). The entorhinal cortex of the monkey: I. Cytoarchitectonic organization. *Journal of Comparative Neurology*, *264*(3), 326–355. http://doi.org/10.1002/cne.902640305

Amaral, R. S. C., Winterburn, J. L., Pruessner, J. C., & Chakravarty, M. M. (2015). Towards the

complete volumetric assessment of the human memory circuit: Segmentation of medial temporal lobe, and subicular cortices on high-resolution 3T images. *Society for Neuroscience*. Chicago.

Andersen, P. (2007). The Hippocampus Book. Oxford University Press.

Apostolova, L. G., & Thompson, P. M. (2008). Mapping progressive brain structural changes in early Alzheimer's disease and mild cognitive impairment. *Neuropsychologia*, *46*(6), 1597–1612. http://doi.org/10.1016/j.neuropsychologia.2007.10.026

Apostolova, L. G., Dinov, I. D., Dutton, R. A., Hayashi, K. M., Toga, A. W., Cummings, J. L., & Thompson, P. M. (2006). 3D comparison of hippocampal atrophy in amnestic mild cognitive impairment and Alzheimer's disease. *Brain : a Journal of Neurology*, *129*(Pt 11), 2867–2873. http://doi.org/10.1093/brain/awl274

Apostolova, L. G., Green, A. E., Babakchanian, S., Hwang, K. S., Chou, Y.-Y., Toga, A. W., & Thompson, P. M. (2012). Hippocampal atrophy and ventricular enlargement in normal aging, mild cognitive impairment and Alzheimer's disease. *Alzheimer Disease and Associated Disorders*, *26*(1), 17–27. http://doi.org/10.1097/WAD.0b013e3182163b62

Apostolova, L. G., Zarow, C., Biado, K., Hurtz, S., Boccardi, M., Somme, J., et al. (2015). Relationship between hippocampal atrophy and neuropathology markers: a 7T MRI validation study of the EADC-ADNI Harmonized Hippocampal Segmentation Protocol. *Alzheimer"S & Dementia : the Journal of the Alzheimer"S Association*, *11*(2), 139–150. http://doi.org/10.1016/j.jalz.2015.01.001

Arevalo-Rodriguez, I., & Smailagic, N. (2015). Mini-Mental State Examination (MMSE) for the detection of Alzheimer's disease and other dementias in people with mild cognitive impairment (MCI). … Database Syst Rev.

Arnold, S. J. M., Ivleva, E. I., Gopal, T. A., Reddy, A. P., Jeon-Slaughter, H., Sacco, C. B., et al. (2015). Hippocampal volume is reduced in schizophrenia and schizoaffective disorder but not in psychotic bipolar I disorder demonstrated by both manual tracing and automated parcellation (FreeSurfer). *Schizophrenia Bulletin*, *41*(1), 233–249. http://doi.org/10.1093/schbul/sbu009

Ashton, E. A., Parker, K. J., Berg, M. J., & Chen, C. W. (1997). A novel volumetric feature extraction technique with applications to MR images. *Medical Imaging, IEEE Transactions on*, *16*(4), 365–371. http://doi.org/10.1109/42.611343

Avants, B. B., Epstein, C. L., Grossman, M., & Gee, J. C. (2008). Symmetric diffeomorphic image registration with cross-correlation: evaluating automated labeling of elderly and neurodegenerative brain. *Medical Image Analysis*, *12*(1), 26–41. http://doi.org/10.1016/j.media.2007.06.004

Balchandani, P., & Naidich, T. P. (2015). Ultra-High-Field MR Neuroimaging. *AJNR. American Journal of Neuroradiology*, *36*(7), 1204–1215. http://doi.org/10.3174/ajnr.A4180

Barnes, J., Boyes, R. G., Lewis, E. B., Schott, J. M., Frost, C., Scahill, R. I., & Fox, N. C. (2007). Automatic calculation of hippocampal atrophy rates using a hippocampal template and the boundary shift integral. *Neurobiology of Aging*, *28*(11), 1657–1663. http://doi.org/10.1016/j.neurobiolaging.2006.07.008

Basser, P. J., & Pajevic, S. (2000). Statistical artifacts in diffusion tensor MRI (DT-MRI) caused by background noise. *Magnetic Resonance in Medicine*, *44*(1), 41–50. http://doi.org/10.1002/1522-2594(200007)44:1<41::AID-MRM8>3.0.CO;2-O

Battaglini, M., Smith, S. M., Brogi, S., & De Stefano, N. (2008). Enhanced brain extraction improves the accuracy of brain atrophy estimation. *NeuroImage*, *40*(2), 583–589. http://doi.org/10.1016/j.neuroimage.2007.10.067

Baudendistel, K. T., Heverhagen, J. T., & Knopp, M. V. (2004). [Clinical MR at 3 Tesla: current status]. *Der Radiologe*, *44*(1), 11–18. http://doi.org/10.1007/s00117-003-0995-3

Bechterew, Von, W. (1900). Demonstration eines Gehims mit Zerstorung

der vorderen und inneren Theile der Himrinde beider Schlafenlappen. *Neurologisch. Zentralbl.*, *1*(19), 990–999.

Bender, A. R., Daugherty, A. M., & Raz, N. (2013). Vascular risk moderates associations between hippocampal subfield volumes and memory. *Journal of Cognitive Neuroscience*, *25*(11), 1851–1862. http://doi.org/10.1162/jocn_a_00435

Bick, S. K. B., & Eskandar, E. N. (2016). Neuromodulation for restoring memory. *Neurosurgical Focus*, *40*(5), E5. http://doi.org/10.3171/2016.3.FOCUS162

Bilir, E., Craven, W., Hugg, J., Gilliam, F., Martin, R., Faught, E., & Kuzniecky, R. (1998). Volumetric MRI of the limbic system: anatomic determinants. *Neuroradiology*, *40*(3), 138–144.

Birks, J. S. (2006). Cholinesterase inhibitors for Alzheimer's disease. (J. S. Birks, Ed.). Chichester, UK: John Wiley & Sons, Ltd. http://doi.org/10.1002/14651858.CD005593

Blackstad, T. W. (1956). Commissural connections of the hippocampal region in the rat, with special reference to their mode of termination. *Journal of Comparative Neurology*, *105*(3), 417–537. http://doi.org/10.1002/cne.901050305

Bobinski, M., de Leon, M. J., Wegiel, J., Desanti, S., Convit, A., Saint Louis, L. A., et al. (2000). The histological validation of post mortem magnetic resonance imaging-determined hippocampal volume in Alzheimer's disease. *Neuroscience*, *95*(3), 721–725.

Boccardi, M., Bocchetta, M., Apostolova, L. G., Barnes, J., Bartzokis, G., Corbetta, G., et al. (2015). Delphi definition of the EADC-ADNI Harmonized Protocol for hippocampal segmentation on magnetic resonance. *Alzheimer"S & Dementia : the Journal of the Alzheimer"S Association*, *11*(2), 126–138. http://doi.org/10.1016/j.jalz.2014.02.009

Boccardi, M., Ganzola, R., Bocchetta, M., Pievani, M., Redolfi, A., Bartzokis, G., et al. (2011). Survey of protocols for the manual segmentation of the hippocampus: preparatory steps towards a joint EADC-ADNI harmonized protocol. *Journal of Alzheimer's Disease : JAD*, *26 Suppl 3*(s3), 61–75. http://doi.org/10.3233/JAD-2011-0004

Bonilha, L., Kobayashi, E., Rorden, C., Cendes, F., & Li, L. M. (2003). Medial temporal lobe atrophy in patients with refractory temporal lobe epilepsy. *Journal of Neurology, Neurosurgery, and Psychiatry*, *74*(12), 1627–1630. http://doi.org/10.1136/jnnp.74.12.1627

Boutet, C., Chupin, M., Lehéricy, S., Marrakchi-Kacem, L., Epelbaum, S., Poupon, C., et al. (2014). Detection of volume loss in hippocampal layers in Alzheimer's disease using 7 T MRI: a feasibility study. *NeuroImage. Clinical*, *5*, 341–348. http://doi.org/10.1016/j.nicl.2014.07.011

Boyle, P. A., Wilson, R. S., Yu, L., Barr, A. M., Honer, W. G., Schneider, J. A., & Bennett, D. A. (2013). Much of late life cognitive decline is not due to common neurodegenerative pathologies. *Annals of Neurology*, *74*(3), 478–489. http://doi.org/10.1002/ana.23964

Braak, H. (2012). Architectonics of the Human Telencephalic Cortex (Vol. 4). Berlin, Heidelberg: Springer Science & Business Media. http://doi.org/10.1007/978-3-642-81522-5

Braak, H., & Braak, E. (1991). Demonstration of amyloid deposits and neurofibrillary changes in whole brain sections. *Brain Pathology (Zurich, Switzerland)*, *1*(3), 213–216.

Braak, H., & Braak, E. (1997). Frequency of Stages of Alzheimer-Related Lesions in Different Age Categories. *Neurobiology of Aging*, *18*(4), 351–357. http://doi.org/10.1016/S0197-4580(97)00056-0

Bremner, J. D., Randall, P., Scott, T. M., Bronen, R. A., Seibyl, J. P., Southwick, S. M., et al. (1995). MRI-based measurement of hippocampal volume in patients with combat-related posttraumatic stress disorder. *The American Journal of Psychiatry*, *152*(7), 973–981. http://doi.org/10.1176/ajp.152.7.973

Brundin, P., Melki, R., & Kopito, R. (2010). Prion-like transmission of protein aggregates in neurodegenerative diseases. *Nature Reviews. Molecular Cell Biology*, *11*(4), 301–307. http://doi.org/10.1038/nrm2873

C R Jack, J., Twomey, C. K., Zinsmeister, A. R., Sharbrough, F. W., Petersen, R. C., & Cascino, G. D. (1989). Anterior temporal lobes and hippocampal formations: normative volumetric measurements from MR images in young adults. *Radiology*, *172*(2), 549–554. http://doi.org/10.1148/radiology.172.2.2748838

Cabezas, M., Oliver, A., Lladó, X., Freixenet, J., & Bach Cuadra, M. (2011). A review of atlas-based segmentation for magnetic resonance brain images. *Computer Methods and Programs in Biomedicine*, *104*(3), e158–e177. http://doi.org/10.1016/j.cmpb.2011.07.015

Cajal, S. R. Y. (1911). Histologie du système nerveux de l'homme & des vertébrés.

Callen, D. J., Black, S. E., Gao, F., Caldwell, C. B., & Szalai, J. P. (2001). Beyond the hippocampus: MRI volumetry confirms widespread limbic atrophy in AD. *Neurology*, *57*(9), 1669–1674.

Carmichael, O. T., Aizenstein, H. A., Davis, S. W., Becker, J. T., Thompson, P. M., Meltzer, C. C., & Liu, Y. (2005). Atlas-based hippocampus segmentation in Alzheimer's disease and mild cognitive impairment. *NeuroImage*, *27*(4), 979–990. http://doi.org/10.1016/j.neuroimage.2005.05.005

Castilla-Ortega, E., Serrano, A., Blanco, E., Araos, P., Suárez, J., Pavón, F. J., et al. (2016). A place for the hippocampus in the cocaine addiction circuit: Potential roles for adult hippocampal neurogenesis. *Neuroscience and Biobehavioral Reviews*, *66*, 15–32. http://doi.org/10.1016/j.neubiorev.2016.03.030

Chakravarty, M. M., Steadman, P., van Eede, M. C., Calcott, R. D., Gu, V., Shaw, P., et al. (2013). Performing label-fusion-based segmentation using multiple automatically generated templates. *Human Brain Mapping*, *34*(10), 2635–2654. http://doi.org/10.1002/hbm.22092

Chételat, G., Fouquet, M., Kalpouzos, G., Denghien, I., la Sayette, De, V., Viader, F., et al. (2008). Three-dimensional surface mapping of hippocampal atrophy progression from MCI

to AD and over normal aging as assessed using voxel-based morphometry. *Neuropsychologia*, *46*(6), 1721–1731. http://doi.org/10.1016/j.neuropsychologia.2007.11.037

Chou, M.-C., Lin, Y.-R., Huang, T.-Y., Wang, C.-Y., Chung, H.-W., Juan, C.-J., & Chen, C.-Y. (2005). FLAIR diffusion-tensor MR tractography: comparison of fiber tracking with conventional imaging. *AJNR. American Journal of Neuroradiology*, *26*(3), 591–597.

Christensen, G. E., Joshi, S. C., & Miller, M. I. (1997). Volumetric transformation of brain anatomy. *Medical Imaging, IEEE Transactions on*, *16*(6), 864–877. http://doi.org/10.1109/42.650882

Cohen, M. S., DuBois, R. M., & Zeineh, M. M. (2000). Rapid and effective correction of RF inhomogeneity for high field magnetic resonance imaging. *Human Brain Mapping*, *10*(4), 204–211.

Collins, D. L., Neelin, P., Peters, T. M., & Evans, A. C. (1994). Automatic 3D intersubject registration of MR volumetric data in standardized Talairach space. *Journal of Computer Assisted Tomography*, *18*(2), 192–205.

Convit, A., de Leon, M. J., Tarshish, C., De Santi, S., Tsui, W., Rusinek, H., & George, A. (1997). Specific Hippocampal Volume Reductions in Individuals at Risk for Alzheimer's Disease. *Neurobiology of Aging*, *18*(2), 131–138. http://doi.org/10.1016/S0197-4580(97)00001-8

Cootes, T. F., Edwards, G. J., & Taylor, C. J. (2001). Active appearance models. *IEEE Transactions on Pattern …*.

Cootes, T. F., Taylor, C. J., Cooper, D. H., & Graham, J. (1995). Active Shape Models-Their Training and Application. *Computer Vision and Image Understanding*, *61*(1), 38–59. http://doi.org/10.1006/cviu.1995.1004

Copenhaver, B. R., Rabin, L. A., Saykin, A. J., Roth, R. M., Wishart, H. A., Flashman, L. A., et al. (2006). The fornix and mammillary bodies in older adults with Alzheimer's disease, mild cognitive impairment, and cognitive complaints: a volumetric MRI study. *Psychiatry Research*, *147*(2-3), 93–103. http://doi.org/10.1016/j.pscychresns.2006.01.015

Corder, E. H., Saunders, A. M., Strittmatter, W. J., Schmechel, D. E., Gaskell, P. C., Small, G. W., et al. (1993). Gene dose of apolipoprotein E type 4 allele and the risk of Alzheimer's disease in late onset families. *Science (New York, N.Y.)*, *261*(5123), 921–923.

http://doi.org/10.1126/science.8346443

Coric, V., van Dyck, C. H., Salloway, S., Andreasen, N., Brody, M., Richter, R. W., et al. (2012). Safety and Tolerability of the γ-Secretase Inhibitor Avagacestat in a Phase 2 Study of Mild to Moderate Alzheimer Disease. *Archives of Neurology*, *69*(11), 1430–1440. http://doi.org/10.1001/archneurol.2012.2194

Corkin, S. (1984). Lasting consequences of bilateral medial temporal lobectomy: Clinical course and experimental findings in HM. *Seminars in Neurology*.

Coupé, P., Manjón, J. V., Fonov, V., Pruessner, J., Robles, M., & Collins, D. L. (2011). Patch-based segmentation using expert priors: Application to hippocampus and ventricle segmentation. *NeuroImage*, *54*(2), 940–954. http://doi.org/10.1016/j.neuroimage.2010.09.018

Csernansky, J. G., Wang, L., Joshi, S., Miller, J. P., Gado, M., Kido, D., et al. (2000). Early DAT is distinguished from aging by high-dimensional mapping of the hippocampus. Dementia of the Alzheimer type. *Neurology*, *55*(11), 1636–1643.

Cui, Y., Sachdev, P. S., Lipnicki, D. M., Jin, J. S., Luo, S., Zhu, W., et al. (2012). Predicting the development of mild cognitive impairment: a new use of pattern recognition. *NeuroImage*, *60*(2), 894–901. http://doi.org/10.1016/j.neuroimage.2012.01.084

de Flores, R., La Joie, R., Landeau, B., Perrotin, A., Mézenge, F., La Sayette, de, V., et al. (2015). Effects of age and Alzheimer's disease on hippocampal subfields: comparison between manual and FreeSurfer volumetry. *Human Brain Mapping*, *36*(2), 463–474. http://doi.org/10.1002/hbm.22640

de Nó, R. L. (1934). Studies on the structure of the cerebral cortex. II. Continuation of the study of the ammonic system. *Journal Für Psychologie Und Neurologie*.

Deep-Brain Stimulation for Parkinson's Disease Study Group. (2001). Deep-brain stimulation of the subthalamic nucleus or the pars interna of the globus pallidus in Parkinson's disease. *The New England Journal of Medicine*, *345*(13), 956–963.

Deller, T., Adelmann, G., Nitsch, R., & Frotscher, M. (1996). The alvear pathway of the rat hippocampus. *Cell and Tissue Research*, *286*(3), 293–303. http://doi.org/10.1007/s004410050699

Despotović, I., Goossens, B., & Philips, W. (2015). MRI segmentation of the human brain: challenges, methods, and applications. *Computational and Mathematical Methods in*

Medicine, *2015*(6), 450341–23. http://doi.org/10.1155/2015/450341

deToledo-Morrell, L., Stoub, T. R., Bulgakova, M., Wilson, R. S., Bennett, D. A., Leurgans, S., et al. (2004). MRI-derived entorhinal volume is a good predictor of conversion from MCI to AD. *Neurobiology of Aging*, *25*(9), 1197–1203. http://doi.org/10.1016/j.neurobiolaging.2003.12.007

Dice, L. R. (1945). Measures of the Amount of Ecologic Association Between Species. *Ecology*, *26*(3), 297. http://doi.org/10.2307/1932409

Dickerson, B. (2001). MRI-derived entorhinal and hippocampal atrophy in incipient and very mild Alzheimer's disease. *Neurobiology of Aging*, *22*(5), 747–754. http://doi.org/10.1016/S0197-4580(01)00271-8

Dill, V., Franco, A. R., & Pinho, M. S. (2015). Automated Methods for Hippocampus Segmentation: the Evolution and a Review of the State of the Art. *Neuroinformatics*, *13*(2), 133–150. http://doi.org/10.1007/s12021-014-9243-4

Donix, M., Burggren, A. C., Suthana, N. A., Siddarth, P., Ekstrom, A. D., Krupa, A. K., et al. (2010). Longitudinal changes in medial temporal cortical thickness in normal subjects with the APOE-4 polymorphism. *NeuroImage*, *53*(1), 37–43.

Doody, R. S., Raman, R., Farlow, M., Iwatsubo, T., Vellas, B., Joffe, S., et al. (2013). A phase 3 trial of semagacestat for treatment of Alzheimer's disease. *The New England Journal of Medicine*, *369*(4), 341–350. http://doi.org/10.1056/NEJMoa1210951

Doody, R. S., Thomas, R. G., Farlow, M., Iwatsubo, T., Vellas, B., Joffe, S., et al. (2014). Phase 3 Trials of Solanezumab for Mild-to-Moderate Alzheimer's Disease. *Dx.Doi.org*, *370*(4), 311–321. http://doi.org/10.1056/NEJMoa1312889

Douglas, J. (1995). MRI-based measurement of hippocampal volume in patients with combat-related posttraumatic stress disorder. *The American Journal of Psychiatry*.

Du, A. T., Schuff, N., Amend, D., Laakso, M. P., Hsu, Y. Y., Jagust, W. J., et al. (2001). Magnetic resonance imaging of the entorhinal cortex and hippocampus in mild cognitive impairment and Alzheimer's disease. *Journal of Neurology, Neurosurgery, and Psychiatry*, *71*(4), 441–447. http://doi.org/10.1136/jnnp.71.4.441

Du, F., Whetsell, W. O., Abou-Khalil, B., Blumenkopf, B., Lothman, E. W., & Schwarcz, R. (1993). Preferential neuronal loss in layer III of the entorhinal cortex in patients with temporal lobe epilepsy. *Epilepsy Research*, *16*(3), 223–233.

Duchesne, S., Pruessner, J. C., & Collins, D. L. (2002). Appearance-Based Segmentation of Medial Temporal Lobe Structures. *NeuroImage*, *17*(2), 515–531. http://doi.org/10.1006/nimg.2002.1188

Duncan, K., Tompary, A., & Davachi, L. (2014). Associative encoding and retrieval are predicted by functional connectivity in distinct hippocampal area CA1 pathways. *The Journal of Neuroscience : the Official Journal of the Society for Neuroscience*, *34*(34), 11188–11198. http://doi.org/10.1523/JNEUROSCI.0521-14.2014

Duvernoy, H. M., Cattin, F., & Risold, P.-Y. (2013). The Human Hippocampus. Berlin, Heidelberg: Springer Science & Business Media. http://doi.org/10.1007/978-3-642-33603-4

Ekstrom, A. D., Bazih, A. J., Suthana, N. A., Al-Hakim, R., Ogura, K., Zeineh, M., et al. (2009). Advances in high-resolution imaging and computational unfolding of the human hippocampus. *NeuroImage*, *47*(1), 42–49. http://doi.org/10.1016/j.neuroimage.2009.03.017

Elmaoğlu, M., & Çelik, A. (2011). MRI handbook: MR physics, patient positioning, and protocols.

Eskildsen, S. F., Coupé, P., Fonov, V., Manjón, J. V., Leung, K. K., Guizard, N., et al. (2012). BEaST: brain extraction based on nonlocal segmentation technique. *NeuroImage*, *59*(3), 2362–2373. http://doi.org/10.1016/j.neuroimage.2011.09.012

Fage, B. A., Chan, C., & Gill, S. S. (2015). Mini-Cog for the diagnosis of Alzheimer's disease dementia and other dementias within a community setting. … : New.

Farrer, L. A., Cupples, L. A., Haines, J. L., Hyman, B., Kukull, W. A., Mayeux, R., et al. (1997). Effects of Age, Sex, and Ethnicity on the Association Between Apolipoprotein E Genotype and Alzheimer Disease: A Meta-analysis. *Jama*, *278*(16), 1349–1356. http://doi.org/10.1001/jama.1997.03550160069041

Fischl, B. (2012). FreeSurfer. *NeuroImage*, *62*(2), 774–781. http://doi.org/10.1016/j.neuroimage.2012.01.021

Fjell, A. M., & Walhovd, K. B. (2010). Structural brain changes in aging: courses, causes and cognitive consequences. *Reviews in the Neurosciences*, *21*(3), 187–221.

Fjell, A. M., McEvoy, L., Holland, D., Dale, A. M., & Walhovd, K. B. (2014). What is normal in normal aging? Effects of aging, amyloid and Alzheimer's disease on the cerebral cortex and the hippocampus. *Progress in Neurobiology*, *117*, 20–40. http://doi.org/10.1016/j.pneurobio.2014.02.004

Fletcher, E., Raman, M., Huebner, P., Liu, A., Mungas, D., Carmichael, O., & DeCarli, C. (2013). Loss of fornix white matter volume as a predictor of cognitive impairment in cognitively normal elderly individuals. *JAMA Neurology*, *70*(11), 1389–1395. http://doi.org/10.1001/jamaneurol.2013.3263

Freeborough, P. A., Fox, N. C., & Kitney, R. I. (1997). Interactive algorithms for the segmentation and quantitation of 3-D MRI brain scans. *Computer Methods and Programs in Biomedicine*, *53*(1), 15–25. http://doi.org/10.1016/S0169-2607(97)01803-8

Frisoni, G. B., Fox, N. C., Jack, C. R., Scheltens, P., & Thompson, P. M. (2010). The clinical use of structural MRI in Alzheimer disease. *Nature Reviews Neurology*, *6*(2), 67–77. http://doi.org/10.1038/nrneurol.2009.215

Frisoni, G. B., Ganzola, R., Canu, E., Rüb, U., Pizzini, F. B., Alessandrini, F., Zoccatelli, G., Beltramello, A., Caltagirone, C., & Thompson, P. M. (2008a). Mapping local hippocampal changes in Alzheimer's disease and normal ageing with MRI at 3 Tesla. *Brain : a Journal of Neurology*, *131*(12), 3266–3276. http://doi.org/10.1093/brain/awn280

Frisoni, G. B., Ganzola, R., Canu, E., Rüb, U., Pizzini, F. B., Alessandrini, F., Zoccatelli, G., Beltramello, A., Caltagirone, C., & Thompson, P. M. (2008b). Mapping local hippocampal changes in Alzheimer's disease and normal ageing with MRI at 3 Tesla. *Brain : a Journal of Neurology*, *131*(Pt 12), 3266–3276. http://doi.org/10.1093/brain/awn280

Frisoni, G. B., Jack, C. R., Bocchetta, M., Bauer, C., Frederiksen, K. S., Liu, Y., et al. (2015). The EADC-ADNI Harmonized Protocol for manual hippocampal segmentation on magnetic resonance: evidence of validity. *Alzheimer"S & Dementia : the Journal of the Alzheimer"S Association*, *11*(2), 111–125. http://doi.org/10.1016/j.jalz.2014.05.1756

Frisoni, G. B., Sabattoli, F., Lee, A. D., Dutton, R. A., Toga, A. W., & Thompson, P. M. (2006). In vivo neuropathology of the hippocampal formation in AD: a radial mapping MR-based study. *NeuroImage*, *32*(1), 104–110. http://doi.org/10.1016/j.neuroimage.2006.03.015

Friston, K. J., Ashburner, J., Frith, C. D., Poline, J. B., Heather, J. D., & Frackowiak, R. S. J. (1995). Spatial registration and normalization of images. *Human Brain Mapping*, *3*(3), 165–189. http://doi.org/10.1002/hbm.460030303

Gale, S. D., Johnson, S. C., Bigler, E. D., & Blatter, D. D. (1995). Nonspecific white matter degeneration following traumatic brain injury. *Journal of the International Neuropsychological Society : JINS*, *1*(1), 17–28.

Genin, E., Hannequin, D., Wallon, D., Sleegers, K., Hiltunen, M., Combarros, O., et al. (2011). APOE and Alzheimer disease: a major gene with semi-dominant inheritance. *Molecular Psychiatry*, *16*(9), 903–907. http://doi.org/10.1038/mp.2011.52

Gerardin, E., Chételat, G., Chupin, M., Cuingnet, R., Desgranges, B., Kim, H.-S., et al. (2009). Multidimensional classification of hippocampal shape features discriminates Alzheimer's disease and mild cognitive impairment from normal aging. *NeuroImage*, *47*(4), 1476–1486. http://doi.org/10.1016/j.neuroimage.2009.05.036

Geuze, E., Vermetten, E., & Bremner, J. D. (2005). MR-based in vivo hippocampal volumetrics: 1. Review of methodologies currently employed. *Molecular Psychiatry*, *10*(2), 147–159. http://doi.org/10.1038/sj.mp.4001580

Ghanei, A., Soltanian-Zadeh, H., & Windham, J. P. (1998). A 3D deformable surface model for segmentation of objects from volumetric data in medical images. *Computers in Biology and Medicine*, *28*(3), 239–253. http://doi.org/10.1016/S0010-4825(98)00007-9

Glees, P., & Griffith, H. B. (1952). Bilateral destruction of the hippocampus (cornu ammonis) in a case of dementia. *Monatsschrift Für Psychiatrie Und Neurologie*, *123*(4-5), 193–204. http://doi.org/10.1159/000140010

Gomez-Isla, T., Price, J. L., McKeel, D. W., Morris, J. C., Growdon, J. H., & Hyman, B. T. (1996). Profound loss of layer II entorhinal cortex neurons occurs in very mild Alzheimer's disease. *The Journal of Neuroscience : the Official Journal of the Society for Neuroscience*, *16*(14), 4491–4500.

Gondard, E., Chau, H. N., Mann, A., Tierney, T. S., Hamani, C., Kalia, S. K., & Lozano, A. M. (2015). Rapid Modulation of Protein Expression in the Rat Hippocampus Following Deep Brain Stimulation of the Fornix. *Brain Stimulation*, *8*(6), 1058–1064. http://doi.org/10.1016/j.brs.2015.07.044

Gosche, K. M., Mortimer, J. A., Smith, C. D., Markesbery, W. R., & Snowdon, D. A. (2002). Hippocampal volume as an index of Alzheimer neuropathology: findings from the Nun Study. *Neurology*, *58*(10), 1476–1482.

Gratwicke, J., Kahan, J., Zrinzo, L., Hariz, M., Limousin, P., Foltynie, T., & Jahanshahi, M. (2013). The nucleus basalis of Meynert: a new target for deep brain stimulation in dementia? *Neuroscience and Biobehavioral Reviews*, *37*(10 Pt 2), 2676–2688. http://doi.org/10.1016/j.neubiorev.2013.09.003

Grünthal, E. (1947). Über das klinische Bild nach umschriebenem beiderseitigem Ausfall der Ammonshornrinde. *European Neurology*.

Gunbey, H. P., Ercan, K., Fındıkoglu, A. S., Bulut, H. T., Karaoglanoglu, M., & Arslan, H. (2014). The limbic degradation of aging brain: a quantitative analysis with diffusion tensor imaging. *TheScientificWorldJournal*, *2014*(3), 196513–7. http://doi.org/10.1155/2014/196513

Haller, J. W., Banerjee, A., Christensen, G. E., Gado, M., Joshi, S., Miller, M. I., et al. (1997). Three-dimensional hippocampal MR morphometry with high-dimensional transformation of a neuroanatomic atlas. *Radiology*, *202*(2), 504–510. http://doi.org/10.1148/radiology.202.2.9015081

Hanseeuw, B. J., Van Leemput, K., Kavec, M., Grandin, C., Seron, X., & Ivanoiu, A. (2011). Mild cognitive impairment: differential atrophy in the hippocampal subfields. *AJNR. American Journal of Neuroradiology*, *32*(9), 1658–1661. http://doi.org/10.3174/ajnr.A2589

Hao, Y., Wang, T., Zhang, X., Duan, Y., Yu, C., Jiang, T., et al. (2014). Local label learning (LLL) for subcortical structure segmentation: application to hippocampus segmentation. *Human Brain Mapping*, *35*(6), 2674–2697. http://doi.org/10.1002/hbm.22359

Hardenacke, K., Shubina, E., Bührle, C. P., & Zapf, A. (2013). Deep brain stimulation as a tool for improving cognitive functioning in Alzheimer's dementia: a systematic review. *Front ...*.

Hashemi, R. H., Bradley, W. G., & Lisanti, C. J. (2010). MRI. Lippincott Williams & Wilkins.

Haukvik, U. K., Westlye, L. T., Mørch-Johnsen, L., Jørgensen, K. N., Lange, E. H., Dale, A. M., et al. (2015). In vivo hippocampal subfield volumes in schizophrenia and bipolar disorder. *Biological Psychiatry*, *77*(6), 581–588. http://doi.org/10.1016/j.biopsych.2014.06.020

Heckemann, R. A., Hajnal, J. V., Aljabar, P., Rueckert, D., & Hammers, A. (2006). Automatic anatomical brain MRI segmentation combining label propagation and decision fusion. *NeuroImage*, *33*(1), 115–126. http://doi.org/10.1016/j.neuroimage.2006.05.061

Hescham, S., Lim, L. W., Jahanshahi, A., Blokland, A., & Temel, Y. (2013a). Deep brain stimulation in dementia-related disorders. *Neuroscience and Biobehavioral Reviews*, *37*(10), 2666–2675. http://doi.org/10.1016/j.neubiorev.2013.09.002

Hescham, S., Lim, L. W., Jahanshahi, A., Steinbusch, H. W. M., Prickaerts, J., Blokland, A., & Temel, Y. (2013b). Deep brain stimulation of the forniceal area enhances memory functions in experimental dementia: The role of stimulation parameters. *Brain Stimulation: Basic,*

Translational, and Clinical Research in Neuromodulation, *6*(1), 72–77. http://doi.org/10.1016/j.brs.2012.01.008

Hogan, R. E., Mark, K. E., Choudhuri, I., Wang, L., Joshi, S., Miller, M. I., & Bucholz, R. D. (2000). Magnetic resonance imaging deformation-based segmentation of the hippocampus in patients with mesial temporal sclerosis and temporal lobe epilepsy. *Journal of Digital Imaging*, *13*(1), 217–218. http://doi.org/10.1007/BF03167670

Holmes, C. J., Hoge, R., Collins, L., Woods, R., Toga, A. W., & Evans, A. C. (1998). Enhancement of MR images using registration for signal averaging. *Journal of Computer Assisted Tomography*, *22*(2), 324–333.

Hu, S., Coupé, P., Pruessner, J. C., & Collins, D. L. (2011). Appearance-based modeling for segmentation of hippocampus and amygdala using multi-contrast MR imaging. *NeuroImage*, *58*(2), 549–559. http://doi.org/10.1016/j.neuroimage.2011.06.054

Huang, H., Fan, X., Weiner, M., Martin-Cook, K., Xiao, G., Davis, J., et al. (2012). Distinctive disruption patterns of white matter tracts in Alzheimer's disease with full diffusion tensor characterization. *Neurobiology of Aging*, *33*(9), 2029–2045. http://doi.org/10.1016/j.neurobiolaging.2011.06.027

Iglesias, J. E., Augustinack, J. C., Nguyen, K., Player, C. M., Player, A., Wright, M., et al. (2015). A computational atlas of the hippocampal formation using ex vivo, ultra-high resolution MRI: Application to adaptive segmentation of in vivo MRI. *NeuroImage*, *115*, 117–137. http://doi.org/10.1016/j.neuroimage.2015.04.042

Insausti, R., Juottonen, K., Soininen, H., Insausti, A. M., Partanen, K., Vainio, P., et al. (1998). MR volumetric analysis of the human entorhinal, perirhinal, and temporopolar cortices. *AJNR. American Journal of Neuroradiology*, *19*(4), 659–671.

Jack, C. R. (1994). MRI-based hippocampal volume measurements in epilepsy. *Epilepsia*, *35 Suppl 6*, S21–9.

Jack, C. R., Dickson, D. W., Parisi, J. E., Xu, Y. C., Cha, R. H., O'Brien, P. C., et al. (2002). Antemortem MRI findings correlate with hippocampal neuropathology in typical aging and dementia. *Neurology*, *58*(5), 750–757.

Jack, C. R., Petersen, R. C., Xu, Y., O'Brien, P. C., & Smith, G. E. (1998). Rate of medial temporal lobe atrophy in typical aging and Alzheimer's disease. *Neurology*.

Jenkinson, M., Bannister, P., Brady, M., & Smith, S. (2002). Improved Optimization for the

Robust and Accurate Linear Registration and Motion Correction of Brain Images. *NeuroImage*, *17*(2), 825–841. http://doi.org/10.1006/nimg.2002.1132

Jin, Y., Shi, Y., Zhan, L., & Thompson, P. M. (2015). Automated multi-atlas labeling of the fornix and its integrity in alzheimer's disease. *2015 IEEE 12th International Symposium on Biomedical Imaging (ISBI 2015)*, 140–143. http://doi.org/10.1109/ISBI.2015.7163835

Jones, D. K. (2003). Determining and visualizing uncertainty in estimates of fiber orientation from diffusion tensor MRI. *Magnetic Resonance in Medicine*, *49*(1), 7–12. http://doi.org/10.1002/mrm.10331

Jones, E. G., & POWELL, T. P. S. (2016). An anatomical study of converging sensory pathways within the cerebral cortex of the monkey. *Brain : a Journal of Neurology*, *93*(4), 793–820. http://doi.org/10.1093/brain/93.4.793

Karch, C. M., & Goate, A. M. (2015). Alzheimer's Disease Risk Genes and Mechanisms of Disease Pathogenesis. *Biological Psychiatry*, *77*(1), 43–51. http://doi.org/10.1016/j.biopsych.2014.05.006

Karran, E., Mercken, M., & de Strooper, B. (2011). The amyloid cascade hypothesis for Alzheimer's disease: an appraisal for the development of therapeutics. *Nature Reviews Drug Discovery*, *10*(9), 698–712. http://doi.org/10.1038/nrd3505

Kaye, J. A., Swihart, T., Howieson, D., Dame, A., Moore, M. M., Karnos, T., et al. (1997). Volume loss of the hippocampus and temporal lobe in healthy elderly persons destined to develop dementia. *Neurology*, *48*(5), 1297–1304. http://doi.org/10.1212/WNL.48.5.1297

Kelemen, A., Székely, G., & Gerig, G. (1999). Elastic model-based segmentation of 3-D neuroradiological data sets. *Medical Imaging, IEEE Transactions on*, *18*(10), 828–839. http://doi.org/10.1109/42.811260

Kerchner, G. A., Bernstein, J. D., Fenesy, M. C., Deutsch, G. K., Saranathan, M., Zeineh, M. M., & Rutt, B. K. (2013). Shared vulnerability of two synaptically-connected medial temporal lobe areas to age and cognitive decline: a seven tesla magnetic resonance imaging study. *The Journal of Neuroscience : the Official Journal of the Society for Neuroscience*, *33*(42), 16666–16672. http://doi.org/10.1523/JNEUROSCI.1915-13.2013

Kerchner, G. A., Deutsch, G. K., Zeineh, M., Dougherty, R. F., Saranathan, M., & Rutt, B. K. (2012). Hippocampal CA1 apical neuropil atrophy and memory performance in Alzheimer's disease. *NeuroImage*, *63*(1), 194–202. http://doi.org/10.1016/j.neuroimage.2012.06.048

Kerchner, G. A., Hess, C. P., Hammond-Rosenbluth, K. E., Xu, D., Rabinovici, G. D., Kelley, D. A. C., et al. (2010). Hippocampal CA1 apical neuropil atrophy in mild Alzheimer disease visualized with 7-T MRI. *Neurology*, *75*(15), 1381–1387. http://doi.org/10.1212/WNL.0b013e3181f736a1

Kerchner, G., Berdnik, D., Shen, J., Bernstein, J., Fenesy, M., Deutsch, G., et al. (2014). ApoE4 Worsens Hippocampal CA1 Apical Neuropil Atrophy and Episodic Memory (S48.005). *Neurology*, *82*(10 Supplement), S48.005.

Khan, A. R., Cherbuin, N., Wen, W., Anstey, K. J., Sachdev, P., & Beg, M. F. (2011). Optimal weights for local multi-atlas fusion using supervised learning and dynamic information (SuperDyn): Validation on hippocampus segmentation. *NeuroImage*, *56*(1), 126–139. http://doi.org/10.1016/j.neuroimage.2011.01.078

Khan, W., Westman, E., Jones, N., Wahlund, L.-O., Mecocci, P., Vellas, B., et al. (2015). Automated Hippocampal Subfield Measures as Predictors of Conversion from Mild Cognitive Impairment to Alzheimer's Disease in Two Independent Cohorts. *Brain Topography*, *28*(5), 746–759. http://doi.org/10.1007/s10548-014-0415-1

Killiany, R. J., Gomez-Isla, T., Moss, M., Kikinis, R., Sandor, T., Jolesz, F., et al. (2000). Use of structural magnetic resonance imaging to predict who will get Alzheimer's disease. *Annals of Neurology*, *47*(4), 430–439.

Killiany, R. J., Hyman, B. T., Gomez-Isla, T., Moss, M. B., Kikinis, R., Jolesz, F., et al. (2002). MRI measures of entorhinal cortex vs hippocampus in preclinical AD. *Neurology*, *58*(8), 1188–1196. http://doi.org/10.1212/WNL.58.8.1188

Killiany, R. J., Moss, M. B., Albert, M. S., Sandor, T., Tieman, J., & Jolesz, F. (1993). Temporal Lobe Regions on Magnetic Resonance Imaging Identify Patients With Early Alzheimer's Disease. *Archives of Neurology*, *50*(9), 949–954. http://doi.org/10.1001/archneur.1993.00540090052010

Kim, H., Mansi, T., Bernasconi, N., & Bernasconi, A. (2012). Surface-based multi-template automated hippocampal segmentation: Application to temporal lobe epilepsy. *Medical Image Analysis*, *16*(7), 1445–1455. http://doi.org/10.1016/j.media.2012.04.008

Kirwan, C. B., Jones, C. K., Miller, M. I., & Stark, C. E. L. (2007). High-resolution fMRI investigation of the medial temporal lobe. *Human Brain Mapping*, *28*(10), 959–966. http://doi.org/10.1002/hbm.20331

Konrad, C., Ukas, T., Nebel, C., Arolt, V., Toga, A. W., & Narr, K. L. (2009). Defining the human hippocampus in cerebral magnetic resonance images—An overview of current segmentation protocols. *NeuroImage*, *47*(4), 1185–1195. http://doi.org/10.1016/j.neuroimage.2009.05.019

Kraff, O., Fischer, A., Nagel, A. M., Mönninghoff, C., & Ladd, M. E. (2015). MRI at 7 Tesla and above: demonstrated and potential capabilities. *Journal of Magnetic Resonance Imaging : JMRI*, *41*(1), 13–33. http://doi.org/10.1002/jmri.24573

Kuchling, J., Sinnecker, T., Bozin, I., Dörr, J., Madai, V. I., Sobesky, J., et al. (2014). [Ultrahigh field MRI in context of neurological diseases]. *Der Nervenarzt*, *85*(4), 445–458. http://doi.org/10.1007/s00115-013-3967-5

Kuzniecky, R., Bilir, E., Gilliam, F., Faught, E., Martin, R., & Hugg, J. (1999). Quantitative MRI in temporal lobe epilepsy: evidence for fornix atrophy. *Neurology*, *53*(3), 496–501.

Kwak, K., Yoon, U., Lee, D.-K., Kim, G. H., Seo, S. W., Na, D. L., et al. (2013). Fully-automated approach to hippocampus segmentation using a graph-cuts algorithm combined with atlas-based segmentation and morphological opening. *Magnetic Resonance Imaging*, *31*(7), 1190–1196. http://doi.org/10.1016/j.mri.2013.04.008

La Joie, R., Fouquet, M., Mézenge, F., Landeau, B., Villain, N., Mevel, K., et al. (2010). Differential effect of age on hippocampal subfields assessed using a new high-resolution 3T MR sequence. *NeuroImage*, *53*(2), 506–514. http://doi.org/10.1016/j.neuroimage.2010.06.024

La Joie, R., Perrotin, A., La Sayette, de, V., Egret, S., Doeuvre, L., Belliard, S., et al. (2013). Hippocampal subfield volumetry in mild cognitive impairment, Alzheimer's disease and semantic dementia. *NeuroImage. Clinical*, *3*, 155–162. http://doi.org/10.1016/j.nicl.2013.08.007

Lebel, C., Gee, M., Camicioli, R., Wieler, M., Martin, W., & Beaulieu, C. (2012). Diffusion tensor imaging of white matter tract evolution over the lifespan. *NeuroImage*, *60*(1), 340–352. http://doi.org/10.1016/j.neuroimage.2011.11.094

Lehericy, S., Baulac, M., Chiras, J., Piérot, L., Martin, N., Pillon, B., et al. (1994). Amygdalohippocampal MR volume measurements in the early stages of Alzheimer disease. *AJNR. American Journal of Neuroradiology*, *15*(5), 929–937.

Lewis, E. B., & Fox, N. C. (2004). Correction of differential intensity inhomogeneity in

longitudinal MR images. *NeuroImage*, *23*(1), 75–83. http://doi.org/10.1016/j.neuroimage.2004.04.030

Li, Y.-D., Dong, H.-B., Xie, G.-M., & Zhang, L.-J. (2013). Discriminative analysis of mild Alzheimer's disease and normal aging using volume of hippocampal subfields and hippocampal mean diffusivity: an in vivo magnetic resonance imaging study. *American Journal of Alzheimer's Disease and Other Dementias*, *28*(6), 627–633. http://doi.org/10.1177/1533317513494452

Libby, L. A., Ekstrom, A. D., Ragland, J. D., & Ranganath, C. (2012). Differential connectivity of perirhinal and parahippocampal cortices within human hippocampal subregions revealed by high-resolution functional imaging. *The Journal of Neuroscience : the Official Journal of the Society for Neuroscience*, *32*(19), 6550–6560. http://doi.org/10.1523/JNEUROSCI.3711-11.2012

Lim, H. K., Hong, S. C., Jung, W. S., Ahn, K. J., Won, W. Y., Hahn, C., et al. (2012). Automated hippocampal subfield segmentation in amnestic mild cognitive impairments. *Dementia and Geriatric Cognitive Disorders*, *33*(5), 327–333. http://doi.org/10.1159/000339588

Lim, H. K., Hong, S. C., Jung, W. S., Ahn, K. J., Won, W. Y., Hahn, C., et al. (2013). Automated segmentation of hippocampal subfields in drug-naïve patients with Alzheimer disease. *AJNR. American Journal of Neuroradiology*, *34*(4), 747–751. http://doi.org/10.3174/ajnr.A3293

Lindberg, O., Walterfang, M., Looi, J. C. L., Malykhin, N., Ostberg, P., Zandbelt, B., et al. (2012). Hippocampal shape analysis in Alzheimer's disease and frontotemporal lobar degeneration subtypes. *Journal of Alzheimer's Disease : JAD*, *30*(2), 355–365. http://doi.org/10.3233/JAD-2012-112210

Lockhart, S. N., & DeCarli, C. (2014). Structural Imaging Measures of Brain Aging. *Neuropsychology Review*, *24*(3), 271–289. http://doi.org/10.1007/s11065-014-9268-3

MacLean, P. (1992). The limbic system concept. In M. R. Trimble & T. Bolwig (Eds.), *The Temporal Lobes and the Limbic System*. Petersfeild: Wrightson Biomedical Pub Limited.

Mai, J. K., Majtanik, M., & Paxinos, G. (2015). Atlas of the Human Brain. Academic Press.

Malykhin, N. V., Lebel, R. M., Coupland, N. J., Wilman, A. H., & Carter, R. (2010). In vivo quantification of hippocampal subfields using 4.7 T fast spin echo imaging. *NeuroImage*,

49(2), 1224–1230. http://doi.org/10.1016/j.neuroimage.2009.09.042

Marcus, D. S., Wang, T. H., Parker, J., Csernansky, J. G., Morris, J. C., & Buckner, R. L. (2007). Open Access Series of Imaging Studies (OASIS): cross-sectional MRI data in young, middle aged, nondemented, and demented older adults. *Journal of Cognitive Neuroscience*, *19*(9), 1498–1507. http://doi.org/10.1162/jocn.2007.19.9.1498

Mattsson, N., Andreasson, U., Persson, S., Arai, H., Batish, S. D., Bernardini, S., et al. (2011). The Alzheimer's Association external quality control program for cerebrospinal fluid biomarkers. *Alzheimer's & Dementia*, *7*(4), 386–395.e6. http://doi.org/10.1016/j.jalz.2011.05.2243

Mattsson, N., Zetterberg, H., Hansson, O., Andreasen, N., Parnetti, L., Jonsson, M., et al. (2009). CSF Biomarkers and Incipient Alzheimer Disease in Patients With Mild Cognitive Impairment. *Jama*, *302*(4), 385–393. http://doi.org/10.1001/jama.2009.1064

McKhann, G. M., Knopman, D. S., Chertkow, H., Hyman, B. T., Jack, C. R., Kawas, C. H., et al. (2011). The diagnosis of dementia due to Alzheimer's disease: Recommendations from the National Institute on Aging-Alzheimer's Association workgroups on diagnostic guidelines for Alzheimer's disease. *Alzheimer"S & Dementia : the Journal of the Alzheimer"S Association*, *7*(3), 263–269. http://doi.org/10.1016/j.jalz.2011.03.005

Metzler-Baddeley, C., O'Sullivan, M. J., Bells, S., Pasternak, O., & Jones, D. K. (2012). How and how not to correct for CSF-contamination in diffusion MRI. *NeuroImage*, *59*(2), 1394–1403. http://doi.org/10.1016/j.neuroimage.2011.08.043

Mielke, M. M., Kozauer, N. A., Chan, K. C. G., George, M., Toroney, J., Zerrate, M., et al. (2009). Regionally-specific diffusion tensor imaging in mild cognitive impairment and Alzheimer's disease. *NeuroImage*, *46*(1), 47–55. http://doi.org/10.1016/j.neuroimage.2009.01.054

Milap A Nowrangi, P. B. R. (2015). The Fornix in Mild Cognitive Impairment and Alzheimer's Disease. *Frontiers in Aging Neuroscience*, *7*, 425. http://doi.org/10.3389/fnagi.2015.00001

Miller, M. I., Ratnanather, J. T., Tward, D. J., Brown, T., Lee, D. S., Ketcha, M., et al. (2015). Network Neurodegeneration in Alzheimer's Disease via MRI Based Shape Diffeomorphometry and High-Field Atlasing. *Frontiers in Bioengineering and Biotechnology*, *3*, 54. http://doi.org/10.3389/fbioe.2015.00054

Milner, B. (1972). Disorders of learning and memory after temporal lobe lesions in man. *Clinical*

Neurosurgery, *19*, 421–446.

Mizutani, T., & Kasahara, M. (1995). Degeneration of the intrahippocampal routes of the perforant and alvear pathways in senile dementia of Alzheimer type. *Neuroscience Letters*, *184*(2), 141–144. http://doi.org/10.1016/0304-3940(94)11190-T

Moreno, H., Wu, W. E., Lee, T., Brickman, A., Mayeux, R., Brown, T. R., & Small, S. A. (2007). Imaging the Abeta-related neurotoxicity of Alzheimer disease. *Archives of Neurology*, *64*(10), 1467–1477. http://doi.org/10.1001/archneur.64.10.1467

Morris, J. C. (1993). The Clinical Dementia Rating (CDR): current version and scoring rules. *Neurology*, *43*(11), 2412–2414.

Morris, J. C., Storandt, M., Miller, J. P., McKeel, D. W., Price, J. L., Rubin, E. H., & Berg, L. (2001). Mild Cognitive Impairment Represents Early-Stage Alzheimer Disease. *Archives of Neurology*, *58*(3), 397–405. http://doi.org/10.1001/archneur.58.3.397

Mueller, S. G., & Weiner, M. W. (2009). Selective effect of age, Apo e4, and Alzheimer's disease on hippocampal subfields. *Hippocampus*, *19*(6), 558–564. http://doi.org/10.1002/hipo.20614

Mueller, S. G., Schuff, N., Yaffe, K., Madison, C., Miller, B., & Weiner, M. W. (2010). Hippocampal atrophy patterns in mild cognitive impairment and Alzheimer's disease. *Human Brain Mapping*, *31*(9), 1339–1347. http://doi.org/10.1002/hbm.20934

Mueller, S. G., Stables, L., Du, A. T., Schuff, N., Truran, D., Cashdollar, N., & Weiner, M. W. (2007). Measurement of hippocampal subfields and age-related changes with high resolution MRI at 4T. *Neurobiology of Aging*, *28*(5), 719–726. http://doi.org/10.1016/j.neurobiolaging.2006.03.007

Mueller, S. G., Weiner, M. W., Thal, L. J., Petersen, R. C., Jack, C. R., Jagust, W., Trojanowski, J. Q., Toga, A. W., & Beckett, L. (2005a). Ways toward an early diagnosis in Alzheimer's disease: The Alzheimer's Disease Neuroimaging Initiative (ADNI). *Alzheimer's & Dementia*, *1*(1), 55–66. http://doi.org/10.1016/j.jalz.2005.06.003

Mueller, S. G., Weiner, M. W., Thal, L. J., Petersen, R. C., Jack, C., Jagust, W., Trojanowski, J. Q., Toga, A. W., & Beckett, L. (2005b). The Alzheimer's Disease Neuroimaging Initiative. *Neuroimaging Clinics of North America*, *15*(4), 869–877. http://doi.org/10.1016/j.nic.2005.09.008

Murray, M. E., Graff-Radford, N. R., Ross, O. A., Petersen, R. C., Duara, R., & Dickson, D. W.

(2011). Neuropathologically defined subtypes of Alzheimer's disease with distinct clinical characteristics: a retrospective study. *The Lancet. Neurology*, *10*(9), 785–796. http://doi.org/10.1016/S1474-4422(11)70156-9

Nishimura, D. G. (1996). Principles of magnetic resonance imaging.

Oishi, K., Mielke, M. M., Albert, M., Lyketsos, C. G., & Mori, S. (2012). The fornix sign: a potential sign for Alzheimer's disease based on diffusion tensor imaging. *Journal of Neuroimaging : Official Journal of the American Society of Neuroimaging*, *22*(4), 365–374. http://doi.org/10.1111/j.1552-6569.2011.00633.x

Olsen, R. K., Palombo, D. J., Rabin, J. S., Levine, B., Ryan, J. D., & Rosenbaum, R. S. (2013). Volumetric analysis of medial temporal lobe subregions in developmental amnesia using high-resolution magnetic resonance imaging. *Hippocampus*, *23*(10), 855–860. http://doi.org/10.1002/hipo.22153

Ostbye, T., & Crosse, E. (1994). Net economic costs of dementia in Canada. *CMAJ : Canadian Medical Association Journal = Journal De l'Association Medicale Canadienne*, *151*(10), 1457–1464.

Palombo, D. J., Amaral, R. S. C., Olsen, R. K., Müller, D. J., Todd, R. M., Anderson, A. K., & Levine, B. (2013). KIBRA polymorphism is associated with individual differences in hippocampal subregions: evidence from anatomical segmentation using high-resolution MRI. *The Journal of Neuroscience : the Official Journal of the Society for Neuroscience*, *33*(32), 13088–13093. http://doi.org/10.1523/JNEUROSCI.1406-13.2013

Parekh, M. B., Rutt, B. K., Purcell, R., Chen, Y., & Zeineh, M. M. (2015). Ultra-high resolution in-vivo 7.0T structural imaging of the human hippocampus reveals the endfolial pathway. *NeuroImage*, *112*, 1–6. http://doi.org/10.1016/j.neuroimage.2015.02.029

Park, M. T. M., Pipitone, J., Baer, L. H., Winterburn, J. L., Shah, Y., Chavez, S., et al. (2014). Derivation of high-resolution MRI atlases of the human cerebellum at 3T and segmentation using multiple automatically generated templates. *NeuroImage*, *95*, 217–231. http://doi.org/10.1016/j.neuroimage.2014.03.037

Patenaude, B., Smith, S. M., Kennedy, D. N., & Jenkinson, M. (2011). A Bayesian model of shape and appearance for subcortical brain segmentation. *NeuroImage*, *56*(3), 907–922. http://doi.org/10.1016/j.neuroimage.2011.02.046

Pelletier, A., Periot, O., Dilharreguy, B., Hiba, B., Bordessoules, M., Pérès, K., et al. (2013).

Structural hippocampal network alterations during healthy aging: a multi-modal MRI study. *Frontiers in Aging Neuroscience*, *5*, 84. http://doi.org/10.3389/fnagi.2013.00084

Pennanen, C., Kivipelto, M., Tuomainen, S., Hartikainen, P., Hänninen, T., Laakso, M. P., et al. (2004). Hippocampus and entorhinal cortex in mild cognitive impairment and early AD. *Neurobiology of Aging*, *25*(3), 303–310. http://doi.org/10.1016/S0197-4580(03)00084-8

Pereira, J. B., Valls-Pedret, C., Ros, E., Palacios, E., Falcón, C., Bargalló, N., et al. (2014). Regional vulnerability of hippocampal subfields to aging measured by structural and diffusion MRI. *Hippocampus*, *24*(4), 403–414. http://doi.org/10.1002/hipo.22234

Petersen, R. C. (2016). Mild Cognitive Impairment. *Continuum (Minneapolis, Minn.)*, *22*(2 Dementia), 404–418. http://doi.org/10.1212/CON.0000000000000313

Petersen, R. C., Smith, G. E., Waring, S. C., Ivnik, R. J., Kokmen, E., & Tangelos, E. G. (1997). Aging, Memory, and Mild Cognitive Impairment. *International Psychogeriatrics*, *9*(S1), 65–69. http://doi.org/10.1017/S1041610297004717

Petersen, R. C., Smith, G. E., Waring, S. C., Ivnik, R. J., Tangalos, E. G., & Kokmen, E. (1999). Mild Cognitive Impairment: Clinical Characterization and Outcome. *Archives of Neurology*, *56*(3), 303–308. http://doi.org/10.1001/archneur.56.3.303

Pipitone, J., Park, M. T. M., Winterburn, J., Lett, T. A., Lerch, J. P., Pruessner, J. C., et al. (2014). Multi-atlas segmentation of the whole hippocampus and subfields using multiple automatically generated templates. *NeuroImage*, *101*, 494–512. http://doi.org/10.1016/j.neuroimage.2014.04.054

Platero, C., Tobar, M. C., Sanguino, J., & Velasco, O. (2014). A New Label Fusion Method Using Graph Cuts: Application to Hippocampus Segmentation. In *XIII Mediterranean Conference on Medical and Biological Engineering and Computing 2013* (Vol. 41, pp. 174–177). Cham: Springer International Publishing. http://doi.org/10.1007/978-3-319-00846-2_43

Pluta, J., Avants, B. B., Glynn, S., Awate, S., & Gee, J. C. (2009). Appearance and incomplete label matching for diffeomorphic template based hippocampus segmentation. ….

Pluta, J., Yushkevich, P., Das, S., & Wolk, D. (2012). In vivo analysis of hippocampal subfield atrophy in mild cognitive impairment via semi-automatic segmentation of T2-weighted MRI. *Journal of Alzheimer's Disease : JAD*, *31*(1), 85–99. http://doi.org/10.3233/JAD-2012-111931

Preston, A. R., Bornstein, A. M., Hutchinson, J. B., Gaare, M. E., Glover, G. H., & Wagner, A. D. (2010). High-resolution fMRI of content-sensitive subsequent memory responses in human medial temporal lobe. *Journal of Cognitive Neuroscience*, *22*(1), 156–173. http://doi.org/10.1162/jocn.2009.21195

Prince, M., Bryce, R., Albanese, E., Wimo, A., Ribeiro, W., & Ferri, C. P. (2013). The global prevalence of dementia: a systematic review and metaanalysis. *Alzheimer"S & Dementia : the Journal of the Alzheimer"S Association*, *9*(1), 63–75.e2. http://doi.org/10.1016/j.jalz.2012.11.007

Pruessner, J. C., Köhler, S., Crane, J., Pruessner, M., Lord, C., Byrne, A., et al. (2002). Volumetry of temporopolar, perirhinal, entorhinal and parahippocampal cortex from high-resolution MR images: considering the variability of the collateral sulcus. *Cerebral Cortex (New York, N.Y. : 1991)*, *12*(12), 1342–1353.

Pruessner, J. C., Li, L. M., Serles, W., Pruessner, M., Collins, D. L., Kabani, N., Lupien, S., & Evans, A. C. (2000a). Volumetry of hippocampus and amygdala with high-resolution MRI and three-dimensional analysis software: minimizing the discrepancies between laboratories. *Cerebral Cortex (New York, N.Y. : 1991)*, *10*(4), 433–442.

Pruessner, J. C., Li, L. M., Serles, W., Pruessner, M., Collins, D. L., Kabani, N., Lupien, S., & Evans, A. C. (2000b). Volumetry of hippocampus and amygdala with high-resolution MRI and three-dimensional analysis software: minimizing the discrepancies between laboratories. *Cerebral Cortex (New York, N.Y. : 1991)*, *10*(4), 433–442. http://doi.org/10.1093/cercor/10.4.433

Quinn, T. J., Fearon, P., Noel-Storr, A. H., Young, C., McShane, R., & Stott, D. J. (2014). Informant Questionnaire on Cognitive Decline in the Elderly (IQCODE) for the diagnosis of dementia within community dwelling populations. *The Cochrane Database of Systematic Reviews*, *4*, CD010079. http://doi.org/10.1002/14651858.CD010079.pub2

Raz, N., & Rodrigue, K. M. (2006). Differential aging of the brain: Patterns, cognitive correlates and modifiers. *Neuroscience and Biobehavioral Reviews*, *30*(6), 730–748. http://doi.org/10.1016/j.neubiorev.2006.07.001

Raz, N., Daugherty, A. M., Bender, A. R., Dahle, C. L., & Land, S. (2015). Volume of the hippocampal subfields in healthy adults: differential associations with age and a pro-inflammatory genetic variant. *Brain Structure & Function*, *220*(5), 2663–2674.

http://doi.org/10.1007/s00429-014-0817-6

Reese, C. M., Cherry, K. E., & Copeland, A. L. (2010). Knowledge of Normal versus Pathological Memory Aging in Younger and Older Adults. *Aging, Neuropsychology, and Cognition*, *7*(1), 1–8. http://doi.org/10.1076/anec.7.1.1.809

Sabuncu, M. R., Yeo, B. T. T., Van Leemput, K., Fischl, B., & Golland, P. (2010). A Generative Model for Image Segmentation Based on Label Fusion. *Medical Imaging, IEEE Transactions on*, *29*(10), 1714–1729. http://doi.org/10.1109/TMI.2010.2050897

Sala, S., Agosta, F., Pagani, E., Copetti, M., Comi, G., & Filippi, M. (2012). Microstructural changes and atrophy in brain white matter tracts with aging. *Neurobiology of Aging*, *33*(3), 488–498.e2. http://doi.org/10.1016/j.neurobiolaging.2010.04.027

Salloway, S., Sperling, R., Fox, N. C., Blennow, K., Klunk, W., Raskind, M., et al. (2014). Two Phase 3 Trials of Bapineuzumab in Mild-to-Moderate Alzheimer's Disease. *Dx.Doi.org*, *370*(4), 322–333. http://doi.org/10.1056/NEJMoa1304839

Sankar, T., Chakravarty, M. M., Bescos, A., Lara, M., Obuchi, T., Laxton, A. W., et al. (2015). Deep Brain Stimulation Influences Brain Structure in Alzheimer's Disease. *Brain Stimulation*, *8*(3), 645–654. http://doi.org/10.1016/j.brs.2014.11.020

Sasson, E., Doniger, G. M., Pasternak, O., Tarrasch, R., & Assaf, Y. (2013). White matter correlates of cognitive domains in normal aging with diffusion tensor imaging. *Frontiers in Neuroscience*, *7*, 32. http://doi.org/10.3389/fnins.2013.00032

Scheff, S. W., Price, D. A., Schmitt, F. A., & Mufson, E. J. (2006). Hippocampal synaptic loss in early Alzheimer's disease and mild cognitive impairment. *Neurobiology of Aging*, *27*(10), 1372–1384. http://doi.org/10.1016/j.neurobiolaging.2005.09.012

Scheltens, P., Blennow, K., Breteler, M. M. B., de Strooper, B., Frisoni, G. B., Salloway, S., & Van der Flier, W. M. (2016). Alzheimer's disease. *Lancet (London, England)*, *0*(0). http://doi.org/10.1016/S0140-6736(15)01124-1

Schmahmann, J. D., Pandya, D. N., Wang, R., Dai, G., D'Arceuil, H. E., de Crespigny, A. J., & Wedeen, V. J. (2007). Association fibre pathways of the brain: parallel observations from diffusion spectrum imaging and autoradiography. *Brain : a Journal of Neurology*, *130*(Pt 3), 630–653. http://doi.org/10.1093/brain/awl359

Schuff, N., Woerner, N., Boreta, L., Kornfield, T., Shaw, L. M., Trojanowski, J. Q., et al. (2009). MRI of hippocampal volume loss in early Alzheimer's disease in relation to ApoE genotype

and biomarkers. *Brain : a Journal of Neurology*, *132*(4), 1067–1077. http://doi.org/10.1093/brain/awp007

Scoville, W. B. (1954). The Limbic Lobe in Man*. *Journal of Neurosurgery*, *11*(1), 64–66. http://doi.org/10.3171/jns.1954.11.1.0064

Scoville, W. B., & Milner, B. (1957). Loss of recent memory after bilateral hippocampal lesions. *Journal of Neurology, Neurosurgery, and Psychiatry*, *20*(1), 11–21.

Shattuck, D. W., Sandor-Leahy, S. R., Schaper, K. A., Rottenberg, D. A., & Leahy, R. M. (2001). Magnetic Resonance Image Tissue Classification Using a Partial Volume Model. *NeuroImage*, *13*(5), 856–876. http://doi.org/10.1006/nimg.2000.0730

Sheline, Y. I., Wang, P. W., Gado, M. H., Csernansky, J. G., & Vannier, M. W. (1996). Hippocampal atrophy in recurrent major depression. *Proceedings of the National Academy of Sciences of the United States of America*, *93*(9), 3908–3913.

Shing, Y. L., Rodrigue, K. M., Kennedy, K. M., Fandakova, Y., Bodammer, N., Werkle-Bergner, M., et al. (2011). Hippocampal subfield volumes: age, vascular risk, and correlation with associative memory. *Frontiers in Aging Neuroscience*, *3*, 2. http://doi.org/10.3389/fnagi.2011.00002

Simić, G., Kostović, I., Winblad, B., & Bogdanović, N. (1997). Volume and number of neurons of the human hippocampal formation in normal aging and Alzheimer's disease. *The Journal of Comparative Neurology*, *379*(4), 482–494. http://doi.org/10.1002/(SICI)1096-9861(19970324)379:4<482::AID-CNE2>3.0.CO;2-Z

Sled, J. G., Zijdenbos, A. P., & Evans, A. C. (1998). A nonparametric method for automatic correction of intensity nonuniformity in MRI data. *IEEE Transactions on Medical Imaging*, *17*(1), 87–97. http://doi.org/10.1109/42.668698

Small, S. A., Schobel, S. A., Buxton, R. B., Witter, M. P., & Barnes, C. A. (2011). A pathophysiological framework of hippocampal dysfunction in ageing and disease. *Nature Reviews. Neuroscience*, *12*(10), 585–601. http://doi.org/10.1038/nrn3085

Smith, S. M. (2002). Fast robust automated brain extraction. *Human Brain Mapping*, *17*(3), 143–155. http://doi.org/10.1002/hbm.10062

Soininen, H. S., Partanen, K., Pitkänen, A., Vainio, P., Hänninen, T., Hallikainen, M., et al. (1994). Volumetric MRI analysis of the amygdala and the hippocampus in subjects with age-associated memory impairment: correlation to visual and verbal memory. *Neurology*, *44*(9),

1660–1668.

Sowell, E. R., Peterson, B. S., Thompson, P. M., Welcome, S. E., Henkenius, A. L., & Toga, A. W. (2003). Mapping cortical change across the human life span. *Nature Neuroscience*, *6*(3), 309–315. http://doi.org/10.1038/nn1008

Sperling, R. A., Aisen, P. S., Beckett, L. A., Bennett, D. A., Craft, S., Fagan, A. M., et al. (2011). Toward defining the preclinical stages of Alzheimer's disease: Recommendations from the National Institute on Aging-Alzheimer"s Association workgroups on diagnostic guidelines for Alzheimer"s disease. *Alzheimer's & Dementia*, *7*(3), 280–292. http://doi.org/10.1016/j.jalz.2011.03.003

Squire, L. R., Stark, C. E. L., & Clark, R. E. (2004). THE MEDIAL TEMPORAL LOBE*. *Dx.Doi.org*, *27*(1), 279–306. http://doi.org/10.1146/annurev.neuro.27.070203.144130

Strittmatter, W. J., Weisgraber, K. H., Huang, D. Y., Dong, L. M., Salvesen, G. S., Pericak-Vance, M., et al. (1993). Binding of human apolipoprotein E to synthetic amyloid beta peptide: isoform-specific effects and implications for late-onset Alzheimer disease. *Proceedings of the National Academy of Sciences of the United States of America*, *90*(17), 8098–8102.

Sullivan, E. V., Rohlfing, T., & Pfefferbaum, A. (2010). Quantitative fiber tracking of lateral and interhemispheric white matter systems in normal aging: relations to timed performance. *Neurobiology of Aging*, *31*(3), 464–481. http://doi.org/10.1016/j.neurobiolaging.2008.04.007

Suzuki, W. A., & Amaral, D. G. (1994). Topographic organization of the reciprocal connections between the monkey entorhinal cortex and the perirhinal and parahippocampal cortices. *The Journal of Neuroscience : the Official Journal of the Society for Neuroscience*, *14*(3 Pt 2), 1856–1877.

Takahashi, M., Uematsu, H., & Hatabu, H. (2003). MR imaging at high magnetic fields. *European Journal of Radiology*, *46*(1), 45–52.

Talairach, J., & Tournoux, P. (1988). Co-planar Stereotaxic Atlas of the Human Brain. George Thieme Verlag.

Tang, X., Mori, S., Ratnanather, T., & Miller, M. I. (2012). Segmentation of hippocampus and amygdala using multi-channel landmark large deformation diffeomorphic metric mapping. *2012 38th Annual Northeast Bioengineering Conference (NEBEC)*, 414–415. http://doi.org/10.1109/NEBC.2012.6207140

Tofts, P. (2003). Quantitative MRI of the Brain. John Wiley & Sons.

Tranel, D., Brady, D. R., Van Hoesen, G. W., & Damasio, A. R. (1988). Parahippocampal projections to posterior auditory association cortex (area Tpt) in Old-World monkeys. *Experimental Brain Research*, *70*(2), 406–416. http://doi.org/10.1007/BF00248365

Treadway, M. T., Waskom, M. L., Dillon, D. G., Holmes, A. J., Park, M. T. M., Chakravarty, M. M., et al. (2015). Illness progression, recent stress, and morphometry of hippocampal subfields and medial prefrontal cortex in major depression. *Biological Psychiatry*, *77*(3), 285–294. http://doi.org/10.1016/j.biopsych.2014.06.018

Tustison, N. J., Avants, B. B., Cook, P. A., Zheng, Y., Egan, A., Yushkevich, P. A., & Gee, J. C. (2010). N4ITK: improved N3 bias correction. *IEEE Transactions on Medical Imaging*, *29*(6), 1310–1320. http://doi.org/10.1109/TMI.2010.2046908

van de Pol, L. A., Hensel, A., van der Flier, W. M., Visser, P. J., Pijnenburg, Y. A. L., Barkhof, F., et al. (2006). Hippocampal atrophy on MRI in frontotemporal lobar degeneration and Alzheimer's disease. *Journal of Neurology, Neurosurgery, and Psychiatry*, *77*(4), 439–442. http://doi.org/10.1136/jnnp.2005.075341

van der Kolk, A. G., Hendrikse, J., Zwanenburg, J. J. M., Visser, F., & Luijten, P. R. (2013). Clinical applications of 7T MRI in the brain. *European Journal of Radiology*, *82*(5), 708–718. http://doi.org/10.1016/j.ejrad.2011.07.007

Van Essen, D. C., Smith, S. M., Barch, D. M., Behrens, T. E. J., Yacoub, E., Ugurbil, K., WU-Minn HCP Consortium. (2013). The WU-Minn Human Connectome Project: an overview. *NeuroImage*, *80*, 62–79. http://doi.org/10.1016/j.neuroimage.2013.05.041

Van Hoesen, G. W., & Pandya, D. N. (1975a). Some connections of the entorhinal (area 28) and perirhinal (area 35) cortices of the rhesus monkey. I. Temporal lobe afferents. *Brain Research*, *95*(1), 1–24. http://doi.org/10.1016/0006-8993(75)90204-8

Van Hoesen, G. W., & Pandya, D. N. (1975b). Some connections of the entorhinal (area 28) and perirhinal (area 35) cortices of the rhesus monkey. I. Temporal lobe afferents. *Brain Research*, *95*(1), 1–24. http://doi.org/10.1016/0006-8993(75)90204-8

Van Hoesen, G. W., & Pandya, D. N. (1975c). Some connections of the entorhinal (area 28) and perirhinal (area 35) cortices of the rhesus monkey. III. Efferent connections. *Brain Research*, *95*(1), 39–59. http://doi.org/10.1016/0006-8993(75)90206-1

Van Hoesen, G. W., Pandya, D. N., & Butters, N. (1975). Some connections of the entorhinal

(area 28) and perirhinal (area 35) cortices of the rhesus monkey. II. Frontal lobe afferents. *Brain Research*, *95*(1), 25–38. http://doi.org/10.1016/0006-8993(75)90205-X

Van Leemput, K., Bakkour, A., Benner, T., Wiggins, G., Wald, L. L., Augustinack, J., et al. (2009). Automated segmentation of hippocampal subfields from ultra-high resolution in vivo MRI. *Hippocampus*, *19*(6), 549–557. http://doi.org/10.1002/hipo.20615

Varon, D., Loewenstein, D. A., Potter, E., & Greig, M. T. (2011). Minimal atrophy of the entorhinal cortex and hippocampus: progression of cognitive impairment. *Dementia and Geriatric …*.

Videbech, P., & Ravnkilde, B. (2015). Hippocampal Volume and Depression: A Meta-Analysis of MRI Studies. *American Journal of Psychiatry*.

Villemagne, V. L., & Chételat, G. (2016). Neuroimaging biomarkers in Alzheimer's disease and other dementias. *Ageing Research Reviews*. http://doi.org/10.1016/j.arr.2016.01.004

Visser, P. J., Scheltens, P., Verhey, F. R. J., Ben Schmand, Launer, L. J., Jolles, J., & Jonker, C. (1999). Medial temporal lobe atrophy and memory dysfunction as predictors for dementia in subjects with mild cognitive impairment. *Journal of Neurology*, *246*(6), 477–485. http://doi.org/10.1007/s004150050387

Voineskos, A. N., Winterburn, J. L., Felsky, D., Pipitone, J., Rajji, T. K., Mulsant, B. H., & Chakravarty, M. M. (2015). Hippocampal (subfield) volume and shape in relation to cognitive performance across the adult lifespan. *Human Brain Mapping*, *36*(8), 3020–3037. http://doi.org/10.1002/hbm.22825

Vovk, U., Pernus, F., & Likar, B. (2007). A Review of Methods for Correction of Intensity Inhomogeneity in MRI. *Medical Imaging, IEEE Transactions on*, *26*(3), 405–421. http://doi.org/10.1109/TMI.2006.891486

Wang, L., Khan, A., Csernansky, J. G., Fischl, B., Miller, M. I., Morris, J. C., & Beg, M. F. (2009). Fully-automated, multi-stage hippocampus mapping in very mild Alzheimer disease. *Hippocampus*, *19*(6), 541–548. http://doi.org/10.1002/hipo.20616

Wang, L., Miller, J. P., Gado, M. H., McKeel, D. W., Rothermich, M., Miller, M. I., et al. (2006). Abnormalities of hippocampal surface structure in very mild dementia of the Alzheimer type. *NeuroImage*, *30*(1), 52–60. http://doi.org/10.1016/j.neuroimage.2005.09.017

Wang, L., Swank, J. S., Glick, I. E., Gado, M. H., Miller, M. I., Morris, J. C., & Csernansky, J.

G. (2003). Changes in hippocampal volume and shape across time distinguish dementia of the Alzheimer type from healthy aging. *NeuroImage*, *20*(2), 667–682. http://doi.org/10.1016/S1053-8119(03)00361-6

Watson, C., Jack, C. R., & Cendes, F. (1997). Volumetric magnetic resonance imaging. Clinical applications and contributions to the understanding of temporal lobe epilepsy. *Archives of Neurology*, *54*(12), 1521–1531.

West, M. J., Coleman, P. D., Flood, D. G., & Troncoso, J. C. (1994). Differences in the pattern of hippocampal neuronal loss in normal ageing and Alzheimer's disease. *Lancet (London, England)*, *344*(8925), 769–772.

Whitwell, J. L., Przybelski, S. A., Weigand, S. D., Knopman, D. S., Boeve, B. F., Petersen, R. C., & Jack, C. R. (2007). 3D maps from multiple MRI illustrate changing atrophy patterns as subjects progress from mild cognitive impairment to Alzheimer's disease. *Brain : a Journal of Neurology*, *130*(Pt 7), 1777–1786. http://doi.org/10.1093/brain/awm112

Williams, P. L., Bannister, L. H., Berry, M. M., & Collins, P. (1995). Gray's Anatomy. New York. Churchill Livingstone.

Wimo, A., Winblad, B., & Jönsson, L. (2007). An estimate of the total worldwide societal costs of dementia in 2005. *Alzheimer's & Dementia*, *3*(2), 81–91. http://doi.org/10.1016/j.jalz.2007.02.001

Winterburn, J. L., Pruessner, J. C., Chavez, S., Schira, M. M., Lobaugh, N. J., Voineskos, A. N., & Chakravarty, M. M. (2013). A novel in vivo atlas of human hippocampal subfields using high-resolution 3 T magnetic resonance imaging. *NeuroImage*, *74*, 254–265. http://doi.org/10.1016/j.neuroimage.2013.02.003

Wisse, L. E. M., Biessels, G. J., Heringa, S. M., Kuijf, H. J., Koek, D. H. L., Luijten, P. R., et al. (2014). Hippocampal subfield volumes at 7T in early Alzheimer's disease and normal aging. *Neurobiology of Aging*, *35*(9), 2039–2045. http://doi.org/10.1016/j.neurobiolaging.2014.02.021

Wisse, L. E. M., Gerritsen, L., Zwanenburg, J. J. M., Kuijf, H. J., Luijten, P. R., Biessels, G. J., & Geerlings, M. I. (2012). Subfields of the hippocampal formation at 7 T MRI: in vivo volumetric assessment. *NeuroImage*, *61*(4), 1043–1049. http://doi.org/10.1016/j.neuroimage.2012.03.023

Witter, M. P. (2007). The perforant path: projections from the entorhinal cortex to the dentate

gyrus. In *The Dentate Gyrus: A Comprehensive Guide to Structure, Function, and Clinical Implications* (Vol. 163, pp. 43–61). Elsevier. http://doi.org/10.1016/S0079-6123(07)63003-9

Woods, R. P., Grafton, S. T., Holmes, C. J., Cherry, S. R., & Mazziotta, J. C. (1998). Automated Image Registration: I. General Methods and Intrasubject, Intramodality Validation. *Journal of Computer Assisted Tomography*, *22*(1), 139.

Xu, J., Kober, H., Wang, X., DeVito, E. E., Carroll, K. M., & Potenza, M. N. (2014). Hippocampal volume mediates the relationship between measures of pre-treatment cocaine use and within-treatment cocaine abstinence. *Drug and Alcohol Dependence*, *143*, 74–80. http://doi.org/10.1016/j.drugalcdep.2014.07.007

Xue, H., Srinivasan, L., Jiang, S., Rutherford, M., Edwards, A. D., Rueckert, D., & Hajnal, J. V. (2007). Automatic segmentation and reconstruction of the cortex from neonatal MRI. *NeuroImage*, *38*(3), 461–477. http://doi.org/10.1016/j.neuroimage.2007.07.030

Yang, X., Goh, A., Chen, S.-H. A., & Qiu, A. (2013). Evolution of hippocampal shapes across the human lifespan. *Human Brain Mapping*, *34*(11), 3075–3085. http://doi.org/10.1002/hbm.22125

Yassa, M. A., Stark, S. M., Bakker, A., Albert, M. S., Gallagher, M., & Stark, C. E. L. (2010). High-resolution structural and functional MRI of hippocampal CA3 and dentate gyrus in patients with amnestic Mild Cognitive Impairment. *NeuroImage*, *51*(3), 1242–1252. http://doi.org/10.1016/j.neuroimage.2010.03.040

Yin, R.-H., Tan, L., Jiang, T., & Yu, J.-T. (2014). Prion-like Mechanisms in Alzheimer's Disease.

Yushkevich, P. A., Amaral, R. S. C., Augustinack, J. C., Bender, A. R., Bernstein, J. D., Boccardi, M., et al. (2015a). Quantitative comparison of 21 protocols for labeling hippocampal subfields and parahippocampal subregions in in vivo MRI: towards a harmonized segmentation protocol. *NeuroImage*, *111*, 526–541. http://doi.org/10.1016/j.neuroimage.2015.01.004

Yushkevich, P. A., Avants, B. B., Pluta, J., Das, S., Minkoff, D., Mechanic-Hamilton, D., et al. (2009). A high-resolution computational atlas of the human hippocampus from postmortem magnetic resonance imaging at 9.4 T. *NeuroImage*, *44*(2), 385–398. http://doi.org/10.1016/j.neuroimage.2008.08.042

Yushkevich, P. A., Pluta, J. B., Wang, H., Xie, L., Ding, S.-L., Gertje, E. C., et al. (2015b).

Automated volumetry and regional thickness analysis of hippocampal subfields and medial temporal cortical structures in mild cognitive impairment. *Human Brain Mapping*, *36*(1), 258–287. http://doi.org/10.1002/hbm.22627

Yushkevich, P. A., Wang, H., Pluta, J., Das, S. R., Craige, C., Avants, B. B., et al. (2010). Nearly automatic segmentation of hippocampal subfields in in vivo focal T2-weighted MRI. *NeuroImage*, *53*(4), 1208–1224. http://doi.org/10.1016/j.neuroimage.2010.06.040

Zahajszky, J., Dickey, C. C., McCarley, R. W., Fischer, I. A., Nestor, P., Kikinis, R., & Shenton, M. E. (2001). A quantitative MR measure of the fornix in schizophrenia. *Schizophrenia Research*, *47*(1), 87–97.

Zahr, N. M., Rohlfing, T., Pfefferbaum, A., & Sullivan, E. V. (2009). Problem solving, working memory, and motor correlates of association and commissural fiber bundles in normal aging: a quantitative fiber tracking study. *NeuroImage*, *44*(3), 1050–1062. http://doi.org/10.1016/j.neuroimage.2008.09.046

Zeineh, M. M., Engel, S. A., Thompson, P. M., & Bookheimer, S. Y. (2001). Unfolding the human hippocampus with high resolution structural and functional MRI. *The Anatomical Record*, *265*(2), 111–120.

Zeineh, M. M., Holdsworth, S., Skare, S., Atlas, S. W., & Bammer, R. (2012). Ultra-high resolution diffusion tensor imaging of the microscopic pathways of the medial temporal lobe. *NeuroImage*, *62*(3), 2065–2082. http://doi.org/10.1016/j.neuroimage.2012.05.065

Zhang, C., Hu, W. H., Wu, D. L., Zhang, K., & Zhang, J. G. (2015). Behavioral Effects of Deep Brain Stimulation of the Anterior Nucleus of Thalamus, Entorhinal Cortex and Fornix in a Rat Model of Alzheimer's Disease. *Chinese Medical Journal*.

Zheng, W., Chee, M. W. L., & Zagorodnov, V. (2009). Improvement of brain segmentation accuracy by optimizing non-uniformity correction using N3. *NeuroImage*, *48*(1), 73–83. http://doi.org/10.1016/j.neuroimage.2009.06.039

Zhou, M., Zhang, F., Zhao, L., Qian, J., & Dong, C. (2015). Entorhinal cortex: a good biomarker of mild cognitive impairment and mild Alzheimer's disease. *Reviews in the Neurosciences*, *0*(0). http://doi.org/10.1515/revneuro-2015-0019

Zhuang, L., Sachdev, P. S., Trollor, J. N., Reppermund, S., Kochan, N. A., Brodaty, H., & Wen, W. (2013). Microstructural white matter changes, not hippocampal atrophy, detect early amnestic mild cognitive impairment. *PloS One*, *8*(3), e58887.

http://doi.org/10.1371/journal.pone.0058887

Zillmer, E., Spiers, M., & Culbertson, W. (2007). Principles of neuropsychology.

Appendix A: Detailed Segmentation Protocol

Review of General Anatomy of Alveus, Fimbria, and Fornix:

The human hippocampal formation (HF) is enveloped by thin white matter (WM) projections emanating from within the HF. These myelinated fibers contour its trajectory through the medial temporal lobe until they aggregate near the HF tail and curve superiorly and anteriorly, projecting to the mammillary bodies. The alveus covers the majority of the anterior portion of HF head and extends along the lateral length of the HF. These myelinated fibers extend medially and coalesce forming the fimbria. The fimbria runs along the superomedial bank of the HF and transitions into the fornix, which then projects to the mammillary bodies (See Figure 12).

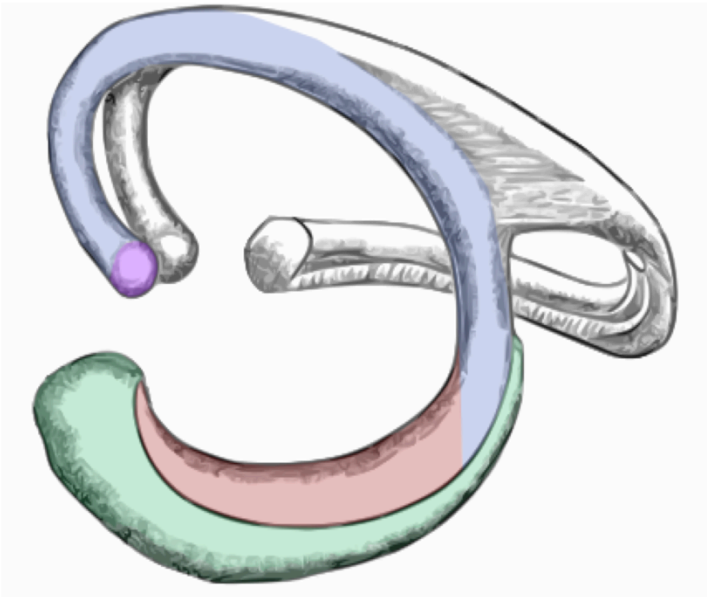

Figure 12. General depiction of hippocampal white matter anatomy. The alveus (green) covers the anterior and lateral portions of the hippocampus. The fimbria (red) begins near the hippocampal uncus region and includes all the aggregated white matter from the alveus. The fimbria continues posteriorly until it reaches the crux of the fornix. At this point the fornix (blue) curves superiorly and moves anterior to reach the midline. At its anterior-most extent, the fornix descends to meet the mamillary bodies (purple). Figure adapted and modified from Gray, Henry. Anatomy of the Human Body. Philadelphia: Lea & Febiger, 1918.

Detailed Manual Tracing Protocol:

Alveus: With most of its WM projections emanating from the subiculum and cornu ammonis (CA) 1 region, the alveus envelops the entire head of the HF superiorly, and extends along the lateral edge of the ventricular surface of the HF. It can be visibly identified as a high- or low-intensity band on T1- or T2-weighted images respectively (See Figure 13). This is consistent with all the WM structures.

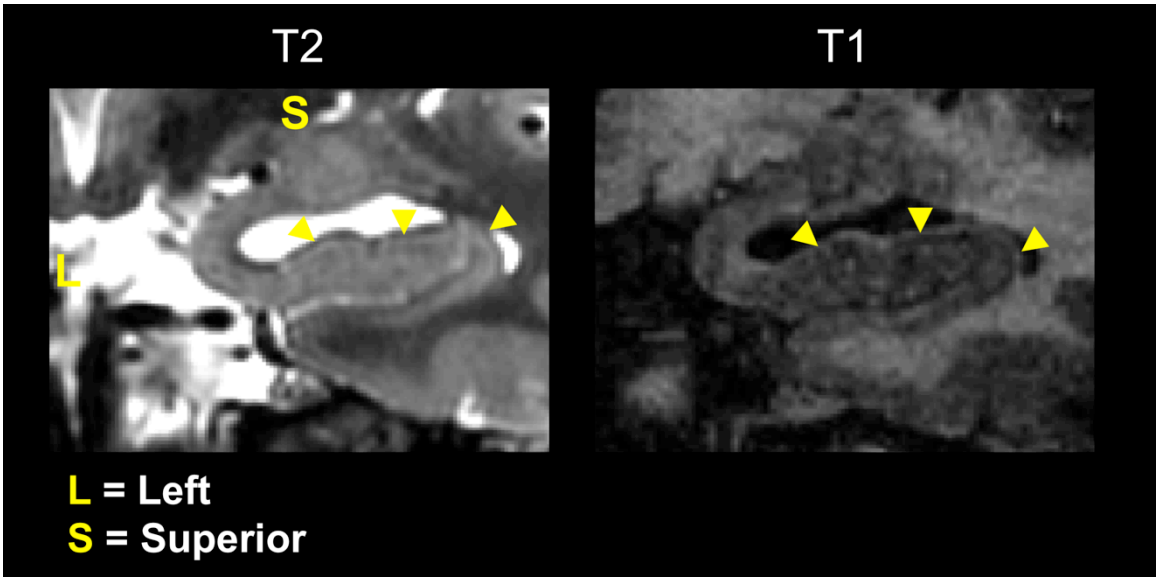

Figure 13. Image depicts a T1- and T2-weighted image of the right hippocampal head of one individual at the same coronal slice. The alveus is visible (yellow arrowheads) as it borders the ventricular surface of the hippocampus, presenting as a thin strip of high-intensity in the T1-weighted image and low-intensity on the T2-weighted image.

The coronal view in T1-weighted images were most useful for demarcation of the alveus. The sagittal and axial planes were also used to ensure accuracy and to maintain consistent morphology of segmentations across coronal slices. Anteriorly, the alveus typically can be seen 2 to 3 slices (~0.6mm) prior to the onset of the HF. Tracing of the anterior section the alveus begins when the high intensity WM structure is first visible in the coronal plane within the middle of the MTL (See Figure 14, i). This will appear as a high-intensity patch of WM in the T1-weighted image. Here, all high-intensity voxels are included as alveus. At this point the superior border of the alveus is the grey matter of the amygdala (Figure 14C, iii) and the inferior portion is the WM just superior to the entorhinal (ERC) and perirhinal (PRC) cortices. A clear division between the WM of the alveus and the more inferior WM can be seen (Figure 14C, v). The lateral border of the alveus is the temporal

horn of the lateral ventricle (Figure 14C, iv). Moving more posterior, the HF begins to emerge through the middle of the alveus (See Figure 14C, ii). At this point the alveus is still follows along the superior surface of the HF, just above the HF CA1 subregion (inferior boundary). Although the WM of the alveus extends inferior along the HF's anterior head, at this point it is indistinguishable from the WM occurring superior to the PRC and ERC. Thus, to create a reliable definition for this region, a line is drawn from the medial extremity to the lateral extremity of the HF. The alveus is therefore stopped at both the medial and lateral-most end of this line (Figure 15).

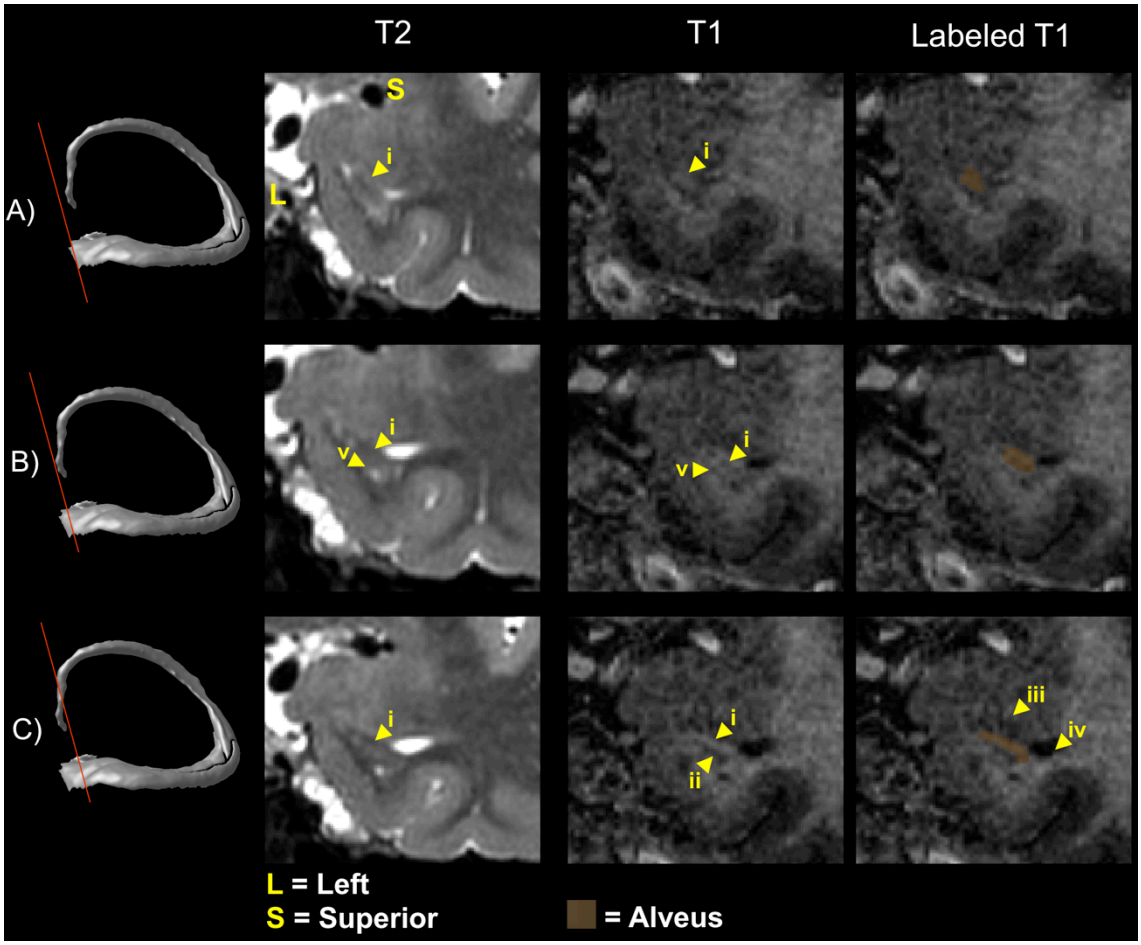

Figure 14. Coronal depiction of first appearance of right alveus and its anterior tracing methodology. Slices A) to C) are of consecutive slices from anterior to posterior. The alveus (i) first appears on the T1 image as a high intensity patch. At this point the superior boundary is the amygdala (iii). The inferior boundary is marked by the division between the WM of the alveus and the WM occurring above the MTL cortex. At this point the T1 and T2-weighted images show a line of different intensity between the two (v). This is used to guide tracing. In more anterior sections the temporal horn (iv) begins to appear and serves as a lateral border. In later slices, the hippocampus appears through the middle of the alveus (ii).

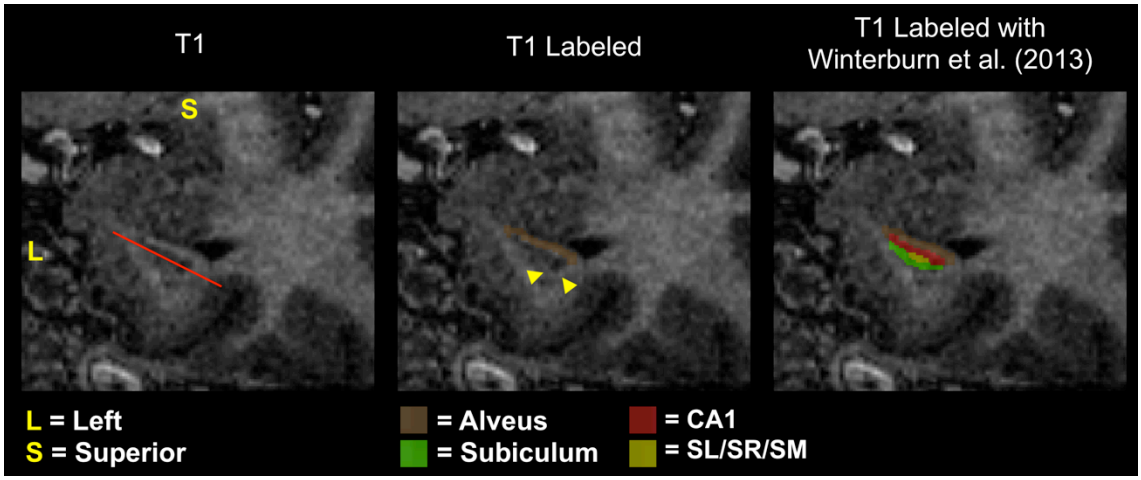

Figure 15. Coronal depiction of geometric rule for the anterior alveus once hippocampus emerges. Image depicts a coronal section through the right hippocampus of one subject. Since inferior-most sections of the alveus are not distinguishable due to the presence of WM superior to the MTL cortex ribbon (yellow arrowheads), a geometric rule also used by Winterburn et al. (2013) was used. Namely, a line (red line) is drawn from the medial extremity to the lateral extremity of the hippocampus. Tracing of the alveus is then ceased at both the medial and lateral extremities of this line. The grey matter of the CA1 region serves as an inferior boundary.

The above geometric rule continues until the HF extends medially (prior to the disappearance of the ambient gyrus) and the lateral side begins to rise out into the temporal horn of the lateral ventricle. At this point, the superior boundary is still the amygdala (or CSF of the lateral ventricle). Medially, the high-intensity alveus is followed as far as it is visible. The inferior boundary remains to be the surface of the HF (i.e. the CA1 subregion). As stated above, the alveus curves around the lateral to the inferior portion of the HF. Since the alveus is still indistinguishable from the WM occurring inferior to the HF, a consistently reliable definition is again required. Thus, the lateral extremity of the WM of the alveus is drawn until the alveus meets the lateral ventricle near the inferomedial area of the HF (See Figure 16, iii). Moving posteriorly, the isthmus of the HF is visible medially. The alveus continues superomedially along the isthmus until it is no longer visible (Figure 16, iv). At its lateral extremity, and near the superiolateral part of the alveus, special care must be taken so as not to include parts of the choroid plexus or partial volumes from the CSF region. For this, it is most useful to use the sagittal sections to ensure strict identification of the alveus (See Figure 17). In addition, the sagittal sections can also be useful for ensuring that the medial definition of the alveus (terminating where it meets the inferior part of the lateral ventricle) is satisfied.

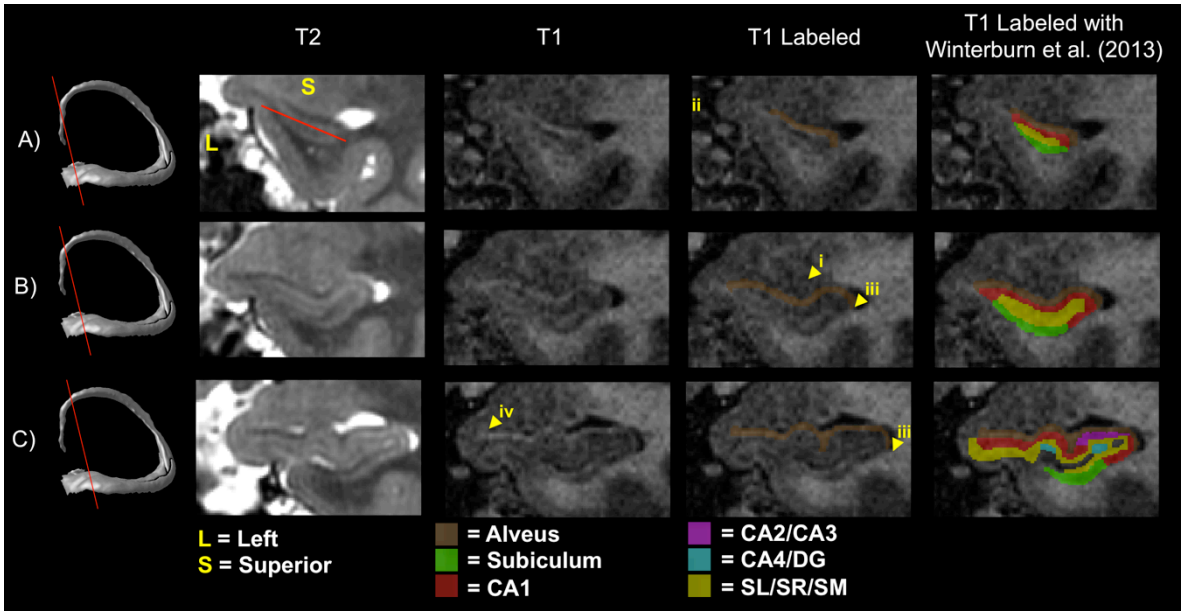

Figure 16. Landmarks and tracing methodology for identification of alveus along more posterior portions of the hippocampal head. Image depicts coronal sections through the right hippocampus of one subject. Rows A) to C) represent slices from anterior to posterior. Images depict the right hippocampus with alveus. The superior border remains the amygdala (i). When the hippocampus rises and extends medially into the lateral ventricle (prior to the disappearance of the ambient cistern, ii), the lateral extent of the alveus extends to where the alveus meets the lateral ventricle (iii). The medial extent of the alveus is drawn until contrast disappears (iv).

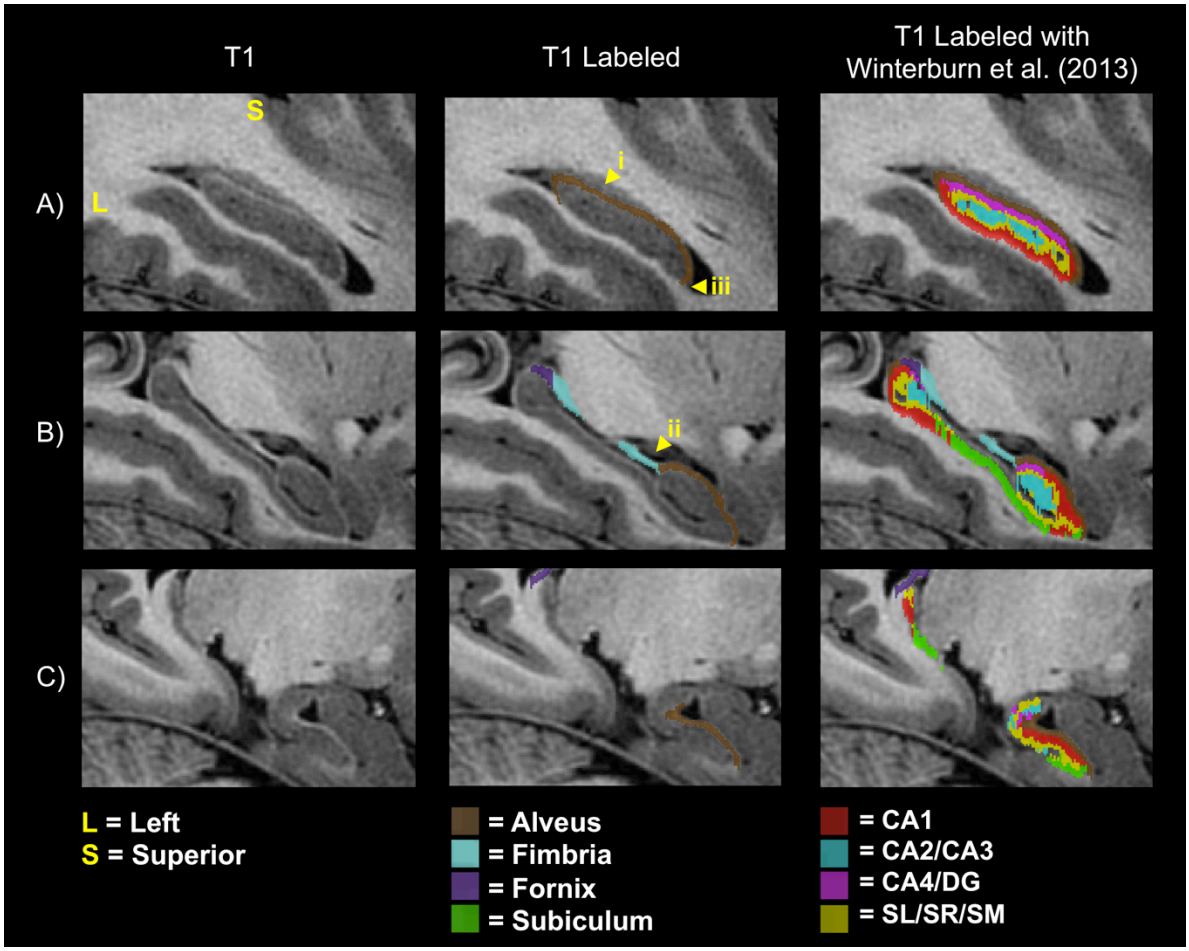

Figure 17. Sagittal sections of the right alveus. Image depicts sagittal sections through the right hippocampus of one subject. Rows A) to C) represent slices from lateral to medial. Sagittal and axial sections were most useful for segmentation. Sagittal sections can be used to ensure partial volumes from CSF (i) or choroid plexus (ii) are not included in segmentations. In addition, sagittal slices allow the tracer to ensure the medial definition of the alveus (i.e. extends to where the alveus and lateral ventricle meet) is being satisfied (iii).

Moving posterior, the HF head bifurcates following the emergence of the uncal sulcus (Figure 18, ii). The slice at which the uncal sulcus first appears is when the alveus no longer extends medially to include the entire WM ribbon occurring superior to the HF. Instead, tracing includes all high-intensity signal associated with the alveus medially until the end of the lateral most undulation of the HF (i.e. area where the teardrop shape of the HF body forms; See Figure 18, iii). The lateral part of the WM ribbon excluded from the alveus is the fimbria (Figure 18, iv). At this point the lateral, superior and inferior borders of the alveus are the same as listed previously. Once the WM superior to the HF uncus rises to lift off of the uncus (Figure 18, v), the alveus extends medially over ¾ of the lateral most undulation of the HF body (Figure 18, vi). Once in the body of the HF (and the uncus disappears), tracing becomes easier. The body of the HF is denoted by the tight, condensed curved c-shape structure (Figure 18, C). At this point, the WM

ribbon sitting superior to the HF body is bisected (i.e. at the half way point; Figure 18, vii), serving as the medial boundary of the alveus. This continues all the way through the body of the HF until the HF tail is reached. Again, all views should be employed to ensure that choroid plexus is not included in demarcation of the alveus (Figure 18, viii).

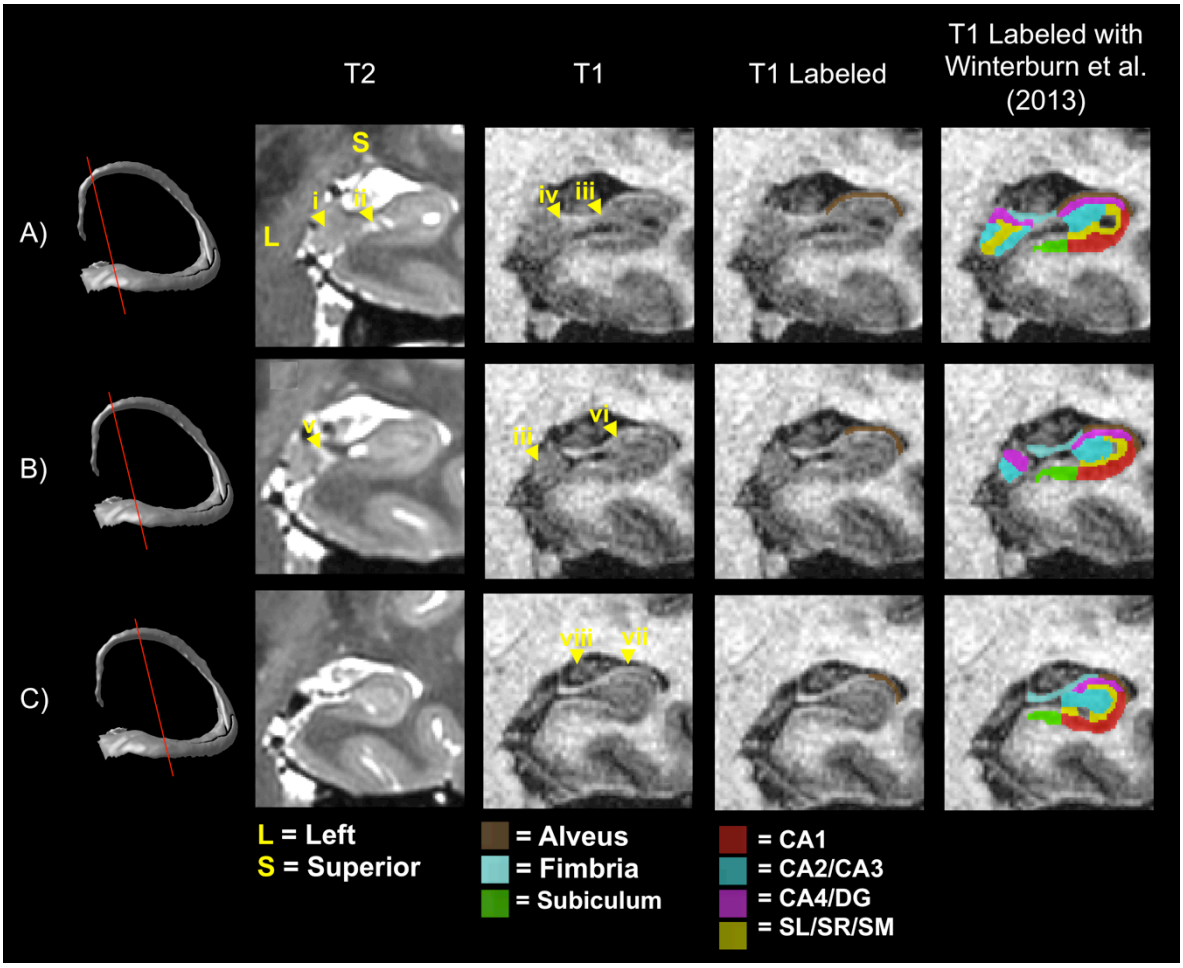

Figure 18. Description of protocol for segmentation of the alveus near the bifurcation of the hippocampal head. Image depicts coronal sections through the right hippocampus of one subject. Rows A) to C) represent slices from anterior to posterior. Anteriorly, the hippocampal head bifurcates following the emergence of the hippocampal uncus region (i) and uncal sulcus (ii). At this point the medial extension of the alveus includes all the WM until the teardrop shape of the lateral most hippocampal undulation (iii). This corresponds to the medial termination of the CA2/3 subregion in Winterburn et al. (2013). The lateral part of the WM ribbon excluded from the alveus is segmented as fimbria (iv). In more posterior areas the WM superior to the HF uncus region begins to lift (v). At this point the medial boarder of the alveus extends ¾ over the lateral most hippocampal undulation (vi). More posterior to this, the uncus disappears and the hippocampal body is reached (C). Here the WM ribbon superior to the hippocampal body is bisected at its halfway point (vii). This serves as the medial boundary of the alveus throughout the rest of the hippocampal body. It is also important to ensure that choroid plexus is excluded from the alveus demarcation (viii).

In more posterior regions, the HF tail becomes visible. At this point the c-shaped HF body moves superiomedially and elongates. The lateral definition of the alveus includes all the WM on the ventricular surface of the HF extending until the inferior most part of the HF (See Figure 19, blue line). The superior and inferior borders remain the CSF of the trigone of the lateral ventricle and ventricular surface of the HF respectfully. The alveus is traced superiomedially along the WM ribbon until it reaches a point where it begins to widen. This is the point at which the alveus will transition into the fornix (Figure 19, ii). This typically occurs approximately 1/3 of the way up the lateral bend of the HF (Figure 19, red lines). Tracing of the alveus ceases once the HF is no longer visible.

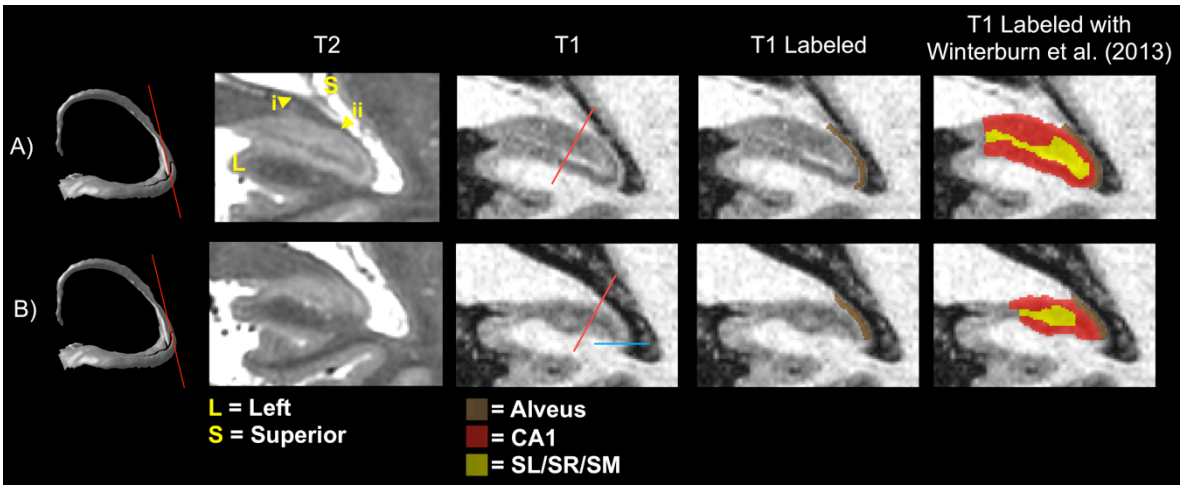

Figure 19. Description of alveus segmentation along the tail of hippocampus. Image depicts coronal sections through the right hippocampus of one subject. Rows A) and B) represent slices from anterior to posterior. Once the hippocampal tail is reached, the lateral border of the alveus is no longer the area where the alveus meets the border of the lateral ventricle. Instead, it extends until the inferior most portion of the hippocampus is reached (blue line). Superiomedially, the alveus curves up to meet the fornix (i). At this point the alveus widens and transitions into the fornix (ii). This serves as the medial extent of the alveus and corresponds to a line perpendicular to the hippocampus 1/3 of the way up its lateral bend (red lines on coronal slices).

Fimbria: The fimbria is a collection of WM which extends along the superomedial portion of the HF. It is the continuation of the alveus and therefore contains WM projections from within the HF. The fimbria travels posteriorly along the superomedial side of the HF and gives rise to the fornix. The Fimbria is best viewed on T1-weighted images, with T2 used to ensure segmentation accuracy in ambiguous areas.

Tracing of the fimbria occurs in the coronal plane once the uncal sulcus appears (Figure 20, i). All other planes are used to ensure correct and accurate segmentation. Similar to the alveus, the inferior extent includes all high-intensity WM above the grey matter of the uncus section. The superior border is the CSF of the temporal horn of the lateral ventricle. Early in the bifurcation of the HF head, the fimbria is traced laterally until the teardrop shape of the lateral HF undulation is reached (Figure 20, ii). Medially, the fimbria extends to include all the high-intensity WM over the uncal region until it is no longer visible. The fimbria continues only for a few slices superior to the uncus until it separates from the uncus completely. The CSF from the uncal sulcus is therefore used as an inferior border (Figure 20, iv). Laterally, the fimbria meets the alveus as it extends 1/3 of the way up the lateral HF undulation. Once the uncus disappears fully in the coronal plane, the fimbria extends laterally half-way up the WM ribbon superior to the HF body (Figure 20, vi). The fimbria is extended medially to include all the WM surrounded by the CSF. In this area, the choroid plexus is visible and should not be included. In addition, the tenia of the fimbria (i.e. tenia fimbriae) is visible (Figure 20, vii). This structure connects the choroid plexus in the lateral ventricles to the fimbria and should be excluded from fimbria segmentations. Axial and sagittal sections were also used to ensure the exclusion of choroid plexus and the tenia fimbriae.

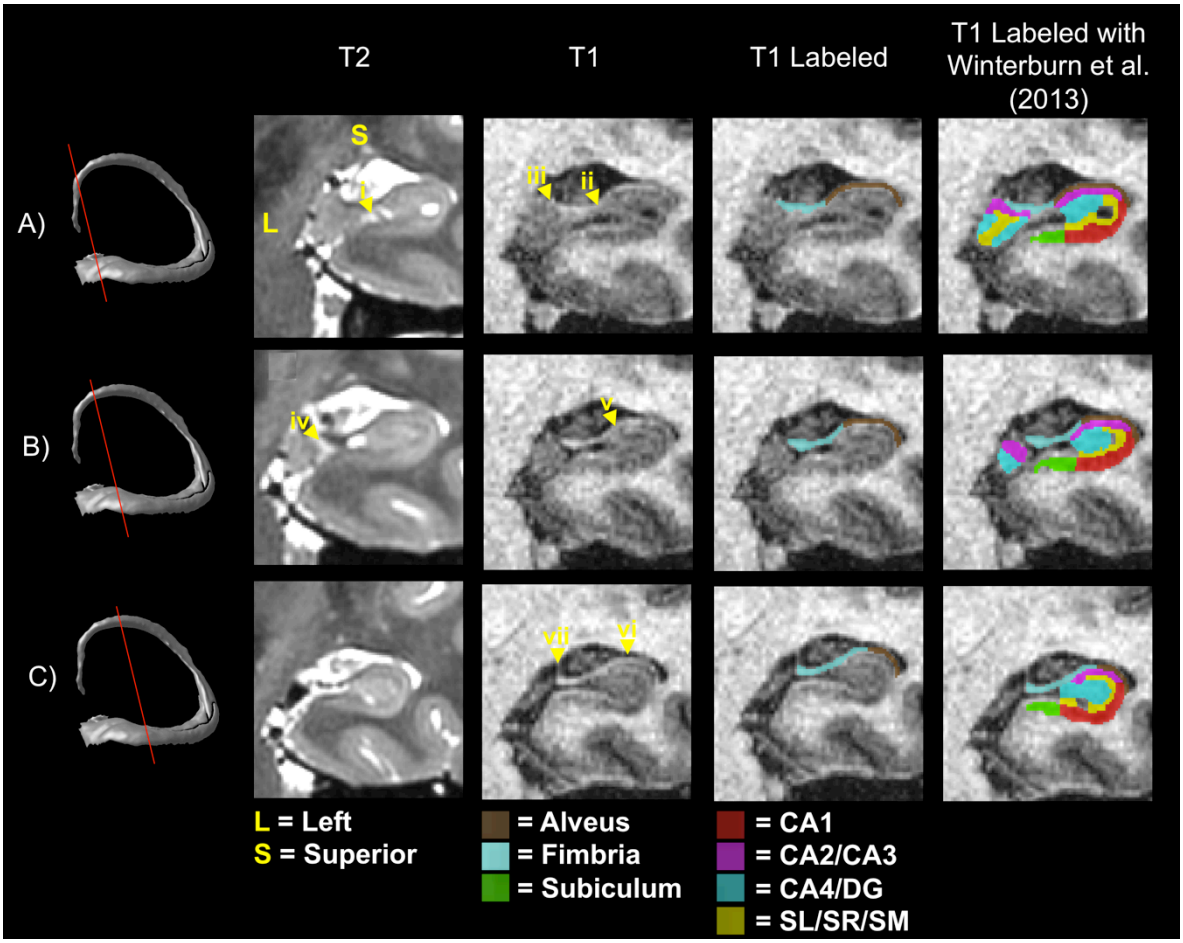

Figure 20. Description of segmentation protocol for the anterior fimbria. Image depicts coronal sections through the right hippocampus of one subject. Rows A) to C) represent slices from anterior to posterior. The fimbria is first traced once the uncal suclus is visible (i) and extends laterally until the teardrop shape of the lateral hippocampal undulation is reached (ii). Medially, the fimbria includes all WM superior to the hippocampal uncal region (iii). After separation of the fimbria from the uncus, the CSF from the uncal sulcus is used as an inferior border (iv). Laterally, the fimbria meets the alveus and extends 1/3 of the way up the lateral hippocampal undulation (v). Once the uncus disappears, the fimbria extends laterally half-way up the WM ribbon to meet the alveus (vi). The tenia of the fimbria is not included as part of the fimbria (vii).

Throughout the body of the HF, the fimbria condenses superomedially directly above the HF body. This shape remains relatively constant. The inferior, medial, and lateral borders remain the same as in previous slices. The superior border becomes the small area of CSF that connects the lateral ventricle to the lateral part of the transverse fissure (Figure 21, ii). In more posterior sections, the fimbria begins to rise as it approaches the crux of the fornix. This corresponds to the emergence of the pulvinar nucleus of the thalamus medial to the fimbria (Figure 21, iv). Care must be taken so as not to include the pulvinar nucleus as part of the fimbria segmentation. Here the fimbria's superior extent is drawn until the low-intensity area between the fornix and the

fimbria is reached (Figure 21, v). This area typically has both vasculature and choroid plexus that impede signal. It may be useful to use the T2 to guide tracing if contrast differences are unclear in the T1 image. At this point, the inferomedial portion of the fimbria is bordered by the CSF from the wing of ambient cistern (Figure 21, vi). Once the crux of the fornix is in full coronal view (i.e. the area where the WM of the fimbria and the fornix meet) segmentation of the fimbria ceases (Figure 21, vii).

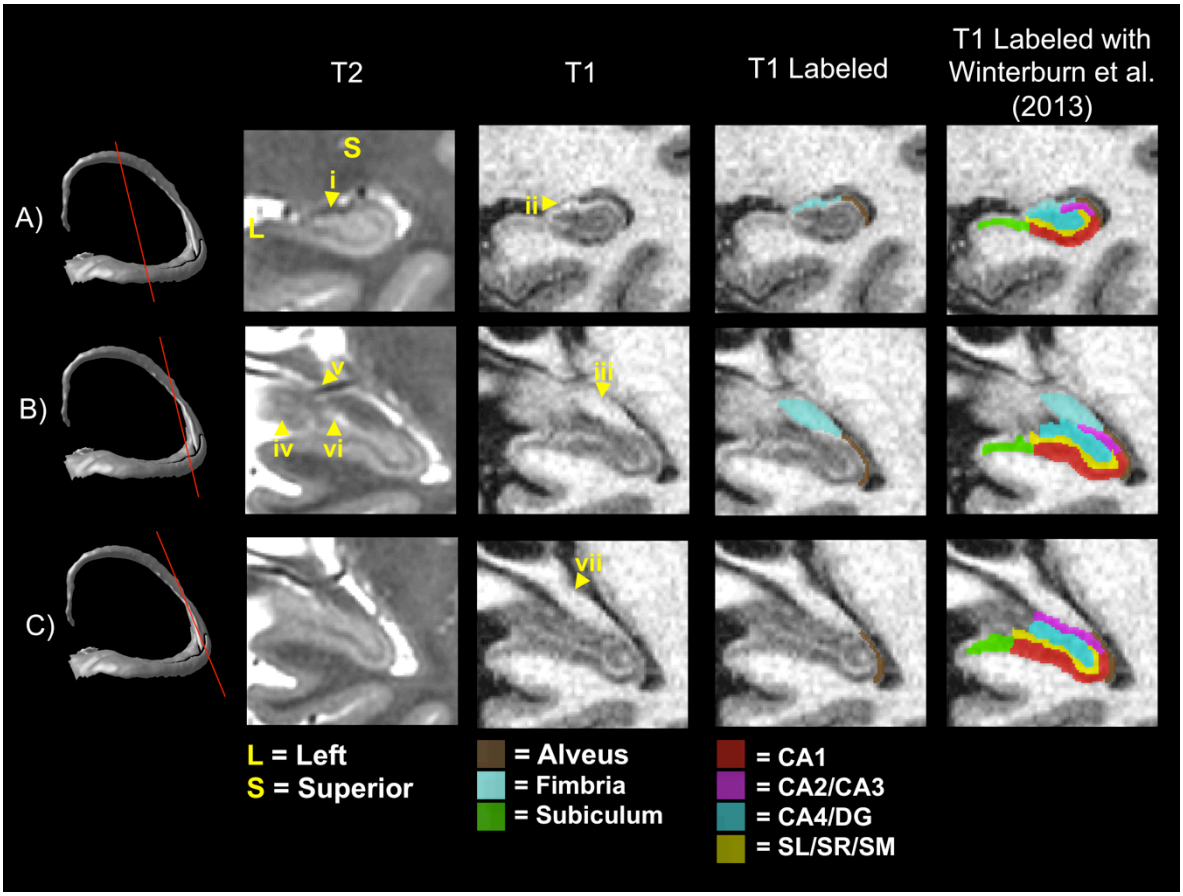

Figure 21. Description of tracing protocol for segmentation of the posterior fimbria. Image depicts coronal sections through the right hippocampus of one subject. Rows A) to C) represent slices from anterior to posterior. The fimbira can be seen superomedially atop the hippocampal body (i). The superior border is the small area of CSF that connects the lateral ventricle to the lateral part of the transverse fissure (ii). The posterior fimbria (B) begins to rise as it approaches the crux of the fornix (iii). At this point the pulvinar nucleus of the thalamus can be seen medial to the fimbria (iv). The pulvinar should not be included in segmentation of the fimbria. Here the superior extent of the fimbria is segmented until the low-intensity area between the fornix and the fimbria is reached (v). This area includes both blood vessels (v) and choroid plexus that impede signal. The inferomedial extent is bordered by the CSF from the wing of ambient cistern (vi). Once the crux of the fornix is in plain view (vii) the fimbria is no longer segmented.

Fornix: All WM fibers from the fimbria and alveus condense near the hippocampal tail to form the fornix. This large WM bundle then curves superiorly and travels anteriorly along the midline

of the brain. At the body of the fornix, each unilateral fornix joins tightly to the contralateral fornix near the midline. In more anterior sections, the fornices then descend vertically and ventrally (forming the region known as the anterior pillars of the fornix) to reach the mammillary bodies.

Tracing of the fornix begins following segmentation of the fimbria. Namely, once the crux of the fornix is visible (Figure 22, i), tracing begins in the coronal plane. Here, all the high-intensity WM of the crux of the fornix is included in the segmentation. The fornix is bound inferomedially at this point by the pulvinar nucleus of the thalamus (Figure 22, ii) and by the CSF of the quadrigeminal cistern (Figure 22, iii). Superiorly the WM of the fornix blends with the WM of the corpus callosum (Figure 22, iv) and the commissure of the fornix (which contains fibers connecting both hippocampi across the midline; See Figure 22, v) cannot be dissociated. Thus, a reliable and consistent definition is introduced that involves tracing the WM along the angle where the fornix meets the superior WM from its lateral to medial edge (Figure 22, red line on coronal slice). The lateral extent is bordered by the alveus and inferomedially by the grey matter of the HF, namely the CA1 subfield. In more posterior coronal slices, the fornix no longer connects supeiromedially near the WM of the corpus callosum. This is consistent with the disappearance of the subiculum and the isolation of the HF tail. The superiomedial boundary of the fornix is extended until the medial part of the HF ends (Figure 22, yellow lines) with the lateral border the same as listed above. Typically, all WM present between the CSF of the posterior horn of the lateral ventricle and the HF is included as fornix. It is important to note that this region is highly anatomically heterogeneous among individuals. Namely, some individuals maintain a large gap between the HF and alveus/fornix while others do not (Figure 23). This typically occurs when the WM of the splenium begins to extend underneath the WM of the fornix (Figure 23, ii). In such cases where the WM of the splenium contributes to the large WM separation between the HF and fornix, the T2-weighted images are used to dissociate the WM of the splenium and fornix. This involved the identification of a thin low-intensity band of CSF, which separated the two structures and served as the medial boundary. All WM lateral to this line was taken as WM of the fornix.

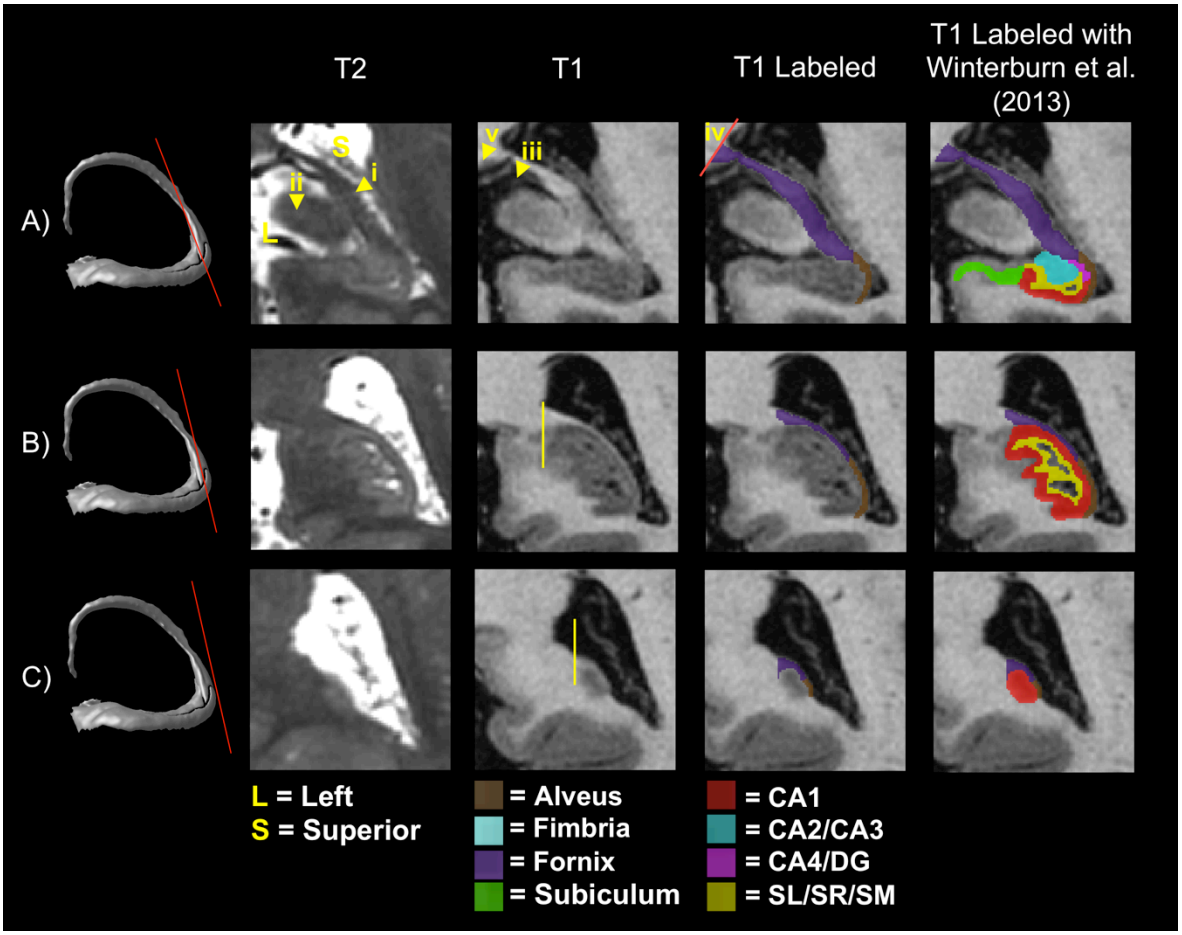

Figure 22. Depiction of protocol for tracing posterior areas of the fornix. Image depicts coronal sections through the right hippocampus of one subject. Rows A) to C) represent slices from anterior to posterior. Tracing of the fornix begins once the crux of the fornix is visible (i). The fornix is bound inferomedially by the pulvinar (ii) and by the CSF of the quadrigeminal cistern (iii). The WM of superior parts of the fornix blends with that of the inferior corpus callosum (iv). While the commissure of the fornix (v) may or may not be visible, demarcation of the fornix is unclear. At this point, segmentation of the fornix involves the inclusion of all WM present along the angle to which the fornix meets the superior WM (red line on coronal image). The lateral extent of the fornix is bordered by the alveus and inferomedially bordered by the grey matter of the hippocampus CA1 subfield. In more posterior slices (B & C), the fornix no longer connects supeiromedially near the WM of the corpus callosum. At this point the subiculum is no longer present and the hippocampal tail is isolated laterally. Here, the superiomedial boundary of the fornix is the point at which the medial part of the hippocampus terminates (yellow lines).

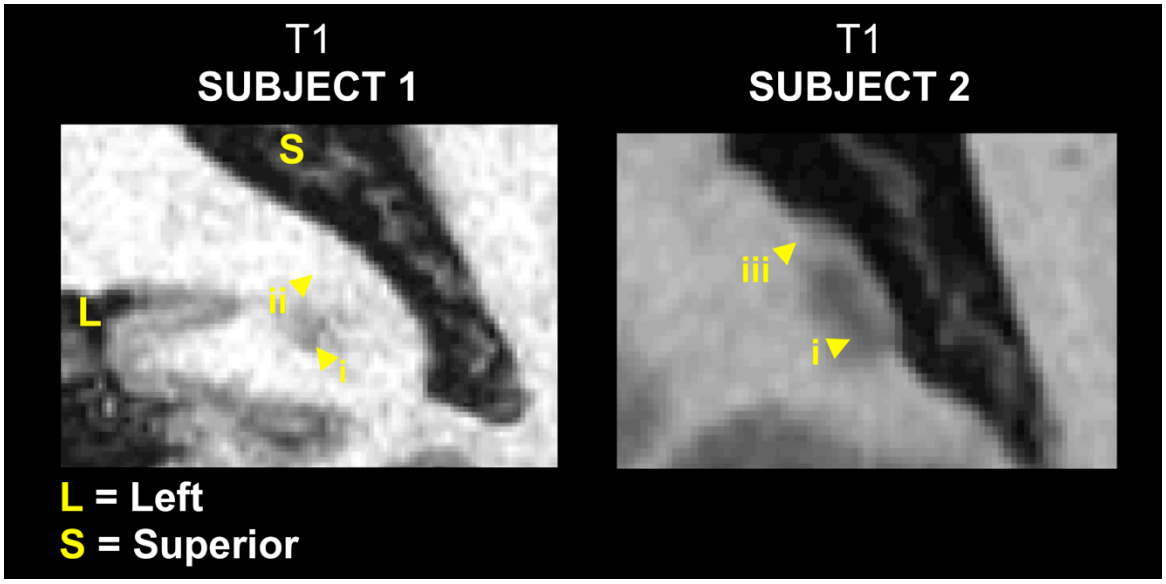

Figure 23. Coronal images depicting differences between posterior fornix anatomy for two different subjects. Namely, some individuals maintain a large gap between the hippocampus (i) and alveus/fornix. Here Subject 1 presents with a large gap (ii), while Subject 2 maintains a small area of white matter (iii). This typically occurs when the WM of the splenium extends underneath the fornix (as in ii).

Anterior to the crux of the fornix, the fornix rises superomedially. At this position, many different (albeit slight) anatomical variances between individuals exist (See Figure 24). The inferior, medial, and lateral borders are the CSF of the lateral ventricles. Superior borders remain as listed previously (Figure 25, red line on coronal image). Moving anterior along the coronal plane, the fornix begins to detach from the superior WM of the corpus callosum and a clear intensity difference can be seen superior to the fornix (Figure 25, v). It is important to note that along the medial side of the fornix, the tenia of the fornix is visible (Figure 25, vi). Functionally, the tenia of the fronix serves as a line of attachment anchoring the choroid plexus within the lateral ventricles. Its epithelial tissue therefore contains no axonal fibers and should not be included in fornix segmentation. Its visibility is denoted by a slight decrease in signal intensity.

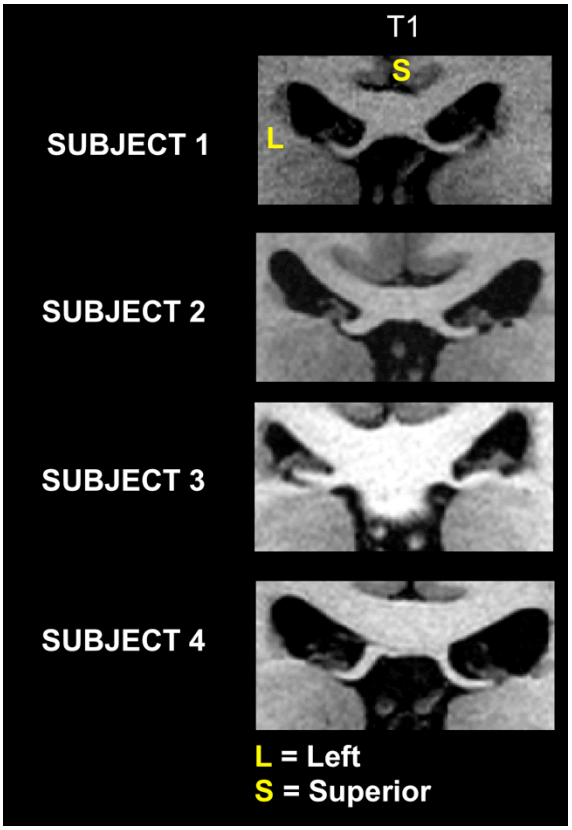

Figure 24. Coronal examples of fornix morphology variation from 4 different subjects. Images are of the area just anterior to crux of the fornix.

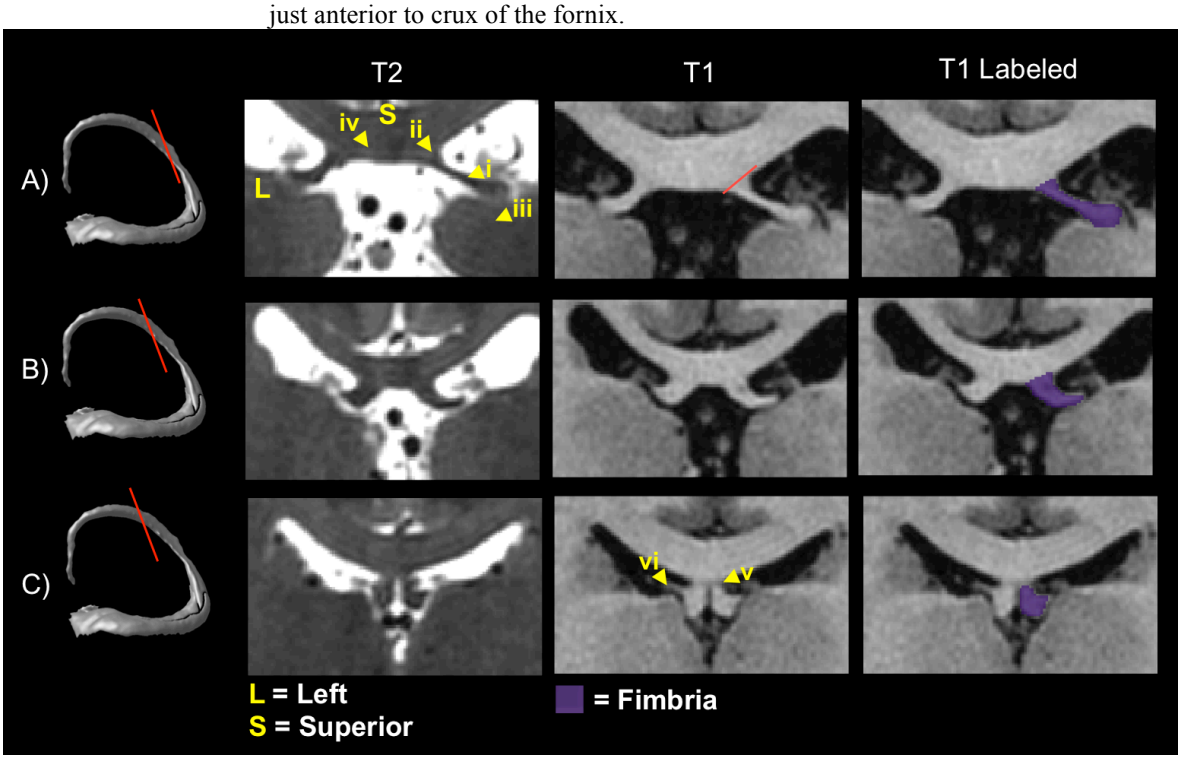

Figure 25. Image depicts segmentation protocol for anterior-middle area of the fornix. Rows A) to C) represent coronal slices from anterior to posterior from one subject. The fornix is visible (i) and elongates superomedially to

meet the WM of the corpus callosum (iii). The inferior, medial and lateral borders are the CSF of the lateral ventricles. The area connecting the fornix to the superior WM of the corpus callosum (ii) follows the same rule as listed previously (red line on coronal image). Anteriorly, the fornix detaches from the superior WM of the corpus callosum (iv) via a clear intensity difference (v) used as a superior border. Along the medial side of the fornix, the tenia of the fornix is visible (vi) and should not be included as fornix.

Moving further in the anterior direction coronally, both fornices appear to merge together tightly (Figure 26, i). This is the level of the body of the fornix. Care must be taken to delineate the left fornix from the right. This is best accomplished via the use of intensity differences present between the two fornices in the T2-weighted images. The superior border of the fornix is drawn to include all the WM below the septum pellucidum (Figure 26, iv). At this position, the area of fornix that moves inferiorly and slightly posteriorly to meet the mammillary bodies is visible and should therefore be segmented (Figure 26, ii). The high intensity WM of this inferior portion of the fornix should be included in the tracing, and care must be taken so as to avoid inclusion of the surrounding hypothalamic nuclei (Figure 26, iii). At this point, the anterior commissure is also visible (Figure 26, v) and serves as an inferior boundary. However, it should not be included within the segmentation. In extreme anterior coronal slices, the columns of the fornix are visible. At this point the medial borders are the CSF that is present between both pillars of the fornices (best seen in T2 image; See Figure 26, vi).

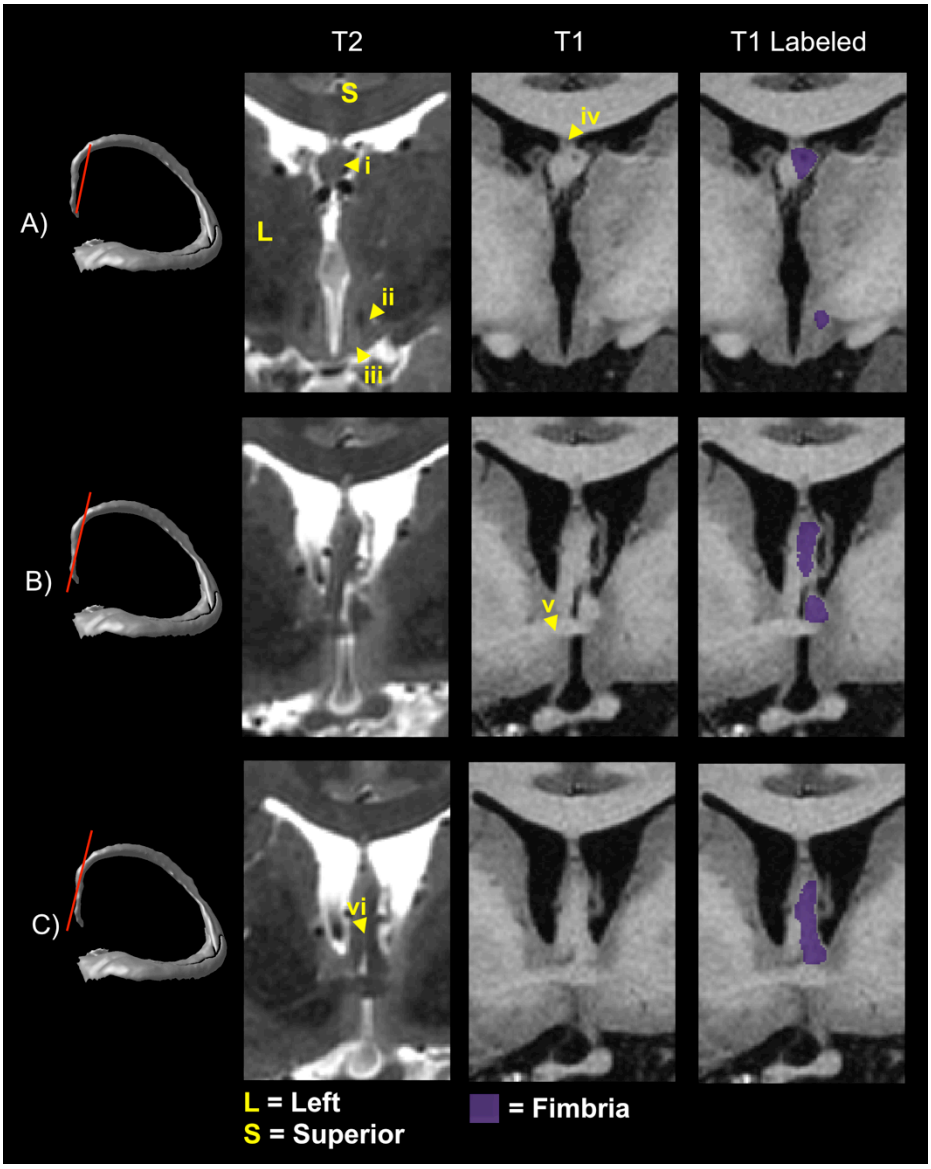

Figure 26. Fornix segmentation protocol for anterior-most area. Rows A) to C) represent slices from anterior to posterior. Fornices appear to merge tightly along the body of the fornix (i). The superior border of the fornix is the septum pellucidum (iv). At this position, the inferior part of the fornix that curves back posteriorly to meet the mammillary bodies is visible (ii) adjacent to the surrounding hypothalamic nuclei (iii). In more anterior slices the anterior commissure is visible (v) and serves as an inferior boundary. In these slices, medial borders are the contrast differences caused by the CSF between the two pillars (best seen in T2 image; vi).

Segmentation of the anterior columns of the fornix should be completed using the axial plane in T2-weighted images, which provide better contrast. In addition, axial slices perpendicular to the anterior columns of the fornix allow for increased discernibility. Superior-most axial slices depict both fornices elongating in the anterior-posterior direction (Figure 27, A). The medial and lateral borders are the CSF of the third and lateral ventricles respectively. These slices also

allow for the inspection of the superiomedial delineation of the fornix from the corpus made coronally (See Figure 25, red line on coronal image). If followed correctly, a smooth line contouring the corpus should be visible (Figure 27, ii). Moving inferior along the axial plane, both fornices merge but can still be dissociated based on intensity differences. Care must be taken to only include the high intensity WM of the fornix and not that of the septum pellucidum (Figure 27, v) or septal nuclei (Figure 27, vi). These structures appear anterior to the fornices and are of lower intensity in T1-weighted images. Moving inferiorly, the anterior commissure is reached (Figure 27, vii) at which point the fornix becomes considerably smaller and condensed. This serves as an anterior boundary for the fornix as it passes posteriorly behind the commissure. In the inferior-most axial sections, the fornix begins to thin and elongate toward the mammillary bodies. Here, all high intensity areas (low intensity in T2) are traced until the mammillary bodies.

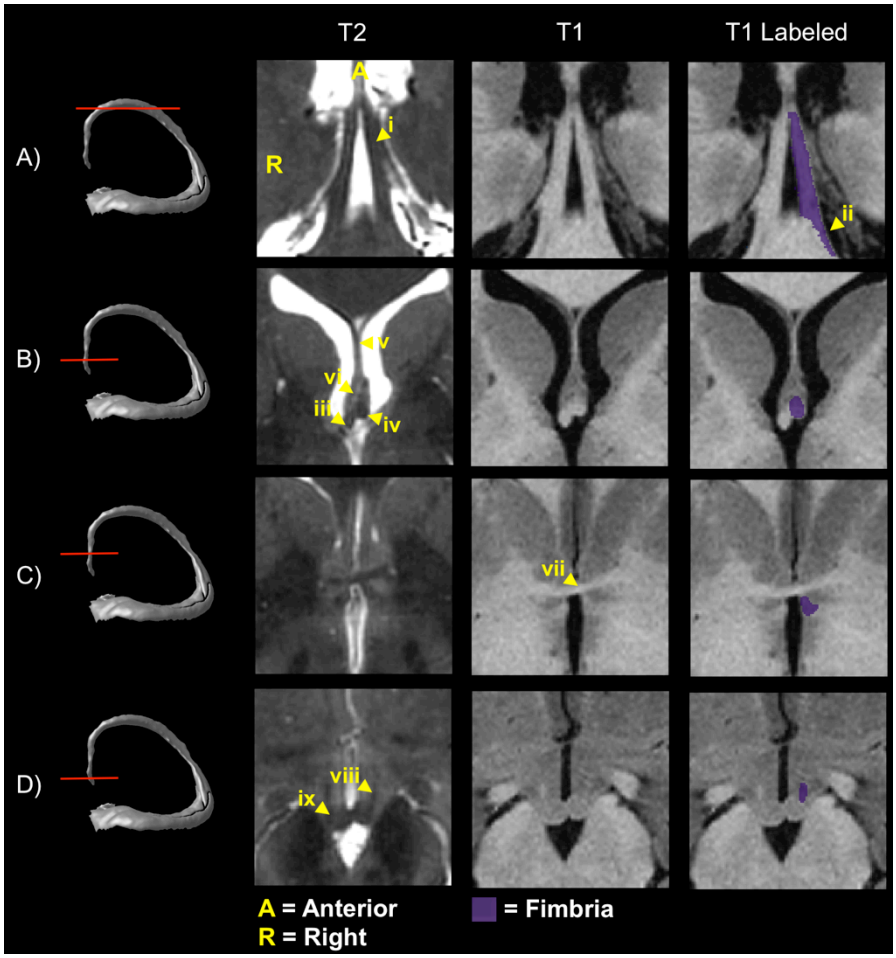

Figure 27. Anterior axial fornix segmentation. Rows A) to D) represent slices from superior to inferior for one subject. In superior-most axial slices, the fornix elongates in the anterior-posterior direction (i). These superior axial slices also allow for the inspection of the superiomedial delineation of the fornix made earlier. If followed correctly, a smooth line contouring the corpus callosum should be visible (ii). Moving inferior along the axial plane, both fornices merge together. Right (iii) and left (iv) fornices can still be dissociated based on intensity differences. The septum pellucidum (v) and septal nuclei (vi) appear anterior to the fornices and should not be segmented. Moving more inferior in the axial plane, the anterior commissure is reached (vii) and serves as an anterior boundary. At this point, the fornix becomes smaller and passes posterior to the anterior commissure. Inferior-most axial sections depict the fornix as thin and elongated (viii) reaching the mammillary bodies (ix).

The use of 3D reconstruction was employed throughout all tracings (Figure 28) and was found to be valuable in checking for anatomical accuracy. Its use also aided tracing in areas of ambiguity, or to identify areas that did not conform to the protocol. Moreover, additional planes were used to confirm anatomical accuracy of all regions following segmentation on the primary (or preferred) plane.

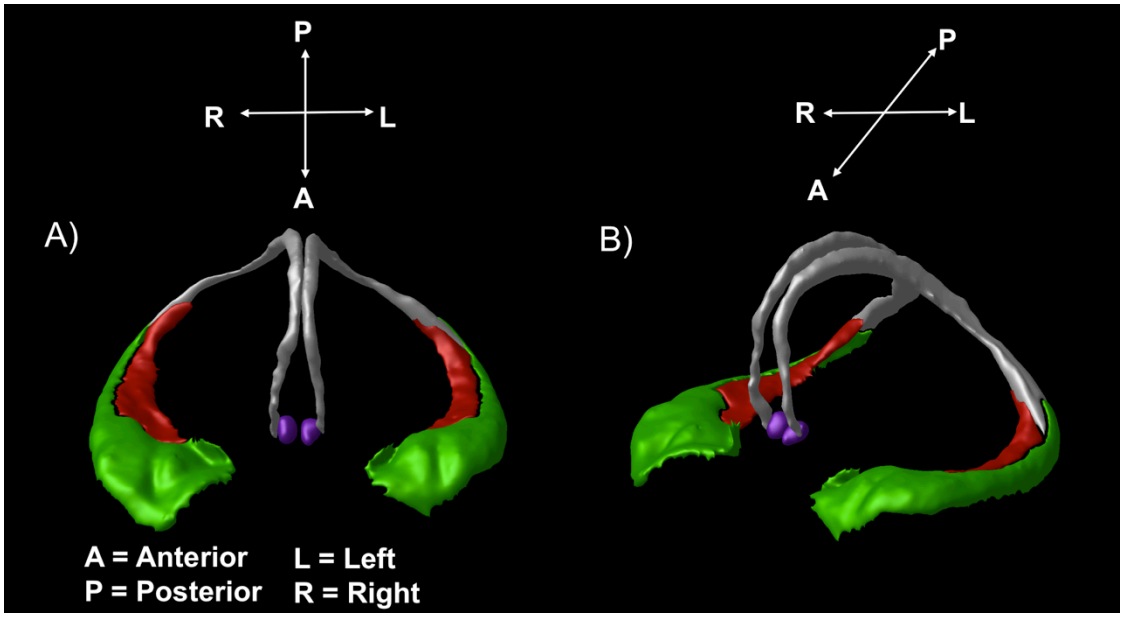

Figure 28. 3D rendering of completed segmentation for one subject. 3D reconstruction for all structures may serve as a valuable tool to check for anatomical accuracy or aid in tracing.

Appendix B: Population Demographics

Both the OASIS and ADNI subject cohorts were assessed for age/sex distribution characteristics. Age and sex ratios for the OASIS dataset were found to be relatively consistent across decades (Figure 29) with consistently more males. A negatively skewed histogram indicated a bias towards the inclusion of younger participants. A histogram of all ADNI subjects combined (i.e. controls, MCI and AD cohorts) revealed a relative balance of age and sex (Figure 30, A). While the histogram for controls revealed more female participants and was negatively skewed (Figure 30, B), the MCI histogram was positively skewed with a more male-based cohort (Figure 30, C). The AD cohort itself maintained a high female to male ratio (Figure 30, D).

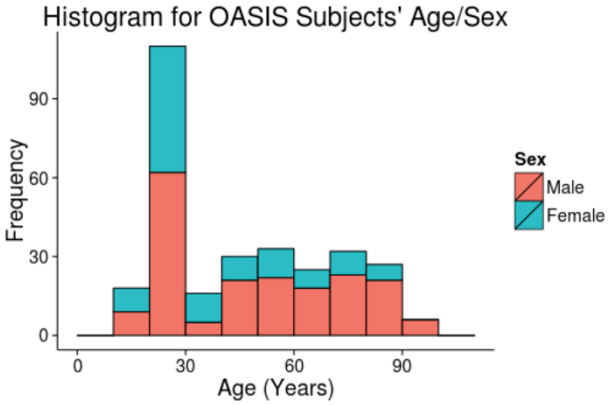

Figure 29. Histogram characterizing sex and age distributions in OASIS healthy aging dataset. Although positively skewed, male to female ratios are relatively consistent across each decade, with slightly more males.

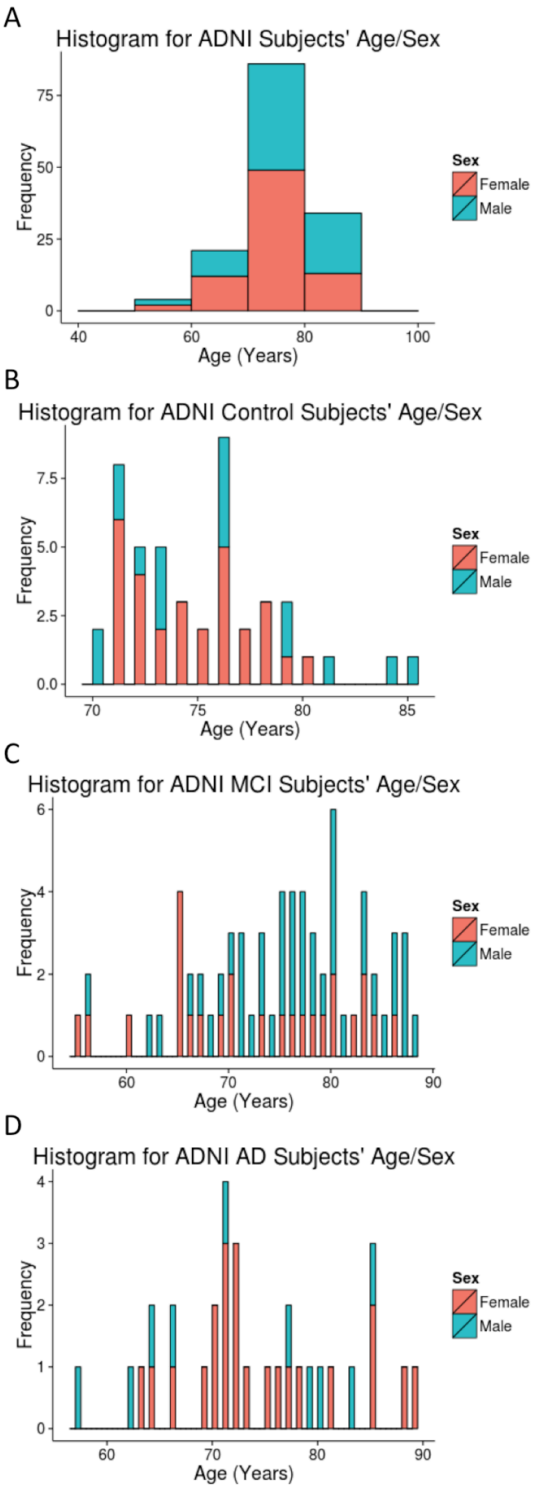

Figure 30. Histograms characterizing sex and age distributions in ADNI data. A: Histogram of age and sex distribution across all data groups included in analysis. Male to female ratios are well matched across each decade. B: Histogram of sex and age data for control group. C: Histogram of sex and age data for MCI group. D: Histogram of sex and age for AD group.

Appendix C: Quality Control of MAGeT Output

All MAGeT brain outputs were assessed for quality via manual inspection on a slice-per-slice basis (results are summarized in SM Table 1). Quality control (QC) was rigorously assessed using a three point system. All participants received a score of 1 (perfect), 0.5 (good) or 0 (fail). Any segmentation receiving a QC score of 0 was not included in the final analyses. Specific criteria existed for each QC value assigned. Given that the typical HF and its associated WM extends across approximately 30-45 coronal slices, some errors may exist. If segmentations maintained less then 5 slices per hemisphere where visible segmentation errors occurred, a QC score of 1 was assigned. Any segmentation with 5 to 10 slices containing errors was assigned a score of 0.5. If more than 10 errors were present unilaterally on separate slices, labels would be rejected and receive a failing score of 0 (See Figure 31 for examples). Images were also 3D-Rendered to ensure anatomical accuracy (Figure 32).

The above-mentioned errors typically involved small deviations from the correct and true segmentation (See Figure 31, arrowheads). Segmentations occasionally revealed large, gaping holes encompassing significant portions of the HF. At times, such inaccuracies would extend along the entire length of the HF, while others would only continue for a few dozen slices. Albeit rare, such segmentation faults were considered to be too unremitting and were consequently rejected outright, (regardless if most HF subfields or WM regions remained intact). Rather, errors typically involved small shifts in label placements (e.g. CA1 label bleeding into subiculum) or, more frequently, over/underestimation of specific labels (e.g. over estimation of the alveus leading to inclusion of CSF as WM). Special attention was also paid to proper SL/SR/SM segmentation, which is most visible in 1mm scans given its high intensity signal. It is also important to note that accuracy during quality control was taken into consideration by looking at segmentations as a whole (e.g. all HF subfields) not on a one-per-one basis (CA1, CA2/3, CA4/DG, etc.).

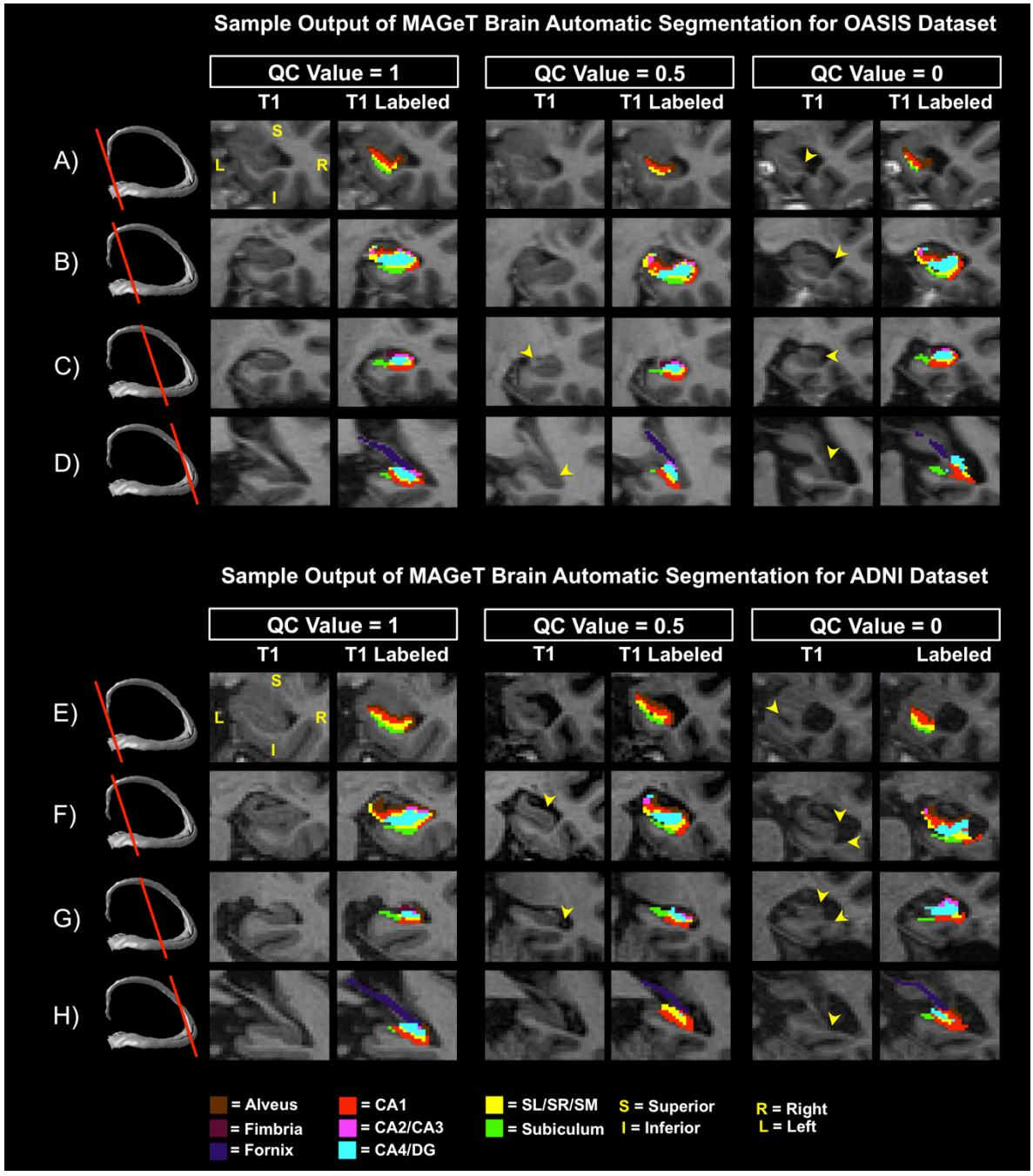

Figure 31. Sample outputs from OASIS and ADNI cohort segmentation via Multiple Automatically Generated Templates (MAGeT Brain) and quality contol methods. Rows A-D indicate sample outputs from OASIS segmentation and determination of quality control designation. Rows depict T1 weighted coronal sections through the right hippocampal: A) anterior head, B) posterior head C) body and D) tail. Areas of label error are indicated by yellow arrowheads. Rows E-H depict sample output segmentations from the ADNI dataset. T1 weighted coronal sections through the right hippocampal: E) anterior head, F) posterior head G) body and H) tail are shown. Areas of label errors are indicated by yellow arrowheads.

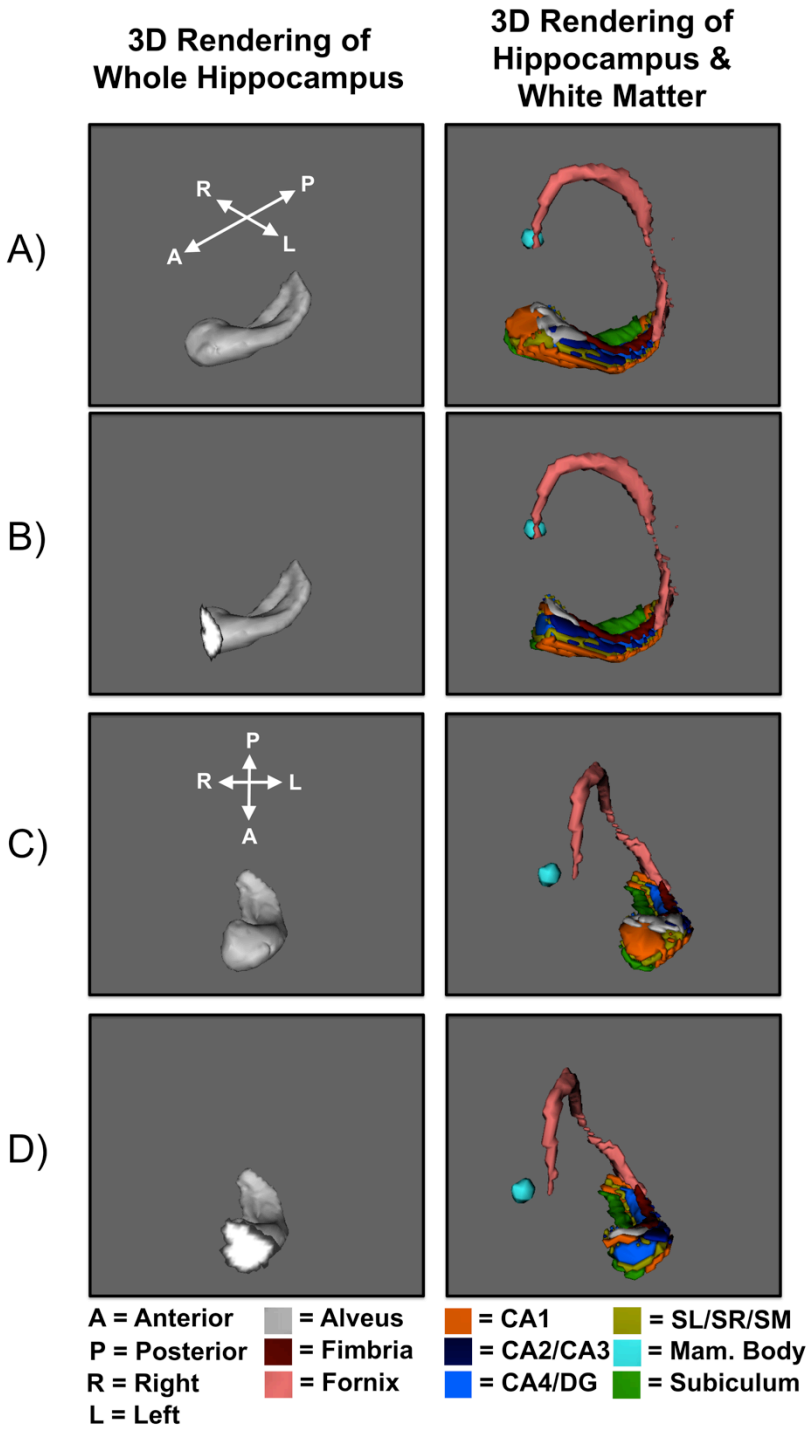

Figure 32. 3D rendering of MAGeT-Brain segmentation output for one randomly chosen OASIS subject. Rows A) and B) show the medial aspect of the left hippocampus subfields and white matter regions. Rows C) and D) depict the anterior aspect of the left hippocampal subfields and white matter regions. Given that white matter regions curve in and out of plane with anatomical complexity, 3D reconstruction allowed for confirmation of proper anatomical placement of MAGeT-Brain generated labels.

Appendix D: Brain Extraction Based on Nonlocal Segmentation Technique (BEaST)

Recently, a robust and reliable method of brain extraction described as brain extraction based on nonlocal segmentation technique (BEaST) has been made available. BEaST employs a library of 80 priors to complete nonlocal segmentations of brain masks in a multi-resolution framework (Eskildsen et al., 2012). This method of brain extraction is thought to be more reliable and true to the underlying anatomy. Therefore, BEaST was also used as a complementary to the estimated total intracranial volumes provided in the OASIS and ADNI datasets. Prior to statistical analysis, BEaST outputs were also controlled for quality.

BEaST Quality Control:

Similar to MAGeT-Brain segmentations, BEaST outputs also underwent quality control in order to ensure accurate segmentation (Figure 33). Each brain mask was inspected on a slice-per-slice basis using MINC Display. Unlike the three-point system used for the quality control of MAGeT brain segmentations, BEaST output was measured using a two-point pass/fail system. Brain masks receiving a score of 0 did not pass quality assessment, while those receiving a score of 1 passed. Given the size of a typical whole-brain mask, errors focused on those that omitted large parts of the cortex or other brain regions (See Figure 33). While such errors were rare, minute errors were occasionally visible but did not warrant a score of 0. Such errors involved the mistaken inclusion/exclusion of areas into the label, most frequently occurring along the cortical surface. An example of this would involve the whole-brain mask including CSF of the subarachnoid space into the whole brain label. Despite only continuing for a few slices, such minute errors were nonetheless surprisingly infrequent.

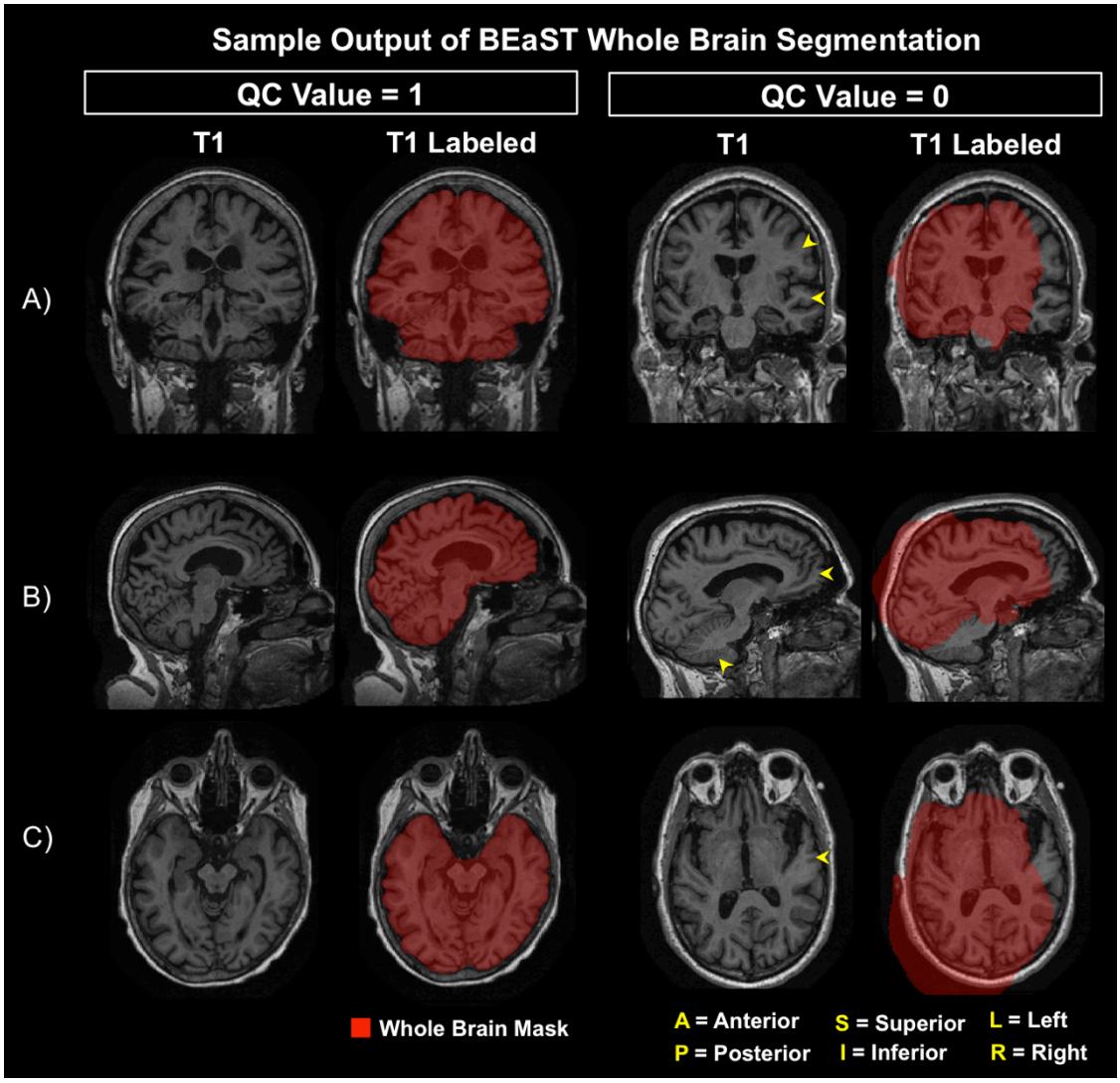

Figure 33. Sample outputs from BEaST whole brain segmentation and determination of quality control (QC) designation. Each image was rated with a QC value of either 1 (Pass) or 0 (Fail). Any disturbances in the whole brain mask constituted a QC value of 0. **A)** Coronal section through a sample T1-weighted image and corresponding whole brain mask for both a successful and unsuccessful subject. **B)** Corresponding sagittal section through a sample T1-weighted image and corresponding whole brain mask for both a successful and unsuccessful subject. **C)** Corresponding axial section through a sample T1-weighted image and corresponding whole brain mask for both a successful and unsuccessful subject. Out of 315 OASIS cases 3 did not pass QC. 5 out of 151 ADNI cases did not pass QC.

BEaST Quality Control Results:

BEaST quality control for the OASIS dataset resulted in 396 successful whole brain segmentations. A total of 3 segmentations did not pass QC. For ADNI cohorts 8 subjects failed in total leaving a total of 143 individuals with successful whole brain segmentations.

OASIS Dataset Analyzed Using BEaST Measure:

All linear model statistics were re-computed using BEaST eTIV. A general linear model covarying for sex and TIV (obtained through BEaST) was used to assess volumetric changes across age. No significant changes were observed with respect to combined WM volumes (i.e. alveus fimbria and fornix; Left: p=0.12; Right: p=0.24). Out of all the WM subregions, the bilateral alveus showed the most increase across age (Left: R^2=0.15, p<0.001; Right: R^2=0.12, p<0.001). The left fimbria was found to decrease over time (R^2=0.022, p<0.002) while the right fimbria failed to reach significance (p=0.79). Decreases in fornix volume were observed for both the left (R^2=0.015, p<0.006) and right (R^2=0.026, p<0.001) fornix.

A significant change in the combined HF total volumes was found for the right HF (R^2=0.013, p<0.007) but not the left (p=0.29). Significance was observed in some of the subfield structures as defined by Winterburn et al. (2013). With respect to the HF subfields, significance was observed in the left and right CA1 region (respectively, Left: R^2=0.058, p<0.001; Right: R^2=0.061, p<0.001) demonstrating increases in volume over time. The left and right CA4/DG showed no significance (Left: p=0.18: Right: p=0.35). The left SL/SR/SM was found to significantly decrease over time (R^2=0.0043, p=0.01). No significant differences were observed for the right SL/SR/SM (p=0.88).

ADNI Dataset Analyzed Using BEaST Measure:

As in stated in 'BEaST Quality Control Results', the ADNI dataset also included measures of intracranial volume (ICV). BEaST was used to provide another measure of total brain volume. All linear models were re-computed using BEaST measures.

A general linear model accounting for age, sex, and TIV (as obtained by BEaST), was used to assess changes in volume across disease states. Comparing controls to the MCI cohort, a trending but non-significant decrease was observed for the combined WM volumes (i.e. alveus fimbria and fornix; Left: R^2=0.02, p=0.056; Right: R^2=0.0015, p=0.093). A significant decrease in HF

volume also occurred comparing controls to MCI (Left: R^2=0.085, p<0.001; Right: R^2=0.043, p<0.001). Out of all WM subfields, the bilateral alveus was the only region that did not exhibit a significant difference between control and MCI cohorts (Left: R^2=-0.004, p=0.5353; Right: R^2=0.006, p=0.1870). On the other hand, the bilateral fimbriae were found to decrease bilaterally (Left: R^2=0.15, p<0.001; Right: R^2=0.066, p=0.004) as did the fornices (Left: R^2=0.033, p=0.025; Right: R^2=0.071, p=0.002).

Between the MCI and AD cohorts no significant effect was found for all WM regions combined (Left: p=0.45; Right: p=0.99). Although trending, no significance was observed with respect to the whole HF (Left: R^2=0.05, p=0.21; Right: R^2=0.001, p=0.29). All WM subfields, including the bilateral alveus (Left: p=0.79; Right: p=0.64), right fimbria (p=0.93), and bilateral fornix (Left: p=0.43; Right: p=0.72), were not significantly different. However, the left fimbria was found to have a significant decrease (R^2=0.031, p=0.045).

Comparing controls to AD patients reveled significant decreases in combined left WM volumes (R^2=0.056, p=0.008) and a similar trending result was observed for the right WM (R^2=0.018, p=0.10). The combined HF volumes were also significantly decreased in AD cohort compared to controls (Left: R^2=0.19, p<0.001; Right: R^2=0.12, p<0.001). The bilateral alveus showed no significant difference between cohorts (Left: p=0.46; Right: p=0.084. Both the bilateral fimbria (Left: R^2=0.29, p<0.001; Right: R^2=0.065, p=0.002) and fornix (Left: R^2=0.046, p=0.026; Right: R^2=0.074, p=0.007) were found to have significantly decreased volumes in the AD group compared to controls.